UNIVERSITY OF OSLO
Faculty of Mathematics and Natural Sciences;
Department of Geosciences; Meteorology and Oceanography Section

Investigating the shift in the North-Atlantic storm track

Thesis for the degree of Master of Science

Lise Seland

June 2, 2009

Abstract

This thesis presents results from an AGCM sensitivity study in which the response in the Northern Hemisphere storm tracks to an imposed SST anomaly is investigated. The study was motivated by observational studies cited in the IPCC Fourth Assessment Report indicating that the storm tracks have shifted northward during the second half of the 20th century, a shift which may be related to global warming.

To perform sensitivity studies, the NCAR CAM3 model was applied using the data ocean model with an imposed 2 K SST anomaly in all oceanic grid points north of 45°S. Additionally, the sensitivity to longitudinal and latitudinal variations in the SST anomaly domain was investigated by heating high-latitudes and low-latitudes, only high-latitudes and only low-latitudes in the Atlantic and Arctic Ocean in three different runs. To investigate the importance of a potential reduction in the ice cover, CAM3 was run without ice in the Northern Hemisphere. The storm tracks were represented in terms of bandpass variance using the bandpass filter method and cyclone count using the CCI method developed by Rasmus E. Benestad at the Norwegian Meteorological Institute.

Warming the ocean by 2 K in all oceanic grid points north of 45°S yields, in terms of bandpass variance, a northeastward shift in the North-Atlantic storm track and no latitudinal shift in the Pacific storm track, with corresponding changes in atmospheric baroclinicity and the mean circulation. The zonally averaged Eady parameter shifts upward and northward in response to an increased upper-level temperature gradient and a decreased lower-level temperature gradient, consistent with the findings of Yin (2005). As Yin (2005) performed a climate scenario study using a 15 member ensemble of coupled GCMs, while this study investigates the effects in a uncoupled AGCM where the only forcing is a positive SST anomaly, indications are that *oceanic heating is the main driver of the observed storm track changes*.

Variations in the SST anomaly domain reveals that *low-latitude heating is the primary driver of the observed storm track changes*. Removing the ice cover yields changes of comparable magnitudes to high-latitude heating, as is therefore not as important as low-latitude heating.

Acknowledgements

This thesis is submitted to the Department of Geosciences at University of Oslo in partial fulfilment of the requirements for the degree of Master of Science. The work was carried out at the Meteorology and Oceanography Section (MetOs) of the Department of Geosciences at the University of Oslo, during 2008 and 2009. My supervisor and co-supervisor in this project were professor Joseph H. LaCasce at MetOs and senior scientist Rasmus E. Benestad at the Norwegian Meteorological Institute.

I would particularly like to thank professor Joseph H. LaCasce for all the help and guidance, and for always taking the time to look at my figures and reading my thesis drafts.

Thanks also to Rasmus E. Benestad for helping me with the CCI method and the associated plotting. I would also like to thank my parents, Ninni Seland and Bjarne Seland, for raising me and always supporting me in my choices. And finally, thanks to Joachim Moe Graff for all the support, encouragement and proofreading, especially during the last months.

This thesis was written in the LaTeX document preparation system. Drawings were, unless stated otherwise, created with the LaTeX `picture` environment.

Atmospheric simulations were performed using the NCAR CAM3 model. Modifications to the CAM3 initial conditions data set were made using the R environment of statistical computing developed by R Development Core Team (2008) and the R-package `NCDF` (Pierce, 2006).

The reanalysis data used in this project was taken from the NCEP/NCAR reanalysis 1, provided by the National Ocean & Atmosphere Administration/Outstanding Accomplishments in Research/Earth System Research Laboratory/Physical Sciences Division, Boulder, Colorado, USA, from their web site at `http://www.cdc.noaa.gov/`.

Feature point statistics was created using the CCI method available from the R-package `cyclones` (Benestad, 2008) created by Rasmus E. Benestad. Both the R environment and the R-packages are freely available from `http://cran.r-project.org/`. Bandpass filtering was performed using the intrinsic Interactive Data Language (IDL) function `DIGITAL_FILTER`. All plotting was performed using R and IDL.

Lise Seland
Oslo, June 2, 2009

Contents

List of Figures

List of Tables

Chapter 1

Introduction

Extra-tropical cyclones (from now on referred to as cyclones) are features subject to much attention on both synoptical and climatological timescales. On synoptical timescales, cyclones are responsible for most of the severe mid-latitude weather events, and are commonly known for their strong winds and heavy precipitation (Holton, 2004). On climatological timescales, cyclones are important contributors to meridional transport of heat and momentum at mid-latitudes (Holton, 2004).

On climatological time-scales, certain regions in the North-Atlantic and Pacific are characterized by relatively high cyclone frequencies. These regions stretch from the east coasts of North-America and Asia into the respective oceans towards the Norwegian/Barents Sea and the west coast of North-America. The North-American and Asian east coasts are well suited for cyclone formation, particularly during the winter, as the land-ocean heat contrasts yield strong meridional temperature gradients and by thermal wind balance strong vertical wind shear, making these regions highly baroclinic and favorable for baroclinic growth.

These areas of high cyclone frequency are commonly referred to as *storm tracks* or storm bands. Storm tracks have been subject of much attention for more than a century. In the late 19th century, individual cyclone trajectories would be estimated by eye from e.g. ship observations, picking out the storm track regions where the cyclones preferably traveled (e.g. Hinman (1888)). With the computer came objective automatic methods for storm track identification and analysis. An early method was temporal filtering in which one would apply e.g. a bandpass filter to the 6 h Sea Level Pressure (SLP) field to retain fluctuations with frequencies corresponding to that of a growing baroclinic wave (e.g. Blackmon (1976), Blackmon et al. (1977)), yielding the storm tracks as large maxima in the bandpass variance field. With increasing computer power, more computationally demanding methods were developed and applied which would detect low-centers in the SLP field (so-called feature point identification) and subsequently find the most probable trajectory followed by each low-pressure center (so-called feature point tracking) (e.g. Hodges (1994), Hoskins and Hodges (2002)). Feature point identification methods are commonly applied without subsequent feature point tracking yielding cyclone count statistics (e.g. Benestad and Chen (2006)).

With the availability of reanalysis products

such as the National Center of Environmental Prediction/National Center of Atmospheric Research (NCAR/NCEP) reanalysis 1, and the European Center of Medium-range Weather Forecast (ECMWF) 40-year reanalysis (ERA40), long term studies of storm track trends were made feasible yielding a number of storm track trend analysis (e.g. McCabe et al. (2001), Gulev et al. (2001), Wang et al. (2006), Benestad and Chen (2006), Hoskins and Hodges (2002)) The Intergovernmental Panel of Climate Change (IPCC) Fourth Assessment Report (Trenberth et al., 2007) sites a number of studies (e.g. Gulev et al. (2001), McCabe et al. (2001), Wang et al. (2006)) indicating that there has been significant changes in the storm track structure and intensity during the second half of the 20th century. Among these changes is a northward shift in storm track position (Wang et al. (2006), McCabe et al. (2001)). Yin (2005) found a consistent northward shift in storm track position using 15 coupled IPCC climate models forced with increased greenhouse gas concentrations in accordance with the A1B scenario from the IPCC Special Report on Emission Scenarios (Nakicenovic et al., 2000).

Motivated by findings of reanalysis studies and climate scenario studies such as McCabe et al. (2001) and Yin (2005), indicating that the storm tracks shift north in response to global warming, *the aim of this study was to investigate the potential northward shift in the North-Atlantic storm track in response a 2 K oceanic warming, which is expected to occur in response to global warming, in an Atmospheric General Circulation Model (AGCM)*. Additionally, the response to longitudinal and latitudinal variations in the oceanic warming domain and to removing the ice cover from the entire Northern Hemisphere will be investigated.

To perform simulations, the NCAR Community Atmosphere Model version 3.0 (CAM3) was applied with a Eulerian dynamical core, T42 and T85 resolution in the horizontal, 26 vertical layers and the Data Ocean Model with 12 monthly prescribed Sea Surface Temperature (SST) and ice coverage samples. All modifications were made to the SST and ice coverage fields in the initial condition data set file. The NCEP/NCAR reanalysis was used for model validation. The storm tracks in this study are represented in terms of bandpass variance and cyclone count using the bandpass filter method described in section 4.1 and the Calculus-based Cyclone Identification (CCI) method from Benestad and Chen (2006) described in section 4.2. The time period investigated is 1. December 1980 – 28. February 1990 using the Northern Hemisphere winter months December, January and February (DJF) only.

In the following, an overview of important storm track theory is given in the second chapter, data and methods are presented in the third and forth chapter, respectively, the results are presented in the fifth chapter and summarized and discussed in the sixth chapter. Finally, suggestions for future work is given in the seventh chapter.

Chapter 2

Theory

2.1 What are storm tracks?

Extra-tropical cyclones (referred to as cyclones from now on) are the synoptic-scale features which constitute the storm track on climatological timescales. Cyclones exist due to the baroclinic nature of the mid-latitude atmosphere. Uneven solar heating combined with the prevailing thermal wind balance yields strong westerly wind shear in the vertical. Cyclones start off as small perturbations in the westerly mean flow and will, if they are of certain structures, be able to grow by feeding on the energy of the mean flow. Cyclones are able to extract energy from the mean flow by redistributing mass in such a way as to lower the atmospheric center of mass, thereby converting atmospheric potential energy into kinetic energy. The redistribution of mass yields meridional and vertical heat transport contributing simultaneously to reducing the meridional temperature gradient and the vertical wind shear.

Cyclogenesis, the initial growth and development of a cyclone, predominantly occurs in areas of enhanced baroclinicity. Such areas are found off the east coast of North-America and Asia where the contrast between the cold continents and the warm western boundary currents cause strong meridional temperature gradients. Due to the large heat capacity of the ocean and the low heat capacity of the continents, the baroclinicity is greatest during the winter months. Cyclones travel east along with the jet stream as they grow, reach their mature stage, and ultimately undergo cyclosis, the process of cyclone decay.

The storm tracks are climatological features. On climatological timescales, cyclone frequency in the Northern Hemisphere is particularly high in bands stretching from the traditional baroclinic regions off the east coasts of North-America and Pacific across the North-Atlantic and Pacific oceans towards the Barents Sea and northeastern Pacific. These bands are known as *storm tracks*. Traditionally it has been believed that cyclones would develop in the western end of the storm track, in what is known as the *storm track entrance region*, travel eastward within the storm track region following the jet stream and finally decay in the *storm track exit region* (Chang and Orlanski, 2002). Results several studies (e.g. Hoskins and Hodges (2002), Gulev et al. (2001), Chang and Orlanski (1993), Black and Dole (2000)) indicate that this might not be the case, rather cyclogenesis and

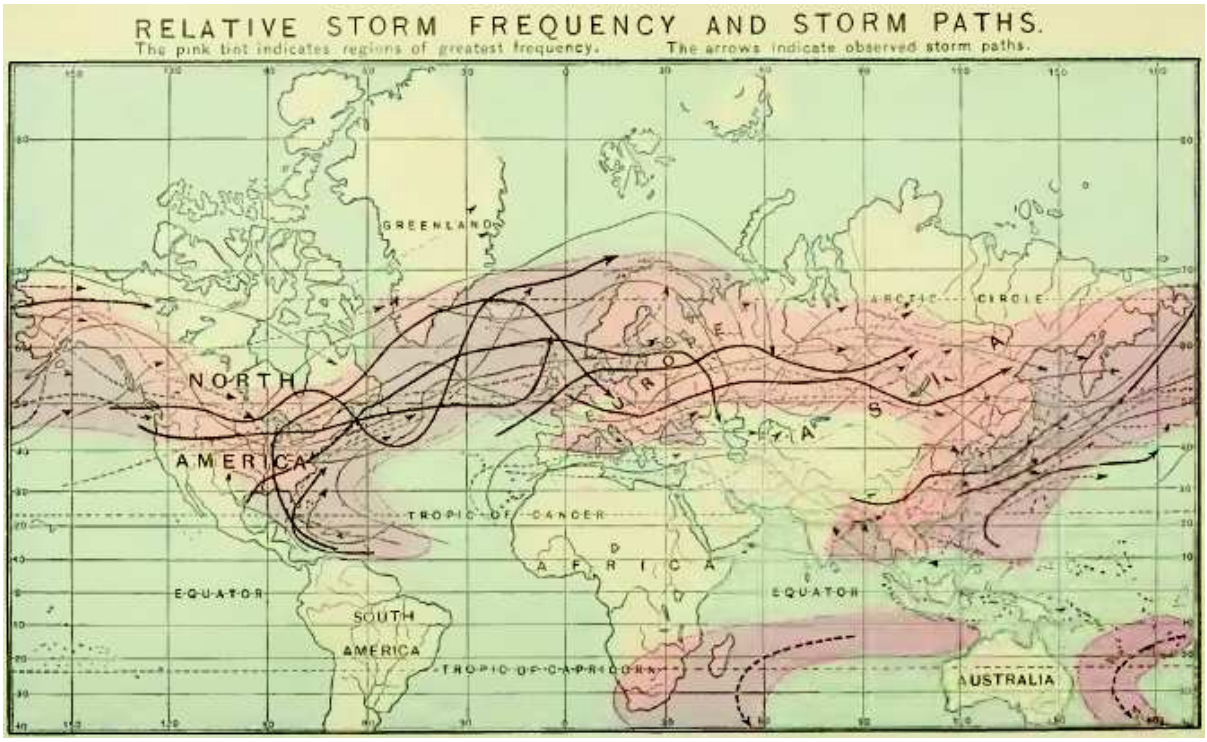

Figure 2.1: *Relative storm frequency and storm paths from Hinman (1888). As stated in the figure title with the small font size, pink areas indicates the regions of highest storm frequency and the arrows indicate observed storm trajectories.*

cyclosis occur to some degree all over the storm track regions.

In terms of the general circulation, the North-Atlatic and Pacific storm tracks start off near the stationary trough in the mean geopotential height field placed over the western parts of the Atlantic and Pacific oceans and terminate near the ridges in the mean geopotential height field found over western Europe and the west coast of North-America (Orlanski, 1998). Orlanski (1998) argues that compared to the jet stream maximas placed over Japan and the east coast of North-America, the storm tracks originate somewhat poleward and downstream of the vertical and horizontal shear zone.

Storm tracks have been a subject of much attention for more than a century. Figure 2.1 shows observed storm frequency and storm trajectories from Hinman (1888), a 19th century school book. Pink regions indicate the areas of greatest storm frequency and the arrows indicate the individual observed storm trajectories. From looking at this figure, it is clear that no distinction has been made between extra-tropical and tropical cyclones. Even so, the traditional North-Atlantic and Pacific storm tracks stand out as regions of both high storm frequency and several observed trajectories.

Storm track definitions differ from study to study depending on the approach (Eulerian, Lagrangian). Storm tracks are loosely defined as geographical areas of high extra-tropical cyclone activity. There is no single way of defining cyclone activity. Different studies utilize different methods, and it is commonly argued (by e.g. Paciorek et al. (2002)) that this is meaningful because cyclones are complex features and different approaches yield different information.

Measuring cyclone activity in terms of observed low-pressure systems is a common method applied in so-called "feature point identification studies" (e.g. Benestad and Chen (2006), McCabe et al. (2001)) activity being measured in terms of observed low-pressure centers, cyclone trajectories, or baroclinic wave activity. Feature point identification is a collective terms for methods that involves finding and counting low-pressure centers, most commonly utilized on the sea level pressure field. Ultimately this method leads to cyclone frequency statistics, yielding information about where, statistically, low-pressure centers are found in time and space. In this context storm tracks are areas experiencing relatively high frequency of low-pressure systems.

The second approach in which one measures cyclone activity in terms of cyclone trajectories in known as feature point tracking methods (e.g. Gulev et al. (2001), Hoskins and Hodges (2002)). Feature point tracking methods are more advanced and yield different information. They compute the trajectories of the low-pressure centers from cyclogenesis to cyclosis. Consequently, feature tracking methods yields information about where the cyclones are formed, where they travel how fast they travel, their deepening rates, how long they last and ultimately where they decay. In this case, storm tracks are defined as areas with relatively high-frequency of cyclone trajectories.

In the last approach, in which one utilizes a bandpass filter to retain fluctuations in some atmospheric field (e.g. geopotential height or sea level pressure) and with periods corresponding to baroclinic waves, are referred to as bandpass filter methods (e.g. Blackmon (1976), Blackmon et al. (1977)). One of the great advantages of this method compared to the others is that it can easily be performed at all altitudes in the atmosphere, yielding a three-dimensional representation of the storm tracks. Also, it's significantly less computationally demanding than feature point identification or feature point tracking. In this context, storm tracks are defined as maximas in the bandpass variance field.

Unfortunately the terminology of the storm track field is somewhat confusing. As previously mentioned there are multiple storm track definitions. A storm track study will typically choose a definition suited for whatever method is used in that particular study. In addition to multiple storm track definitions, there are multiple ways of referring to the features making up the storm tracks. When using feature point identification and tracking methods, the features constituting the storm track are usually referred to as storms, cyclones or low-pressure centers. In bandpass filter studies, features are often referred to as eddies, transients, perturbations e.t.c. Even though the bandpass variance fields are found to be *dominated* by growing baroclinic waves (Blackmon, 1976), other phenomena with similar timescales, such as anticyclones, will un-

avoidably be included in the field. Therefore, it would be inprecise to refer to the features as storms or cyclones in bandpass variance studies.

2.2 Fundamentals

2.2.1 The general circulation

The general circulation is atmospheric flow averaged over time scales long enough to retain variations longer than that of individual cyclones (Holton, 2004). It is traditionally divided into two parts, the zonal mean and the longitudinal dependent circulation (caused by stationary waves). Held et al. (2002) argues that this is meaningful because separate mechanisms maintain the zonal mean and the stationary wave structure.

The zonal mean

The sun is the primary energy source of the earth. Incoming solar radiation displays a strong latitudinal dependence resulting in an over all energy surplus in the tropics and an energy deficit at the poles. As the earth-atmosphere system is in approximate radiative equilibrium, about the same amount of energy being absorbed by the earth and the atmosphere must also be emitted back into space (in an annual mean). Outgoing planetary radiation, unlike incoming solar radiation, displays only a weak dependence on latitude. Accordingly solar heating sets up a meridional temperature gradient decreasing from the equator towards the poles. For this temperature gradient to cease growing there has to be energy transport from the tropics to the polar regions.

On a non-rotating earth the uneven solar heating sets up a meridional temperature gradient stretching from the equator to the poles in both hemispheres. Excessive tropical heating causes the tropical air to expand vertically relative to the poles, setting up a high-level meridional pressure gradient with high pressure at the equator and low pressure at the poles (Wallace and Hobbs, 2006). Consequently warm tropical air flows down-gradient from the tropics towards the poles. As atmospheric mass is redistributed through meridional transport, surface pressure rises at high-latitudes and drops at low-latitudes (Wallace and Hobbs, 2006). The result is a low-level pressure gradient decreasing towards the equator which acts to transport cold polar air down-gradient. *In the absence of rotation, solar heating gives rise to a hemispheric wide thermally direct circulation (Wallace and Hobbs, 2006).* When including the effects of rotation upon the flow, this is the hemispheric wide version of the famous Hadley circulation (Holton, 2004).

The effects of rotation imposes major changes upon the flow. First of all, Newtons laws are only valid in an inertial frame of reference. Because the earth rotates, it is accelerating and is consequently not an inertial frame of reference. Luckily, there is a way around this problem. By introducing pseudo-forces which compensate for the effects of rotation, Newtons second law may still be applied. These pseudo-forces are the Coriolis force and the centrifugal force. It is standard procedure to "absorb" the centrifugal force into the gravitational force. This is done because centrifugal force exactly bal-

ance the part of the force of gravity which exists because the Earth is not a perfect sphere. The new gravity, defined as the sum of the true gravitational force and the centrifugal force, points towards the center of a perfect sphere and is therefore perpendicular to geopotential surfaces.

The physical explanation for the existence of the Coriolis force is conservation of angular momentum. Consider an air parcel moving at constant altitude from the tropics towards the poles. As the air parcel moves poleward, the distance between the axis of rotation and the air parcel decreases and the air parcel must attain positive zonal velocity to conserve angular momentum. Thus the air parcel is deflected to the right. If the air parcel was moving from pole towards the equator the distance between the air parcel and the axis of rotation would increase and the air parcel would need to attain negative zonal velocity to conserve angular momentum. This is a general result: *in the horizontal, the Coriolis force acts to deflect air parcels to the right in the Northern Hemisphere*. Consult Holton (2004) for a detailed derivation and description of the workings of the Coriolis force in this context.

Thus taking into account the effects of rotation, the Coriolis force modifies the picture of the hemispheric wide thermally direct circulation. As the warm tropical air flows polewards it is deflected to the right (in the positive zonal direction) by the Coriolis force. As the flow becomes increasingly more zonal it continues to be deflected towards the right (now in the negative meridional direction). Eventually the meridional component of the Coriolis force will balance the meridional pressure gradient force yielding geostrophic balance.

The effect of the Coriolis force on the low level flow is similar. As the cold air flows equatorward from the poles it is deflected in the negative zonal direction by the Coriolis force. As the zonal flow becomes increasingly more negative the meridional component of the Coriolis force deflects it in the positive meridional direction, ultimately achieving geostrophic balance at low-levels.

The effects of rotation cause geostrophic balance at midlatitudes. Assuming that the atmosphere is in hydrostatic balance as well (generally a good assumption (Holton, 2004)) and combining with geostrophic balance yields thermal wind balance:

$$\frac{\partial v_g}{\partial(\ln p)} = -\frac{R}{f}\left(\frac{\partial T}{\partial x}\right)_p \tag{2.1}$$

$$\frac{\partial u_g}{\partial(\ln p)} = \frac{R}{f}\left(\frac{\partial T}{\partial y}\right)_p \tag{2.2}$$

where u_g and v_g are the zonal and meridional geostrophic velocities, respectively, R is the gas constant of dry air, f is the Coriolis parameter, p is pressure and pressure is applied as the vertical coordinate.

As can be seen from equation (2.1) the presence of a negative meridional temperature gradient is consistent with the existence of a geostrophic zonal wind which decreases with increasing pressure, that is, increases with height. The stronger the meridional temperature gradient, the stronger the vertical shear of the geostrophic zonal wind. *Due to thermal wind balance, midlatitudes are characterized by geostrophic zonal winds which increase with height.*

As it turns out, when the zonal wind reaches some critical value it becomes *baro-*

clinically unstable (Holton, 2004). When a flow is unstable, small perturbations in the flow will be able to grow by drawing energy from the flow itself. The instabilities that eventually occur in the flow are baroclinic waves. These waves act to transport heat in the meridional direction, and thereby contribute to reducing the meridional temperature gradient.

Because of the existence of baroclinic instability at mid-latitudes, the thermally direct Hadley circulation is confined to the subtopics. Warm air rises in the tropics and flows towards the subtropics. Reaching the subtropics the air sinks and flows back to the tropics at low-levels. In the Northern Hemisphere, the Coriolis force is always working to change the direction of the flow by deflecting it towards the right, preventing purely meridional flow. In the zonal mean, the Hadley circulation is responsible for the meridional heat transport at low-latitudes. At higher latitudes, extratropical cyclones, stationary waves and ocean currents are responsible for the meridional heat transport.

Figure 2.2: *Time mean $Z_{500\,\mathrm{hPa}}$ from a nine winter period from Blackmon (1976). The data is from the NMC analysis for the time period 1963 – 1972 using the winter season only. The winter season is in this case defined as 15. November – 14. March. Contour interval is 50 m.*

Zonal asymmetries

If the boundary condition of the earth was independent of longitude, the zonally averaged circulation would provide a complete picture of the general circulation. But as we know, this is not the case. The presence of continents, mountains, warm oceanic currents etc. provide some of the most important contributors to zonal asymmetry. The picture is complicated by feedback processes due to ocean temperature, albedo and ground wetness (Held, 1983). Also, transient large-scale eddies modify the picture through heat and momentum transport and latent heat release.

The effects of the longitudinal asymmetry on the general circulation can be seen by investigating Figure 2.2 which displays the mean $Z_{500\,\mathrm{hPa}}$ field from Blackmon (1976). Major troughs are found downstream from the Rockies and Himalayas over the east coast of North-America and over Japan. A weaker trough is seen over eastern and middle Europe. Ridges are found in the eastern Atlantic and to some extent in the eastern Pacific upstream from the Rockies.

The stationary waves that constitute the longitudinally dependent part of the general circulation are to a good approximation described by forced stationary Rossby waves (Holton, 2004).

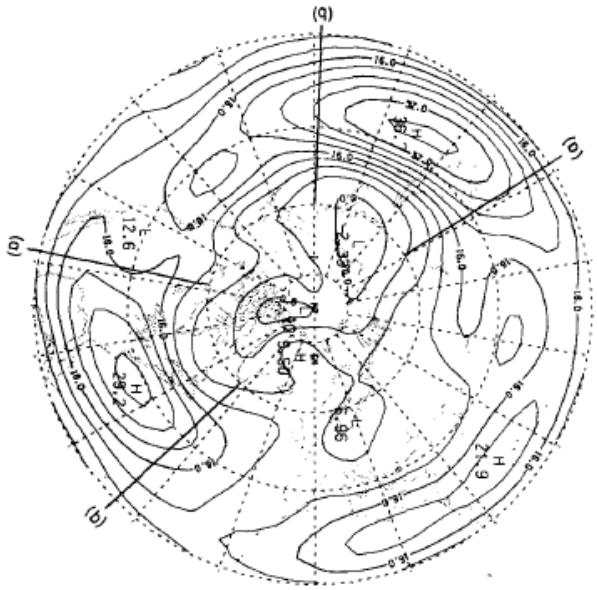

Figure 2.3: *Time mean zonal wind speed at 500 hPa from a nine winter period from Blackmon et al. (1977). The data is from the NMC analysis for the time period 1963 – 1972 using the winter season only. The winter season is in this case defined as 15. November – 14. March.*

2.2.2 The westerlies

Because of the zonally symmetric part of the general circulation (section 2.2.1), there is a band of fast-flowing winds at mid-latitudes (the westerlies) characterized by significant vertical shear. When combining the zonally symmetric and the zonally asymmetric part of the circulation (section 2.2.1) the result is local maximas in the zonal wind field associated with the troughs in the temporally averaged geopotential height field caused by the stationary waves (Holton, 2004). Figure 2.3 shows the winter time mean zonal wind from Blackmon et al. (1977). As should be clear from this figure, the westerlies do indeed exhibit a strong longitudinal dependence, the most evident being the large maximas over the east coasts of North-America and Asia. Notice that the maximas are approximately located in the baroclinic storm track entrance regions and that the maximas coincide with the troughs in the time mean geopotential height field at the same level shown in Figure 2.2, as noted by Blackmon et al. (1977). Notice that Figure 2.3 and Figure 2.2 are taken at the same level and made from the same data.

The polar jet stream (from now on jet stream will refer to the polar jet stream for brevity) is the core of fast-flowing winds found at tropopause level where westerlies reaches maximum strength. The jet stream core is found at about 9 – 12 km altitude with average wind speeds at about 180 km/h.

Ageostrophic circulations

The westerlies induce agestrophic circulations in the plane perpendicular to the mean flow. Figure 2.4 shows a schematic illustration of the time mean circulation for two cross-sections perpendicular to the westerlies located upstream and downstream from the mean flow maximas. The location of the cross sections are marked in Figure 2.3. Consequently (a) is located in a region of acceleration, and (b) is located in a region of deceleration. As seen from the figure, cross section (a) is characterized by a thermally direct meridional circulation with poleward flow at high levels and equatorward flow at low levels. Cross section (b) is characterized by a thermally indirect circulation with poleward flow at low levels and equatorward flow at high levels.

The circulations in Figure 2.4 are consis-

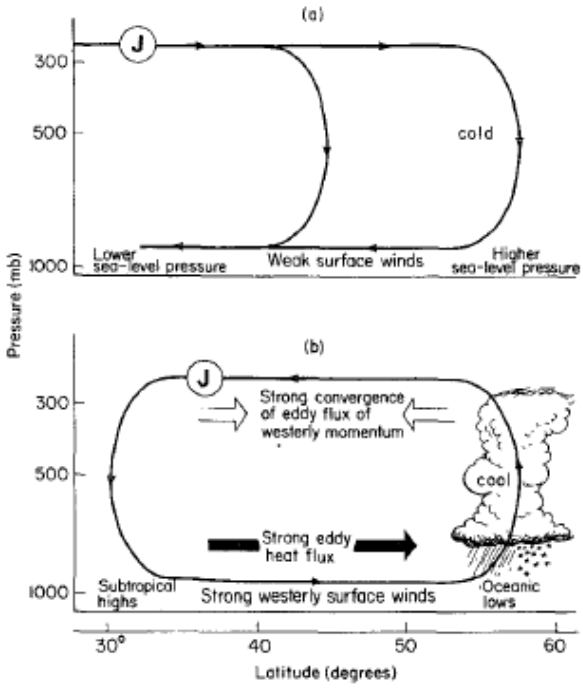

Figure 2.4: *The time mean circulation perpendicular to the westerlies. a) shows the vertical circulation for two cross sections made perpendicular to the jet entrance region where the westerlies are known to accelerate. b) shows the same as a), but for the jet exit region. The locations of the cross sections are marked in Figure 2.3. This figure is from Blackmon et al. (1977).*

tent with what one finds by investigating the ageostrophic wind derived by taking the vertical cross product of the equation of motion and dividing through by the Coriolis parameter (following Martin (2006)):

$$\frac{\vec{k}}{f} \times \frac{D\vec{V}}{dt} = \vec{V} - \vec{V_g} = \vec{V_a} \tag{2.3}$$

Imagine a parcel initially accelerated in the western part of one of the mean flow maximas in Figure 2.3 and neglect the curvature of the flow. From the above equation the ageostrophic velocity must point northward from the location of the parcel. Consequently there is convergence of ageostrophic velocities poleward of the region of acceleration in the westerlies. Convergence at high levels in the atmospheric column indicates sinking and low-level divergence. The ageostrophic velocity vector diverge and indicates rising air in the atmospheric column. This is consistent with the circulation seen in cross section (a) in Figure 2.4. The same arguments can be applied for cross section (b), only the the westerlies are decelerating so the ageostrophic wind vector points south. Thus, from considering the equation (2.3) and a straight jet streak one finds a thermally direct circulation at the entrance region and a thermally indirect circulation at the exit region.

The thermally direct circulation along cross-section (a) has an ageostrophic velocity of about 2 – 3 m/s, which is about an order of magnitude more than the Farrel cell (Holton, 2004). The thermally indirect circulation along cross-section (b) is of about the same magnitude (figure 16 in Blackmon et al. (1977)).

Cyclone – mean flow interactions

The interaction between cyclones and the westerlies is complex. Horizontal and vertical heat transport associated with the cyclones acts to decrease the atmospheric baroclinicity, and thus the vertical wind shear thereby weakening the westerlies. On the other hand, vorticity flux convergence caused by the cyclones at upper-levels seems to act to accelerate the westerlies. Holton (2004)

2.2.3 Baroclinic instability

Baroclinic instability and the subsequent baroclinic growth is commonly accepted as the mechanism responsible for formation of cyclones which are instrumental to the heat transport at mid-latitudes and high-latitudes. This section gives a short descriptive review of baroclinic fluids and the basic principle of baroclinic instability.

As seen in section 2.2.1, solar heating sets up a pole-to-equator temperature gradient in the horizontal. A fluid in which there exists a temperature gradient on a surface of constant pressure is referred to as baroclinic. In a baroclinic fluid, density is a function of pressure and temperature. From thermal wind balance (equation (2.1) and equation (2.2) on page 7), the presence of horizontal temperature gradients allows for vertical wind shear. Figure 2.5(b) illustrates a baroclinic fluid in which the winds are purely zonal and increasing linearly in the vertical.

If the winds do not change with height, as is the case in Figure 2.5(a), the fluid is barotropic. A fluid is barotropic when temperature is constant on constant pressure surfaces. The density then varies with pressure only. From thermal wind balance, the absence of horizontal temperature gradients means that there is no vertical shear. This is a fundamental property of barotropic fluids. The horizontal geostrophic velocities are constant with height. Figure 2.5(a) illustrates a barotropic fluid in which the winds are purely zonal.

Considering a system to be barotropic greatly simplifies things, and is a good approximation in the ocean and the planetary boundary layer. The tropics are also mostly barotropic due to the strong vertical mixing. The mid-latitude atmosphere is on the other hand highly baroclinic in nature. As seen in section 2.2.1, presence of a meridional temperature gradient combined with thermal wind balance yields a westerly flow increasing with height.

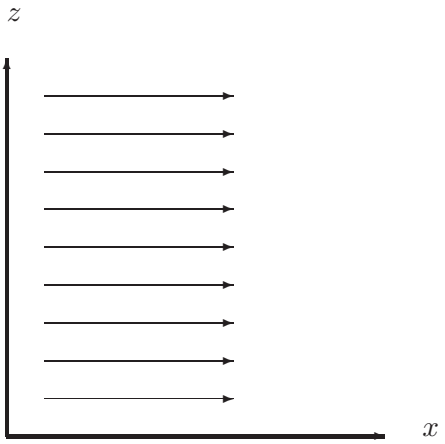

(a) Barotropic fluid: no vertical wind shear. Winds are purely zonal.

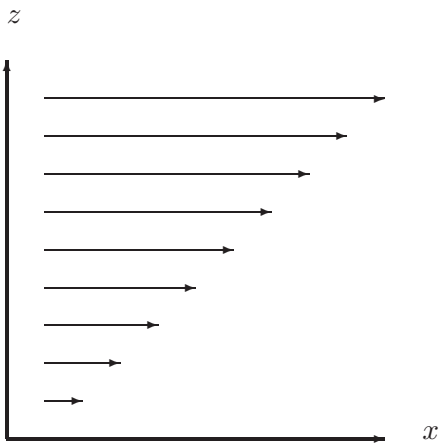

(b) Baroclinic fluid: constant vertical wind shear. Wind speeds are increasing linearly with height and are purely zonal.

Figure 2.5: Examples *vertical wind profiles in a barotropic and a baroclinic fluid.*

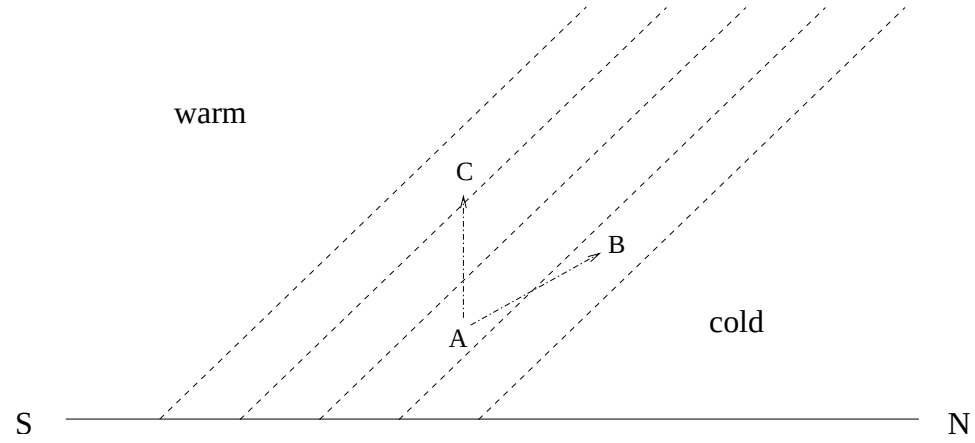

Figure 2.6: *Simplified illustration of slant-wise convection from LaCasce (2008). The stippled lines are isotherms, the letters A, B and C indicate parcel positions and the arrows indicates two possible ways of interchanging them. Parcel A and C are stably stratified and may be interchanged raising the atmospheric center of mass. Parcel A and D are not stably stratified and interchanging them will lower the atmospheric center of mass releasing energy.*

As previously mentioned, a flow is only stable if small perturbations introduced into the flow do *not* amplify in time. It just so happens that in the atmosphere (and ocean) such a stable flow still remains to be found (Vallis, 2005). Under certain circumstances small perturbations will grow into large-scale features, such as cyclones, as they feed on the energy of the mean flow. Cyclones arise because the mid-latitude flow is baroclinically unstable to small perturbations of certain structures. Baroclinic instability does of course demand a baroclinic fluid, but this alone does not suffice. The atmosphere must be stratified in such a way that perturbations may attain kinetic energy through converting atmospheric available potential energy (APE) into kinetic energy.

As the sun heats the earth-atmosphere system it lifts the atmospheric center of mass, increasing the atmospheric APE[1]. Growing cyclones feed upon this energy by interchanging atmospheric mass in such a way as to lower the atmospheric center of mass, thereby releasing APE. (Holton, 2004)

Figure 2.6 illustrates release of APE. The stippled tilted lines are isotherms representing the meridional temperature gradient. Because the temperature gradient has a northward tilt, parcel A and C may be interchanged to increase the APE of the atmosphere. This is because parcel A and C are stably stratified, meaning that parcel A is colder than parcel C. Interchanging the two parcels will lift the atmospheric center of mass. Parcel A and B on the other hand are not stably stratified. Parcel B is colder than parcel A and interchanging the two will lower the atmospheric center of mass and release energy. This is called "slant-

[1]Notice that the APE is the part of the total potential energy (the sum of the potential and internal energy) of the atmosphere that may be converted into kinetic energy. Even though the atmosphere has a huge amount of potential energy only a small fraction of this is considered to be APE. According to Holton (2004) about 0.5% of the total potential energy is available.

wise convection" and is the basic idea of how storms feed on the energy of the mean flow.

2.2.4 Extra-tropical cyclones

This section provides a short descriptive review of some of the most important aspects of the cyclone life cycle following Martin (2006). For a more complete description, consult a textbook in dynamical meteorology such as Holton (2004) or Martin (2006).

Cyclogenesis

As described in section 2.2.3, cyclones start off as small perturbations in the mean flow and grow by extracting energy from it through slant-wise convection.

Nearly all cyclones develop from disturbances in the upper-level flow. The disturbance starts off as a vorticity maxima, and is advected eastward by the westerlies. The geopotential height axis of developing cyclones tilt in the vertical. The upper-level low-pressure center of a growing cyclone is typically located upstream from the low-level low-pressure center. This tilt is instrumental to their ability to intensify. Figure 2.7 from Martin (2006) shows a upper level trough-ridge wave train. The dark arrows are the acceleration vectors of the flow. For example, the black arrow between point A and B represent the acceleration an air parcel must have following the geopotential height contours from point A to B. The dark gray arrows are the ageostrophic wind vectors found from equation (2.3) on page 10. C, D, H and L refers to regions of convergence, divergence, high-pressure and low-pressure, respectively. Upper-level divergence is associated with rising air in the atmospheric column and low surface pressure. Consequently the low-level low-pressure center is located downstream from the upper-level low-pressure center and beneath a region of upper-level divergence. The geopotential height axis of cyclones tilt in the vertical into the wind shear.

As a surface cyclone intensifies, the sea level pressure decreases. The meridional winds associated with the cyclone cause southward warm air advection southwest of the cyclone (producing a thermal trough) and northward cold air advection northeast of the cyclone (producing a thermal ridge). The resulting deformation of the isotherms gives rise to the warm and cold fronts. From this perspective cyclogenesis and frontogenesis (the formation of fronts) are almost concurrent processes. In this way cyclones transport heat in the meridional.

Post-mature stage

Traditionally, the post-mature stage is characterized by the introduction of the occluded front. In the Norwegian cyclone model, the occlusion was thought to happen as a result of the cold front catching up with the warm front, forcing the warm air upwards. If the cold air behind the cold front was denser than the cold air ahead of the warm front, the warm front would be pushed on top of the cold front and there would be cold occlusion. If, on the other hand, the cold air ahead of the warm front was denser, the warm front would undercut the cold front and there would be warm occlusion. The upward displacement of warm moist air from the warm sector of the cyclone acts to reduce the atmospheric center of mass by placing warm air on top of cold air. The cyclone transports heat vertically.

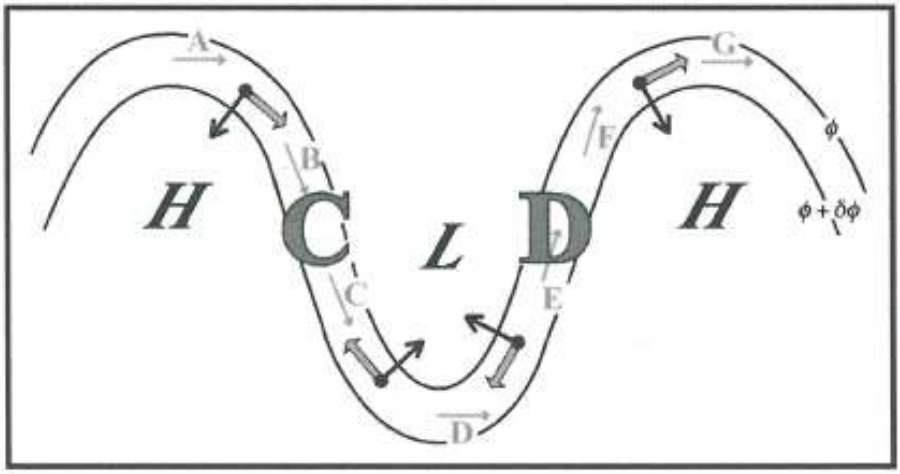

Figure 2.7: *This figure is a schematic illustration of an upper-level trough-ridge wave train in which the traveling velocity is the same everywhere. The black arrows are vectors of acceleration, the dark gray arrows are the ageostrophic wind vectors, and the light gray vectors are the wind vectors. C and D denotes regions of convergence and divergence, respectively. Figures is from Martin (2006)*

Cyclosis

The vertical tilt of the geopotential height axis is necessary for the continued intensification of the cyclone. As the cyclone develops and matures, the upper-level cyclone catches up with the surface cyclone yielding a more barotropic structure. The ultimate consequence of this is that the upper-level divergence previously positioned above the surface cyclones moves downstream and can no longer act to remove air from the atmospheric column. As surface friction causes air to flow into the surface cyclone, pressure will rise as there is no mechanism evacuating air from the atmospheric column above it. The vertical alignment of the upper-level and surface cyclone marks the beginning of cyclosis.

Effects of diabatic heating

Diabatic heating has the power to greatly influence and alter several cyclone properties e.g. intensification rate, life time and maximum intensity. For example, diabatic heating from the Gulf Stream and the Kuroshio can potentially yield so-called "explosive cyclones", which intensify more rapidly and for longer time periods than ordinary cyclones. This happens because the warm boundary currents reduce the atmospheric static stability which allows for more vigorous vertical motions and thereby an intensified cyclogenesis process.

Diabatic heating from latent heat release caused by precipitation processes associated with the cyclones themselves can also greatly influence the cyclogenesis. Potential effects of latent heat release are: energy may be added to the surface cyclone, the static stability of the overlying atmo-

sphere may be reduced in narrow regions due to saturated updrafts, and finally the large-scale structure and dynamics of the atmosphere may be effected causing positive feedback on the cyclogenesis.

2.2.5 The Eady parameter

The Eady parameter of maximum baroclinic growth is a popular measure of atmospheric baroclinicity. The Eady parameter is a growth rate, usually given in terms of day^{-1}, which tells you how fast baroclinic waves amplify.

The Eady parameter descends from linearized models of baroclinic instability, like the Eady model. The Eady model is a model of baroclinic growth and probably the simplest of its kind. A more detailed review of the Eady model, including mathematical derivations, is given in Appendix B on page 113, and will therefore not be given here. In short, the Eady model utilizes the linearized adiabatic quasi-geostrophic potential vorticity equation and the linearized adiabatic quasi-geostrophic temperature equation with the f-plane approximation, a constant Brunt-Väisälä frequency, the rigid lid approximation and a constant vertical wind shear. Notice that the f-plane approximation is the β-plane approximation without the β term, meaning that there is no planetary vorticity in the Eady model. Another special thing about the Eady model is that the mean flow $\bar{u}$ does not have any vorticity either. Because there is no inner vorticity, baroclinic growth only occurs when temperature anomalies on the upper and lower boundary are allowed to interact with each other and amplify in time. As is standard procedure, a Fourier component on the form $\psi = \hat{\psi}(z)\cos(ly)e^{kc_i t}e^{ik(x-c_r t)}$ is applied representing the streamfunction, meaning that the wave will amplify in time if the growth rate, kc_i, is positive (see Appendix B). In the case of amplifying waves, the growth rate is given by (see Appendix B):

$$kc_i = \frac{k\Lambda}{\alpha}\left[\coth(\frac{\alpha D}{2}) - \frac{\alpha D}{2})\right]^{\frac{1}{2}} \times \left[\frac{\alpha D}{2} - \tanh(\frac{\alpha D}{2})\right]^{\frac{1}{2}} \tag{2.4}$$

where k is the zonal wave number, c_i is the imaginary phase speed, Λ is the wind shear (a constant), D is the fluid wind shear, and $\alpha = \sqrt{\frac{N^2(k^2+l^2)}{f_0^2}}$.

So, the rather messy looking equation above states the growth rate of baroclinic waves in the Eady model. As previously mentioned, the Eady parameter is another measure of baroclinic growth. It measures the largest growth rate of the most unstable wave. The exact mathematical expression can be traced back to Lindzen and Farrell (1980), and has been used with small modifications by among others Hoskins and Valdes (1990), Chang and Orlanski (2002) and Yin (2005). Though the exact form of the expression vary somewhat from study to study, the Eady parameter is generally the product of the meridional temperature gradient and the inverse Brunt-Väisälä frequency, multiplied by some constant. The meridional temperature gradient is often exchanged by the vertical wind shear. The various Eady parameter from the respective articles are given in Table 2.1.

Comparing the equations of the Eady parameter with growth from the eady model in equation (2.4), it can be seen that they are rather similar. The growth rate from the Eady model is proportional to $\frac{k\Lambda}{\alpha} =$

Table 2.1: *Various Eady parameters.* $\sigma_{B1} = (kc_i)_{\max}$ *is the maximum growth rate of the most unstable wave, also known as the Eady parameter,* g *is the acceleration of gravity,* a *is the radius of the Earth,* T *is the temperature,* $\bar{T}$ *is the zonal mean temperature,* u *is the zonal velocity,* $\vec{v}$ *is the horizontal velocity vector,* N *is the Brunt-Väisälä frequency and* f *is the Coriolis parameter.*

Article	**Eady parameter**
Lindzen and Farrell (1980)	$\sigma_{B1} = -\left(0.3125 \times \frac{g}{aTN}\right) \frac{\partial T}{\partial \phi}\vert_{z=0}$
Hoskins and Valdes (1990)	$\sigma_{B1} = 0.31 \frac{f}{N} \vert \frac{\partial \vec{v}}{\partial z} \vert$
Yin (2005)	$\sigma_{B1} = 0.31 \frac{g}{NT} \vert \frac{\partial T}{\partial y} \vert$
Chang and Orlanski (2002)	$\sigma_{B1} = \frac{f}{N} \frac{\partial \bar{u}}{\partial z}$

$\frac{f_0 k \Lambda}{N\sqrt{(k^2)}} = \frac{f_0}{N} \frac{\partial \bar{u}}{\partial z}$ (assuming $l = 0$) which almost identical to the expression used in Chang and Orlanski (2002) .

Figure 2.9 on page 18 from Hoskins and Valdes (1990) shows the horizontal distribution of the Eady parameter on the 780 hPa surface using the expression from Table 2.1. (This figure will be discussed further in section 2.3.1). As will be seen later, maxima in the Eady parameter coincide with the storm track entrance regions which are known for strong baroclinic growth. Making a quantitative comparison between the values in this figure and corresponding values for the most unstable wave of the Eady mode, the agreement is rather good. The largest values in Figure 2.9 are found in the Pacific storm track entrance region and are about 1/day. From Figure B.2 the maximum growth rate of the Eady model is about 0.73/day.

The following will be applied as the Eady parameter:

$$\sigma_{B1} = 0.31 \frac{g}{NT} \vert \frac{\partial T}{\partial y} \vert \tag{2.5}$$

It is similar to the expression from Yin (2005), but the temperature is not generally taken as a zonal average.

The Brunt-Väisälä frequency is given by (Holton, 2004):

$$N = \sqrt{g \frac{\partial \theta}{\partial z}}$$

where θ is the potential temperature.

Assuming hydrostatic balance, the Brunt-Väisälä frequency may be written as follows (Holton, 2004):

$$\begin{aligned} N &= \sqrt{\frac{g}{T}\left(\frac{\partial T}{\partial z} + \frac{g}{c_p}\right)} \\ &= \sqrt{\frac{g}{T}\left(g\frac{\partial T}{\partial \Phi} + \frac{g}{c_p}\right)} \\ &= g\sqrt{\frac{\partial \ln T}{\partial \Phi} + \frac{1}{T c_p}} \end{aligned}$$

where Φ is the geopotential and c_p is the specific heat at constant pressure.

Now, the Eady parameter may be written as:

$$\sigma_{B1} = \frac{0.31}{T} \frac{\vert \frac{\partial T}{\partial y} \vert}{\sqrt{\frac{\partial \ln T}{\partial \Phi} + \frac{1}{T c_p}}} \tag{2.6}$$

"Decomposition" of the Eady parameter

Now, as can be seen from equation (2.5), the Eady parameter changes by one of two processes: either the meridional temperature gradient changes or the Brunt-Väisälä frequency changes. The contribution made to the Eady parameter by the meridional temperature gradient is defined as:

$$\sigma_{B1,dT/dy} = 0.31 \frac{g}{T} \frac{|\frac{\partial T}{\partial y}|}{N_{\text{reference}}} \tag{2.7}$$

where $\sigma_{1B,\,dT/dy}$ is the contribution to the Eady parameter from the meridional temperature gradient and the $N_{\text{reference}}$ is a reference value of the Brunt-Väisälä frequency. The reference value will be taken as a temporal and spatial average of the Brunt-Väisälä frequency. In this way, any variation in $\sigma_{1B,\,dT/dy}$ will be caused by the meridional temperature gradient.

Similarly, the contribution from the Brunt-Väisälä frequency is given by:

$$\sigma_{B1,N} = \frac{0.31}{T} \frac{|\frac{\partial T}{\partial y}|_{\text{reference}}}{\sqrt{\frac{\partial \ln T}{\partial \Phi} + \frac{1}{T c_p}}} \tag{2.8}$$

where $\sigma_{1B,N}$ is the contribution to the Eady parameter from the Brunt-Väisälä frequency and $|\frac{\partial T}{\partial y}|_{\text{reference}}$ is a reference value. As with $N_{\text{reference}}$, $|\frac{\partial T}{\partial y}|_{\text{reference}}$ will be taken as a temporal and spatial average of $\frac{\partial T}{\partial y}$. Now, any change in $\sigma_{1B,N}$ will be a caused by the Brunt-Väisälä frequency.

This decomposition of the Eady parameter into one part representing the contribution from the meridional temperature gradient and another representing the contribution from the Brunt-Väisälä frequency will be utilized later in section 2.4.4 and in chapter 5.

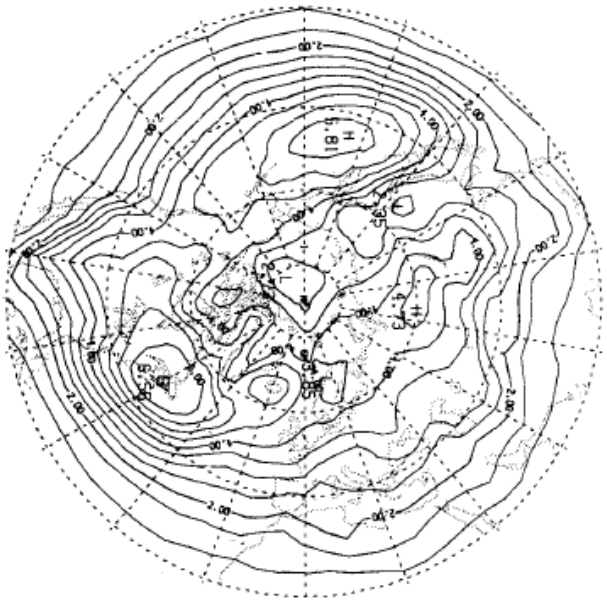

Figure 2.8: *Bandpass variance SLP field from Blackmon et al. (1977) using NCEP analysis data for the time period 1963 – 1972 using winter months only. Winter is defined as 15. November – 14. March.*

2.3 Storm track structure and maintenance

2.3.1 Storm track structure

Using the traditional bandpass variance SLP field to define the storm tracks, they are easily picked out as two large maxima in the bandpass variance field. Figure 2.8 shows the bandpass variance of the SLP from Blackmon et al. (1977). The figure clearly shows two maxima, one in

the North-Pacific and another in the North-Atlantic constituting the Pacific and North-Atlantic storm tracks, respectively. The Pacific storm track stretches from the east coast of Asia across the Pacific and the North-Atlantic storm track stretches from the east coast of North-America across the North-Atlantic. Notice that the North-Atlantic storm track is more tilted than the Pacific.

Storm track entrance region

It is commonly accepted that baroclinic conversion of atmospheric APE tied to the meridional temperature gradient is the primary energy source of extratropical cyclones. Cyclogenesis is expected to be initiated when perturbations of certain structures are found in areas of relatively high baroclinicity. As seen in section 2.2.5, the Eady parameter is a much used measure of atmospheric baroclinicity.

Figure 2.9 shows the mean Eady parameter at the 780 hPa surface for Northern Hemisphere winter, from Hoskins and Valdes (1990). Strongly baroclinic regions, marked by the stippling, are found at the Asian and North American east coasts where the land-ocean heat contrasts cause large local meridional temperature gradients. Consistent with extratropical cyclones originating from baroclinic instability, the maxima in the Eady parameter and bandpass variance fields are found in approximately the same geographical areas. But as noted by Hoskins and Valdes (1990), the Eady parameter tends to reach its maximum values slightly upstream from the maxima in the bandpass variance fields. This can be seen by comparing Figure 2.8 and Figure 2.9 (though it must be kept in mind that the two figures are made from different data).

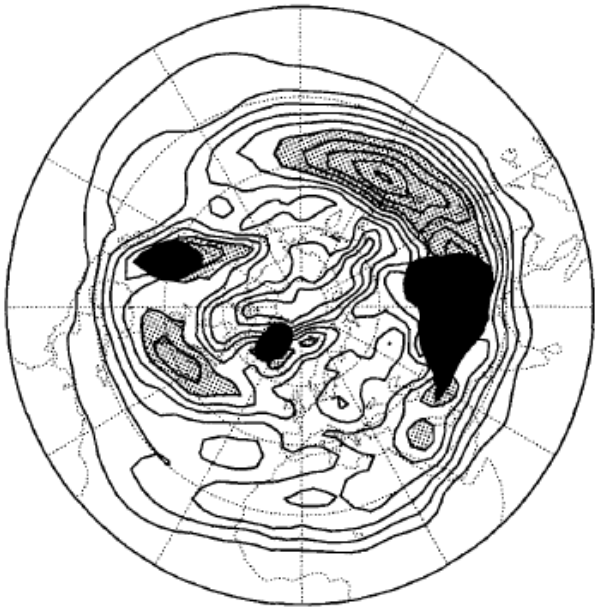

Figure 2.9: *Eady parameter at approximately 780 hPa for the Northern Hemisphere winter. Unit is day^{-1} and the contour interval is 0.1 day^{-1} (increasing from zero at the equator). Stippling implies values greater than 0.6 day^{-1} and black regions indicates orography within 1 km of the pressure level applied for the calculations. The figure is from Hoskins and Valdes (1990). The data is from a linear stationary wave model.*

However, the relationship between atmospheric baroclinicity and baroclinic wave activity is not completely straightforward. In the Pacific, Nakamura (1992) found that although the atmospheric baroclinicity in the Pacific reaches its peak value during midwinter, baroclinic wave activity is actually stronger during autumn and spring. This strongly differs from the North-Atlantic where both baroclinic wave activity and atmospheric baroclinicity reaches peak values at midwinter. Nakamura (1992) suggests that this is somehow connected to

the strength of the jet stream as it reaches greater values over then Pacific than over the Atlantic. Over the North-Atlantic, the jet stream rarely exceeds 45 m/s, while over the Pacific the midwinter jet reaches values of about 65 m/s at midwinter.

Barotropic effects in the entrance region, such as horizontal shear, can also contribute to making the atmosphere favorable for cyclogenesis.

Storm track exit region

As noted by Hoskins and Valdes (1990), the storm track exit region is found in the eastern ends of the North-Atlantic and Pacific in areas where the Eady parameter is relatively small. Thus the atmosphere is not particularly baroclinic in the storm track exit region. Figure 2.9 shows that the storm track exit region is characterized by low baroclinicity. It is intuitive not to expect strong cyclogenesis in these regions.

Traditionally, it is thought that baroclinic eddies undergo baroclinic growth and barotropic decay (Martin, 2006). The eddies themselves are initially baroclinic in nature as they tilt in the vertical into the vertical shear of the mean flow. The low-level low-pressure center is located downstream compared to the upper-level low-pressure center. As the eddies mature the upper level low-pressure center "catches up with" the low-level low-pressure center yielding a more barotropic structure (see section 2.2.4).

It is not just regional variations in atmospheric baroclinicity that affect the storm track structure. Regional variations in barotropic deformation has a pronounced affect on the baroclinic eddies, particularly in the storm track exit region (Black and Dole, 2000). As shown by Black and Dole (2000), baroclinic growth and deformation are of about the same order.

As defined by Black and Dole (2000): "deformation is a local measure of the rate of change in the shape of a fluid element as a result of spatial variations in the velocity field". The total deformation field is the sum of the stretching deformation ($F_1 = \frac{\partial u}{\partial x} - \frac{\partial v}{\partial y}$) and the shearing deformation ($F_2 = \frac{\partial v}{\partial x} + \frac{\partial u}{\partial y}$) (Martin, 2006). Figure 2.10 illustrates deformation fields found in the jet stream. Figure 2.10(a) illustrates stretching deformation in the jet entrance region, Figure

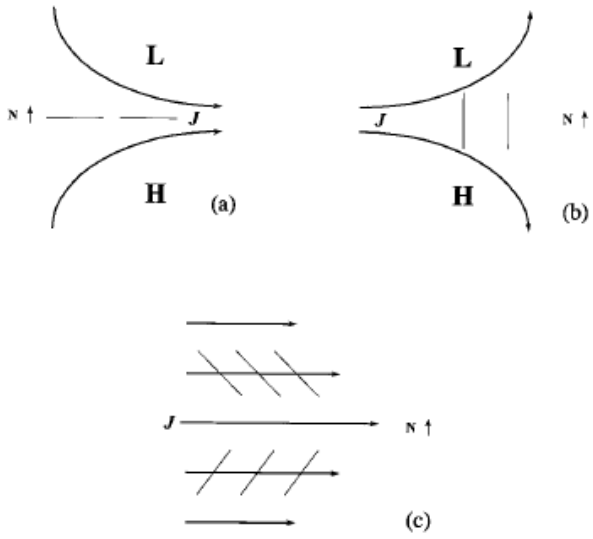

Figure 2.10: *Examples for deformation in the jet stream from Black and Dole (2000). (a) illustrates stretching deformation at the jet entrance region, (b) illustrates stretching deformation at the jet exit region, and (c) illustrates the shearing deformation around the jet stream core. Heavy arrows are streamlines, thin lines are the axes for dilatation and J indicates the meridional position of the jet stream.*

2.10(b) illustrates stretching deformation in the jet exit region, and Figure 2.10(c) illustrates the shearing deformation around the jet stream core. The thin lines in Figure 2.10 are the axis' of dilatation, which is the axis of maximum stretching. Eddies have a tendency to be kinematically stretched along the axis of dilatation (Black and Dole, 2000). It is clear from the figure that an eddy will be kinematically stretched in the zonal direction in the jet entrance region and in the meridional direction in the exit region. Shearing deformation around the jet stream core acts to elongate the eddies in the SW-NE direction south of the jet stream and the NW-SE direction north of the jet stream (Black and Dole, 2000).

2.3.2 Maintenance

Storm tracks are localized regions experiencing high-frequency cyclone activity. Regardless of whether this cyclone activity is measured in terms of number of observed low-pressure centers, number of observed cyclone trajectories or bandpass variance one may wonder why the storm tracks exist. Why is there a localized region where the cyclones travel?

Cyclones feed on the baroclinicity of the atmosphere. They act to transport heat both meridionally and vertically. Thus, cyclones reduce atmospheric baroclinicity. So if cyclones both reduce atmospheric baroclinicity and depend on it to grow, why do they follow one another in a storm track? Why would there be a band of cyclones stretching across the North-Atlantic and Pacific oceans? What is it that maintains the storm track?

Several scientists have asked similar questions. Studies generally attribute storm track maintenance to two things: diabatic heating (Hoskins and Valdes, 1990) and mountains (Broccoli and Manabe, 1992).

Hoskins and Valdes (1990) investigated the effect of the horizontal and vertical heat transport associated with cyclones, the vorticity flux associated with cyclones and diabatic heating on atmospheric baroclinicity using a linear stationary wave model. They found that the major contributor to increasing atmospheric baroclinicity to be diabatic heating. True, cyclones did reduce baroclinicity through transporting heat vertically and meridionally and increase baroclinicity through the vorticity fluxes by forcing the mean flow, but the effect of diabatic heating was by far the dominating one.

So, Hoskins and Valdes (1990) found the storm tracks to be maintained by diabatic heating. They argue that the enhanced baroclinicity in the storm track entrance region exist because of three things:

1. Storm track activity is greatest downstream from the areas of greatest baroclinicity, so the cyclones may not really be that effective at reducing the baroclinicity in these regions.
2. Latent heating in the storm track region associated with the cyclones themselves is responsible for increasing the atmospheric baroclinicity.
3. Cyclones cause low-level flows that forces the Gulf Stream and the Kuroshio current. These western boundary currents are responsible for enhanced baroclinicity due to land-ocean heat contrasts.

As mentioned, another view is that the

storm tracks are maintained by the mountains upstream. Broccoli and Manabe (1992) investigated the influence of orographically-induced stationary waves and found that without orography the Northern Hemisphere storm tracks were circumpolar with only one great maxima stretching across the Pacific and North Atlantic. This was in spite of the fact that the land-ocean heating contrasts remained intact in the runs. In the runs with realistic orography the storm tracks were considerable more asymmetric displaying one maxima in the Pacific and one in the North-Atlantic. If remote features such as orography are vital to storm track organization, the storm track cannot be said to be self-maintaining.

2.3.3 Cyclone life cycle within the storm track region

Traditionally, it has been thought that cyclones would originate in the storm track entrance region, propagate downstream following the mean flow to the storm track exit region, and finally undergo cyclosis (Chang and Orlanski, 2002). Thus, cyclogenesis would generally occur in the storm track entrance region and cyclosis would occur in the storm track exit region.

Recently, Lagrangian storm track studies has revealed that cyclogenesis and cyclosis actually occur to some extent throughout the storm track region (Bengtsson et al., 2006). In Lagrangian storm track studies, each individual cyclone is tracked from cyclogenesis to cyclosis using some feature point tracking routine. There is a widespread use of the traditional SLP field in such studies (e.g. Gulev et al. (2001), Wang et al. (2006)). But it is argued that the vorticity field is a better choice for feature tracking as it is less influenced by the large-scale flow and captures the cyclones at an earlier stage in their life cycle (Hoskins and Hodges, 2002).

Figure 2.11 from Hoskins and Hodges (2002) show cyclogenesis and cyclosis densities found from applying feature point tracking to the relative vorticity field at the 850 hPa pressure surface using reanalysis data and operational data (for later years) from the European Center for Medium-Range Weather Forecasts (EMCWF). As can be seen from the figure, cyclogenesis preferentially occur over Mongolia, southeast China, from east of Japan and downstream along the Pacific storm track, downstream from the Rockies, northeast of Cape Hatteras and in a band stretching towards Ireland, southwest of Greenland, north of Greenland (associated with small-scale features), the Barents Sea, western Mediterranean and the Caspian Sea (Hoskins and Hodges, 2002). The cyclogenesis density maxima found east of Japan and northeast of Cape Hatteras are the traditional cyclogenesis regions in the storm track entrance regions where large baroclinicity is caused by the land-ocean heat contrasts. Cyclosis preferentially occur along the west coast of North-America, in an area stretching from east of the Great Lakes to Hudson Bay and then to Iceland, the Norwegian Sea and Barents Sea, the eastern Mediterranean and Middle East and Siberia (Hoskins and Hodges, 2002). Results are consistent with the findings of Bengtsson et al. (2006).

Further investigation by Hoskins and Hodges (2002) reveal the following:

- Cyclones originating over Mongolia are in general weak systems and undergo

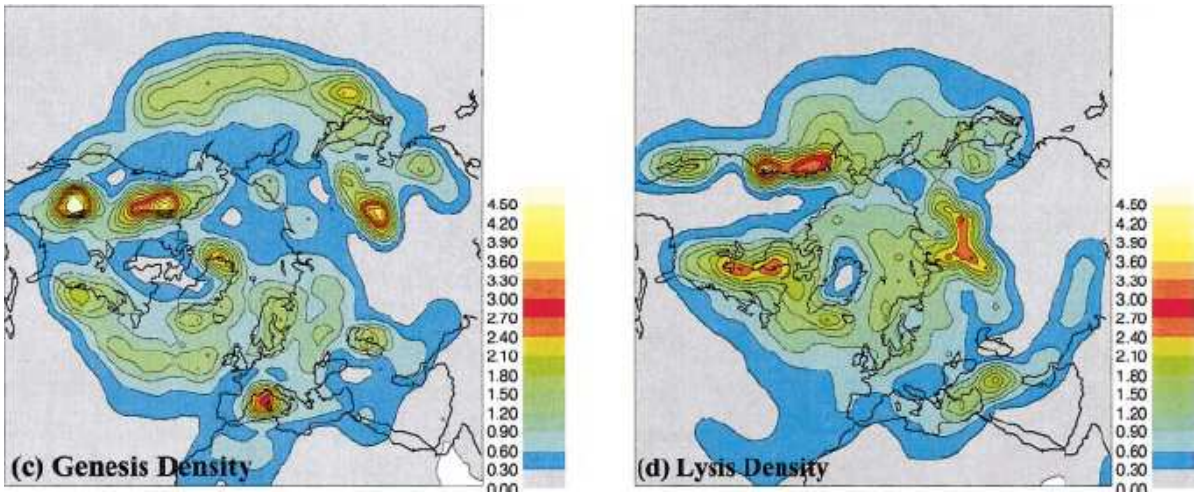

Figure 2.11: *(c) shows cyclogenesis density and (d) showed cyclosis density from Hoskins and Hodges (2002). Fields where derived using a Lagrangian feature point tracking approach on the relative vorticity field on the 850 hPa pressure surface.*

cyclosis over the eastern part of China or the Sea of Japan.

- Cyclones originating over the southeast of China seldom make it further than east of Japan.
- The cyclones resulting from cyclogenesis over the traditional baroclinic region east of Japan undergo cyclosis in the central or North-Pacific.
- Cyclones undergoing cyclosis along the west coast of North-America originate in the middle and eastern parts of the Pacific.
- The cyclones originating downstream from the Rockies generally undergo cyclosis over the North-American continent. A few make it as far as Greenland.
- Most cyclones originating east of Cape Hatteras, in the traditional North-Atlantic cyclogenesis region, decay south of Greenland, while a few make it all the way to the Norwegian Sea.
- The cyclones responsible for the cyclosis maxima over Siberia originate over the Caspian Sea, the Norwegian Sea and the eastern Baltic.

Thus it appears that the cyclones generated over continental North-American and Asian continents do not make it far into the traditional storm track regions. Also, results are in contrast to the traditional view that cyclones originate along the east coasts of North-America and Asia, propagate downstream along with the jet stream and undergo cyclosis in the Norwegian Sea and the Barents Sea. It seems that the majority of the cyclones originating from the traditional cyclogenesis areas mostly decay somewhere around the middle of the storm track regions. It appears that cyclones are also generated in the middle of the storm track region in areas that are not particularly baroclinic measured by e.g. the Eady

parameter (see figure 2.9). A possible mechanism responsible for cyclogenesis in such regions is described in the following.

2.3.4 Downstream development

Traditionally one envisioned the cyclones going through one complete life cycle within the storm track region with baroclinic growth in the entrance region and barotropic decay in the exit region (Chang and Orlanski, 2002). As already seen, this description does not hold for individual cyclones within the storm track. Now, the question is by which mechanism the cyclones generated in the middle of the storm track regions are able to grow into full cyclones. A hypothesis is that in the middle part of the storm track, cyclones retrieve energy from cyclones upstream, a possess referred to as *downstream development* (Chang and Orlanski (1993) and Chang and Orlanski (2002)).

Chang and Orlanski (1993) studied storm track dynamics using an idealized primitive equation model. From their results, the cyclone life cycle in the storm tracks can be described as follows:

Entrance region: at the entrance region disturbances associated with the nonlinear wave packets aloft are amplified by the baroclinicity and initiate type B[2] cyclogenesis. The disturbances are situated in the upper troposphere. Baroclinic conversion dominates the storm track entrance region.

Downstream development region: leaving the entrance region, eddy growth is dominated by transferred energy from the eddies upstream. Thanks to downstream development, eddies are developed and maintained even though they are far away from the highly baroclinic areas off the east coasts of Asia and North America. Downstream development allows for the storm track to extend far into areas which are not necessarily favorable for cyclogenesis.

Exit region: Chang and Orlanski (1993) identified several processes responsible for storm track termination. Areas of enhanced surface friction acts as an energy drain for the eddies, leaving less energy to be "recycled." Also, at the exit region the jet stream decelerates in the zonal direction. The resulting barotropic shear acts to drain energy from the eddies.

2.4 Storm track variability and trends

Synoptically, cyclones are responsible for most severe weather events at midlatitudes. Changes in the storm tracks, whether in terms of a shift in the geographical position or changing intensity, will lead to anomalous patterns of e.g. wind and precipitation. Climatically, cyclones contribute to meridional and vertical transport of heat, momentum and water vapor

[2]Type B cyclogenesis is defined as cyclogenesis initiated by a well-defined disturbance aloft which triggers low-level cyclogenesis when it passes over sufficiently baroclinic areas (Martin, 2006). This runs counter to type A cyclogenesis in which low-level baroclinic waves amplify in the absence of an upper-level disturbance (Martin, 2006). According to Martin (2006), there is a general agreement that most cyclones develop from type B cyclogenesis.

at mid-latitudes (Bengtsson et al., 2006). Any change will possibly lead to anomalous fluxes of these quantities.

Global warming being a major concern these days, numerous studies investigating the effects of increased levels of greenhouse gases on the storm tracks have been performed (e.g. Yin (2005)). To be able to properly interpret the results of such studies, the importance of assessing the natural variability the storm tracks cannot be overemphasized. Without proper knowledge of the natural variability of storm tracks, it is very difficult to assess the true effect of e.g. increased levels of CO_2 in the atmosphere.

Storm tracks are known to undergo seasonal and interannual variability as they change in response to changes such as variation in the meridional temperature gradient (Chang and Orlanski, 2002) and modes of variability like the El Niño-Southern Oscillation (ENSO) (Lau, 1997). A complicating factor is that storm tracks anomalies are also known to be closely tied to anomalies in the low-frequency atmospheric flow through two-way interactions (Branstator, 1992). Branstator (1992) showed that anomalies in the large-scale low-frequency atmospheric flow are caused by anomalies in the storm track using a linear stationary wave model. Later, Branstator (1995) proved the opposite to be true as well as his studies showed that anomalies in the storm tracks are caused by the low-frequency anomalies themselves.

2.4.1 Seasonal variability

Both the location and intensity of the storm tracks vary with the seasons along with the meridional temperature gradient, atmospheric baroclinicity and local diabatic heating. During Northern Hemisphere summer, increased insolation at high-latitudes leads to a decreased temperature gradient and consequently decreased vertical wind shear. In terms of bandpass variance, the storm track will experience decreased intensity during the summer months compared to the winter months (Nakamura, 1992). Also, the storm track maxima are placed further north during summer than winter in both the Atlantic and the Pacific (Nakamura, 1992). Figure 2.12(a) shows baroclinic wave activity in terms of highpass RMS geopotential height at the 250 hPa level as a function of time and latitude. The upper figure shows the Pacific and the lower figure shows the Atlantic. The figures clearly illustrate that within each domain the zonally averaged peak baroclinic wave activity shifts meridionally in time. The peak values shift towards the equator during the autumn and winter months, are farthest south around January, and subsequently migrate north. The storm tracks are farthest north around August. In the Atlantic, baroclinic wave activity is greatest during midwinter while in the Pacific baroclinic wave activity has two maxima, one in November and another in April. The Pacific storm track also seems to experience more migration in the meridional compared to the North-Atlantic storm track (Nakamura, 1992).

As previously mentioned, changes in latitude and intensity of the storm tracks are tied to changes in the atmospheric baroclinicity which is expected to be at its greatest during midwinter when the meridional temperature gradient is largest. Figure 2.12(b) from Nakamura (1992) shows the atmospheric baroclinicity as a function of

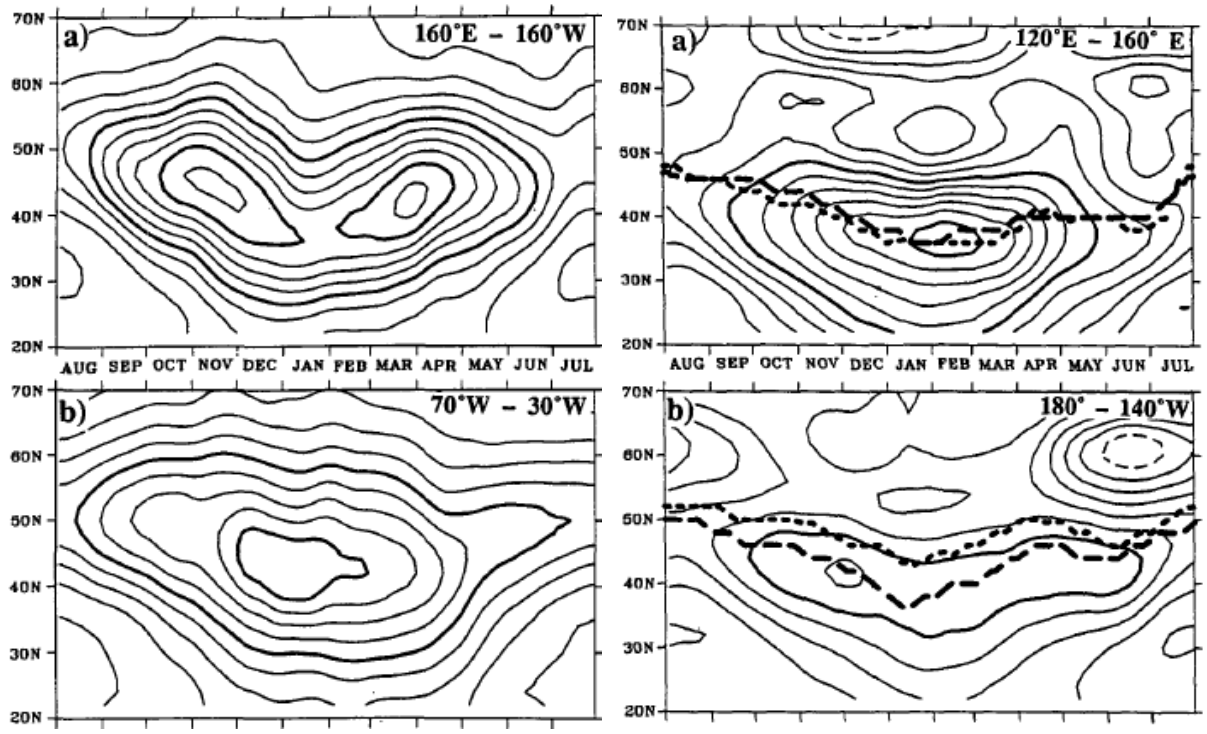

(a) Baroclinic wave activity (b) Atmospheric barclinicity

Figure 2.12: *The figures on the left show the "seasonal march" of baroclinic wave activity in terms of highpass RMS geopotential height field at the 250 hPa level as a function of latitude and time. The highpass filter retains fluctuations with periods within a week. a) shows the Pacific and b) shows the Atlantic. Contour interval is 10 m. Thick lines indicates 80 m and 120 m. The figures on the right show the atmospheric baroclinicity in terms of the Richardson number* ($\mathrm{Ri}^{-\frac{1}{2}} = N^{-1}\frac{\partial U}{\partial z}$) *taken at the 850 hPa and 700 hPa levels, details of how the Richardson number is computed are given in the appendix of Nakamura (1992). a) shows the Atlantic. b) Shows the Pacific. Contour interval is 0.04. Dashed lines indicate the storm track axis in terms of Z250 and dotted lines indicate the storm track axis in terms of SLP as defined in Nakamura (1992). Both figures are from Nakamura (1992).*

time and longitude, the upper figure being for the Atlantic region and the lower figure being for the Pacific region. It is clear from this figure that atmospheric baroclinicity, like baroclinic wave activity, varies in magnitude and latitude. The atmospheric baroclinicity reach its peak value in January – February as expected. The maxima also travels north during spring and back south during fall. It is unknown exactly why the baroclinic wave activity in the Pacific does reach its maximum value when the atmospheric baroclinicity is largest (Nakamura, 1992), (Chang and Orlanski, 2002).

2.4.2 Interannual variability

The ENSO phenomena is perhaps the most well-known mode of SST variability on interannual timescales. ENSO is associated with pronounced SST anomalies in the east-

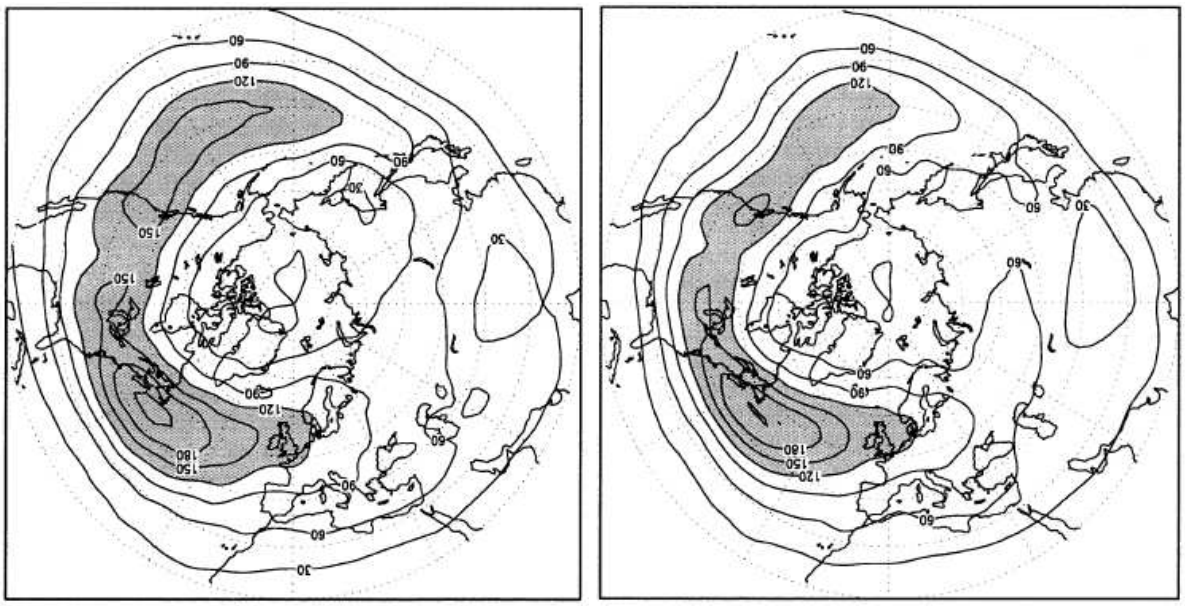

(a) El Niño (b) La Niña

Figure 2.13: *Bandpass variance of the meridional velocity taken at the 300 hPa level. (a) shows the bandpass variance field for nine El Niño years. (b) is the same as (a) only for nine La Niña years. The figures are retrieved from Chang and Orlanski (2002)*

ern tropical Pacific and has has far-reaching influences such as SST anomalies in the northern Pacific and anomalies in the large-scale planetary flow, stationary waves and mid-latitude storm tracks. Figure 2.13(a) and Figure 2.13(b) from Chang and Orlanski (2002) show the storm tracks represented by the bandpass filtered meridional velocity variance field for nine El Niño years and nine La Niña years, respectively. Changes are particularly pronounced in the Pacific storm track where the storm track shifts downstream and equatorward during El Niño years. The exact mechanisms controlling the ENSO phenomena remain to be fully understood (Lau, 1997).

Other modes of variability (e.g the annular modes) are also known to coincide with changes in the storm tracks. The annular modes (the Arctic and Antarctic Oscillation) are atmospheric modes of variability in the geopotential height field in which high-latitudes are characterized by negative anomalies and mid-latitudes are characterized by positive anomalies (Holton, 2004). Annular modes are associated with anomalies in the momentum fluxes caused by zonally asymmetric features such as stationary waves and baroclinic waves, which in turn maintain anomalies in the zonally symmetric mean flow. McCabe et al. (2001) found a pronounced change in cyclone frequency to be coincident with a regime shift in the Arctic Oscillation. Yin (2005) found that the northward shift of the storm tracks was coincident with a shift towards a high-index state of the Arctic and Antarctic Oscillation.

2.4.3 Long-term trends

Observational studies using e.g. reanalysis products are vital to gaining knowledge of long-term atmospheric trends. A plentiful number of studies cited in the IPCC Fourth Assessment Report (Trenberth et al., 2007) have investigated changes in storm tracks in reanalysis [3] data sets (e.g. Gulev et al. (2001), McCabe et al. (2001), Wang et al. (2006)).

Gulev et al. (2001) investigated cyclone variability in the Northern Hemisphere winter season using a feature point identification and subsequent tracking routine on the 6 h SLP field from the NCEP/NCAR reanalysis dataset. They found increasing cyclone intensities in the western North-Atlantic and Pacific, an increase in the cyclone frequency over the Arctic and western Pacific, but a decrease over the Gulf Stream and subpolar Pacific.

McCabe et al. (2001) studies cyclone frequency and intensity trends in the SLP field NCEP/NCAR reanalysis using feature point identification by the nearest neighbor approach. They found a decrease in cyclone frequency at mid-latitudes[4], an increase in cyclone frequency at high-latitudes[5] and an increase in cyclone intensity in both regions.

Wang et al. (2006) conducted a study on extratropical cyclone activity using the 6 h SLP field from both the NCEP/NCAR reanalysis and ERA40, using feature point identification and feature point tracking. An increasing trend in cyclone activity[6] was found over the high-latitude North Atlantic and mid-latitude Pacific and a decreasing trend was found over the mid-latitude North-Atlantic. Wang et al. (2006) estimate that the mean position of the North-Atlantic storm track has shifted northward by 181 km during the time period of the study.

2.4.4 Climate scenario studies

As seen above, reanalysis studies indicate trends in various storm track properties during the last half of the 20th century. According to Yin (2005), taking the step from observing these trends to attributing them to increased atmospheric levels of greenhouse gases cannot be done without further investigations of the atmospheric response to increased levels of greenhouse gases. It is therefore of interest to simulate the effect of increased greenhouse gases to the storm tracks and compare the results to the observed changes (Yin, 2005).

Yin (2005) used an ensemble of 15 general circulation models (GCMs) (a so-called super ensemble (Kalnay, 2007)) to assess the response in the storm tracks and the atmospheric baroclinicity to increased greenhouse gas forcing. Among his findings where a poleward and upward shift in the zonally averaged bandpass filtered eddy kinetic energy flux in both winter (DJF) and summer season June, July and August (JJA) and in both hemispheres. As can be seen from the upper two figures in Figure 2.14 the shift in the storm track is associated with a poleward and upward

[3] For more information about reanalysis datasets, consult section 3.2

[4] Mid-latitude being defined as the region between 30°N and 60°N

[5] High-latitude being defined as the region poleward of 60°N

[6] Cyclone activity is defined as the cyclone count multiplied by their mean intensity and is computed once for every season. (Wang et al., 2006)

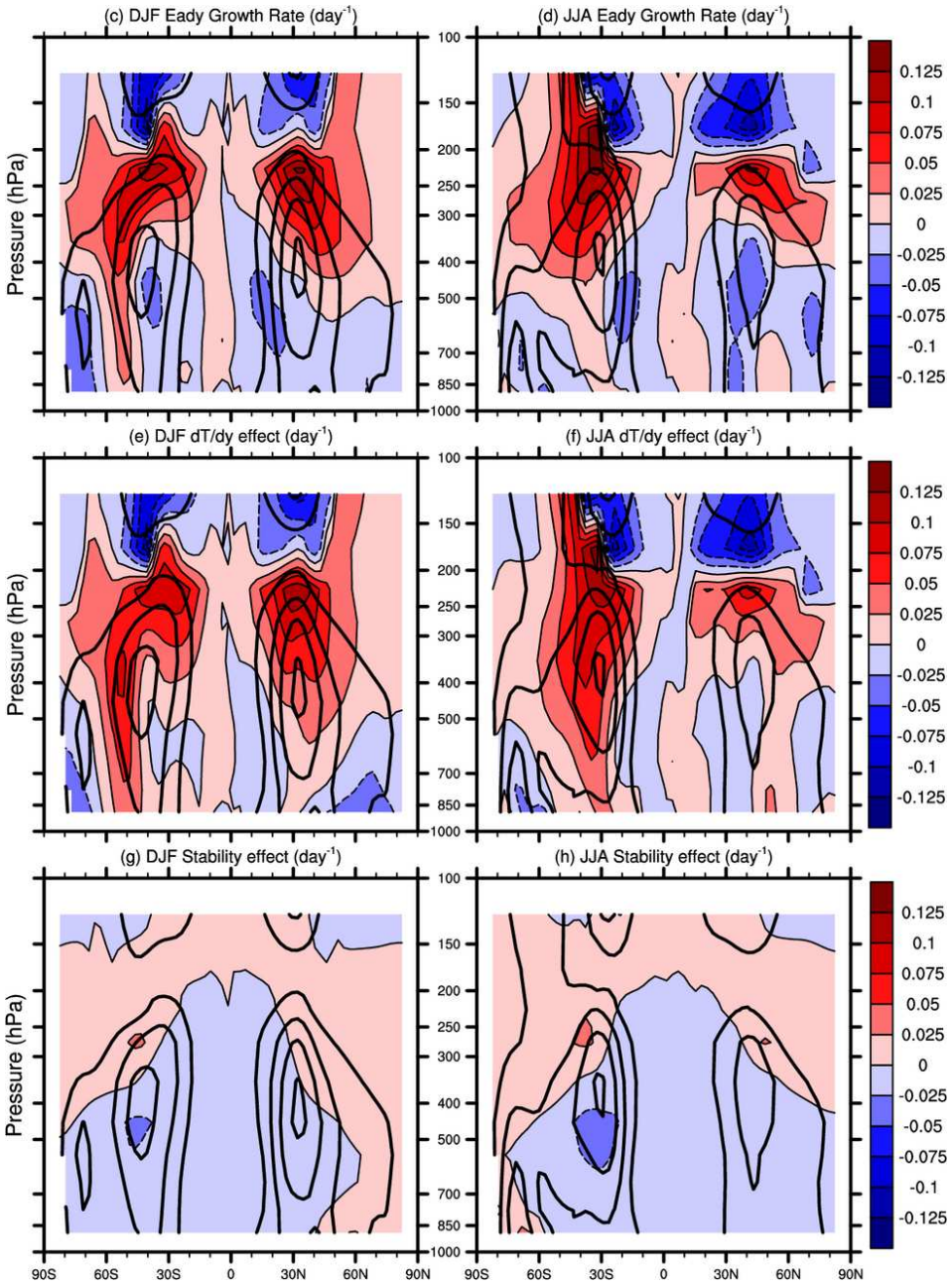

Figure 2.14: *Left column show DJF. Right column show JJA. Black contours represent the Eady parameter from the controle run without increased greenhouse gases, and contour interval is 0.2/day. Filled color contours represent the difference between the scenario runs (with greenhouse gases in accordance with the IPCC climate scenario A1B) and the control run, contour interval being given by the color bar in terms of day^{-1}. Top figures: difference in the full Eady parameter. Middle figures: difference in the contribution to the Eady parameter from the meridional temperature gradient. Bottom figures: difference in the contribution to the Eady parameter from the Brunt-Väisälä frequency. Figure is from Yin (2005).*

shift in the Eady parameter in both seasons and hemispheres. The Eady parameter used in Yin (2005) is given in Table 2.1 on page 16. The middle two figures in Figure 2.14 show the contribution to the Eady parameter from the meridional temperature gradient and the bottom two figures show the contribution from the Brunt-Väisälä frequency. It is clear from these figures that *the changes to the zonally averaged Eady parameter are caused by changes is the zonally averaged temperature gradient rather than the zonally averaged Brunt-Väisälä frequency*. Yin (2005) found the tropical atmosphere to experience warming maxima at high-levels, increasing tropopause height. Another warming maxima was found at high-latitude surface levels which Yin (2005) attribute to reduction of the sea ice. Thus the meridional temperature gradient was found to increase at high-levels in both hemispheres and seasons. The low-level temperature gradient was reduced in Northern Hemisphere winter and increased in Southern Hemisphere winter. Yin (2005) attribute the reduction in the Northern Hemisphere winter temperature gradient at surface level to a reduction in the sea ice cover. Changes to the surface temperature gradient during summer was small in both Hemispheres.

Orsolini and Sorteberg (2009) applied a Lagrangian feature point tracking method utilizing the $\zeta_{850\,\mathrm{hPa}}$ field in the Bergen Climate Model, investigating changes in summer (JJA) cyclones due to increased greenhouse gases. Among their findings were a reduction of total cyclone count, in terms of track density, in the Northern Hemisphere, but an increase in the number of cyclones traveling into the Arctic[7]. Cyclone mean intensity was found to decrease over midlatitudes and increase over the Arctic (Orsolini and Sorteberg, 2009).

[7] Orsolini and Sorteberg (2009) defines entering the Arctic as crossing the 75°N latitude circle

2.5 SST anomalies

SST anomalies can influence the atmosphere through anomalous fluxes of sensible and latent heat. If the SST anomaly can create vertical motion and vortex tube stretching, it can affect the vorticity field and excite the stationary Rossby waves. (Holton, 2004)

For low-frequency variability, the time derivative in the quasi-geostrophic temperature equation may be neglected leaving:

$$\vec{v}_g \bullet \nabla T - \left(\frac{\sigma p}{R}\right)\omega = \frac{J}{c_p}$$

where $\vec{v}_g$ is the horizontal geostrophic velocity vector, T is the temperature, σ is the static stability parameter, R is the ideal gas constant for dry air, ω is the vertical velocity in pressure coordinates, J is diabatic heating and c_p is the heat capacity under constant pressure.

The quasi-geostrophic temperature equation clearly shows that a diabatic heat source can be balanced in one of two ways: either by horizontal temperature advection by the geostrophic wind or by vertical motion and adiabatic cooling. Which process ends up dominating depends on the static stability of the atmosphere. In the tropics where the static stability is low, diabatic warming is compensated by vertical advection and adiabatic cooling. This allows for the SST anomaly signal to penetrate far into the atmosphere and cause

anomalies in the stationary wave pattern. Rising air in the atmospheric column cause upper level divergence which creates an upper level vorticity anomaly. In the presence of westerly flow, this vorticity anomaly can lead to stationary Rossby waves. At higher latitudes where static stability is generally large, horizontal temperature advection dominates over adiabatic cooling and the signal does not penetrate far into the atmosphere. It is therefore less likely that extratropical SST anomalies will cause a response in the stationary wave pattern compared to tropical SST anomalies. (Holton, 2004)

A well known example of SST anomalies coinciding with anomalies in the atmospheric circulation is the El Niño Southern Oscillation phenomena. One of the many effects of El Niño is increased SSTs in the western Pacific. The SST anomalies characteristic of El Niño typically have cycles of several years (Lau, 1997).

Chapter 3

Data

This chapter presents a short description of the model and reanalysis data used in this project. Both the model data and the reanalysis data is taken from the 10 year period 1. December 1980 - 28. February 1990 using the Northern Hemisphere winter months (DJF) only.

3.1 The CAM3 model

To perform simulations in this project, the NCAR CAM3 has been applied. CAM3 is a three-dimensional global AGCM which may be run as a stand-alone model or, alternatively, as the atmospheric component of the Community Climate System Model (CCSM) (Collins et al., 2006). The CCSM is a coupled climate model in which CAM3 is integrated together with the Community Land Model (CLM), the Community Sea Ice Model and the Parallel Ocean Program (Collins et al., 2006).

Why choose CAM and not CCSM in this study? The CCSM is suitable when one wishes to study the *interactions* of the atmosphere, ocean, sea ice and land surface. CAM3 on the other hand, is suited for looking into the responses of atmospheric circulation and state to a particular forcing such as increased SSTs or increased concentrations of greenhouse gases (Collins et al., 2006). As the ocean model in the CCSM is in dynamic equilibrium with the remaining components of the model, it would not be possible to force the ocean with a SST anomaly within a specific domain. As the aim of this project was to investigate the response of the storm track structure to various SST anomaly within various oceanic domains, CAM3 is an appropriate choice.

In this project, CAM3 was run as a stand-alone model. As default, CAM3 was integrated with the CLM which simulates energy exchanges over land, a thermodynamic sea ice model and a data ocean model (DOM). The model was run with both T85 and T42 spectral truncation and 26 vertical layers. The data ocean model was applied with default climatological data containing 12 monthly time samples. CAM3 was run with an Eulerian dynamical core, with the time step adjusting to satisfy the Courant-Friedrichs-Levy condition. SST and sea ice coverage[1] were read into the model from a boundary dataset containing 12 monthly samples for each grid point. The fluxes between the ice and the atmosphere were computed by the thermodynamic sea ice model.

[1] In this case the sea ice thickness was assumed to be 2 m in the Northern Hemisphere and 0.5 m in the Southern Hemisphere (Collins et al., 2006)

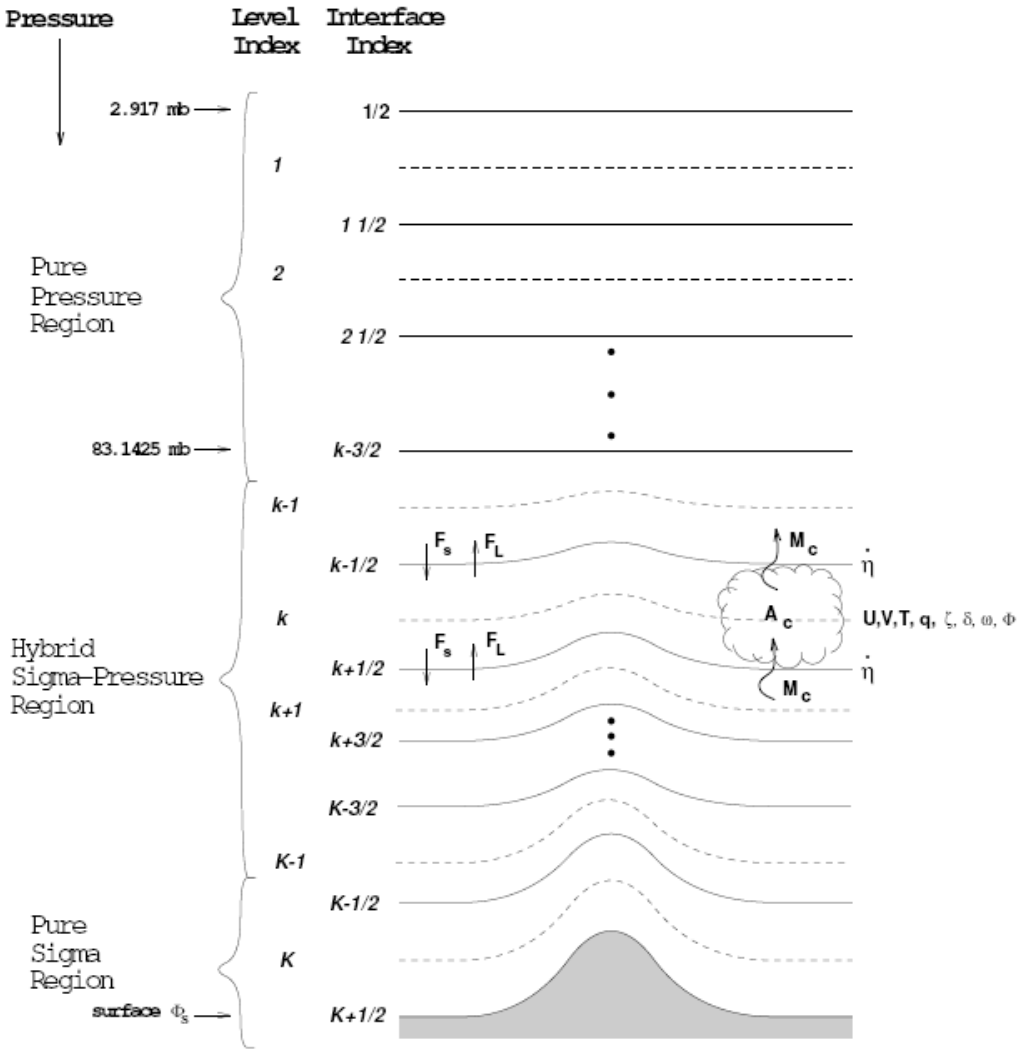

Figure 3.1: Hybrid vertical coordinate

Figure 3.1: *Illustrative description of the hybrid sigma-pressure vertical coordinate system used in the CAM3 model. Figure is from MaCaa et al. (2004).*

The CAM3 model uses hybrid sigma-pressure coordinates in the vertical. As shown in Figure 3.1, the CAM3 model uses sigma coordinates near surface, hybrid sigma-pressure coordinates at intermediate levels and pressure coordinates at high levels.

Pressure at grid point (i, j, k), where i is the zonal counter, j is the meridional counter and k is the vertical counter, at a given time is given by:

$$P(i, j, k) = A(k)P_0 + B(k)P_s(i, j) \qquad (3.1)$$

where A and B are vectors of constants, P_0 is a reference pressure taken to be 1000 hPa and P_s is the surface pressure.

The runs

A total of 13 runs were performed using the CAM3 model in total, including the control runs with T42 and T85 resolution. T42 resolution yields 128 grid points in the zonal direction and 64 grid points in the meridional direction, which corresponds to approximately $2.8^\circ \times 2.8^\circ$. T84 resolution yields 256 grid points in the zonal direction and 128 grid points in the meridional direction, which is corresponds to approximately $1.3^\circ \times 1.4^\circ$. The changes made from the control run in the remaining 11 modified runs were made in the SST and sea ice coverage fields, given in the initial condition dataset file `sst_HadOIBl_bc_64x128_clim_c020411.nc`. The SST and sea ice coverage fields in this file include 12 monthly samples, and changes to either field were made for all months. *Notice that all the modified runs were performed using T42 resolution.*

All modifications to the initial condition dataset were made using the R environment developed by R Development Core Team (2008) and the R-package `NCDF` (Pierce, 2006). Both the R environment and the `NCDF` package are freely available from `http://www.R-project.org`.

Modifications to the SST field were done by adding a scalar (such as 2 K or 8 K) to the existing SST field within a specified domain. The domain was defined in the meridional direction by ϕ_{start} and ϕ_{stop}, the former being the latitude at which the domain starts and the latter being the latitude at which the domain stops. The same goes for the zonal direction. At the domain boundaries a linear relaxation was applied when the boundary was located over the ocean to prevent abrupt changes in the SST field. To make sure that the temperature field was not changed over land, the CAM3 land fraction field available from `cami_000-09-01_64x128_L26_c030918.nc` was used to check that the land fraction at each grid point was sufficiently small to assure that the grid point was over ocean. SSTs were not changed in the presence of sea ice using the sea ice coverage field in a similar way as the land fraction field. For further details about how the SST field or the sea ice fraction field was modified, consult the source code of the

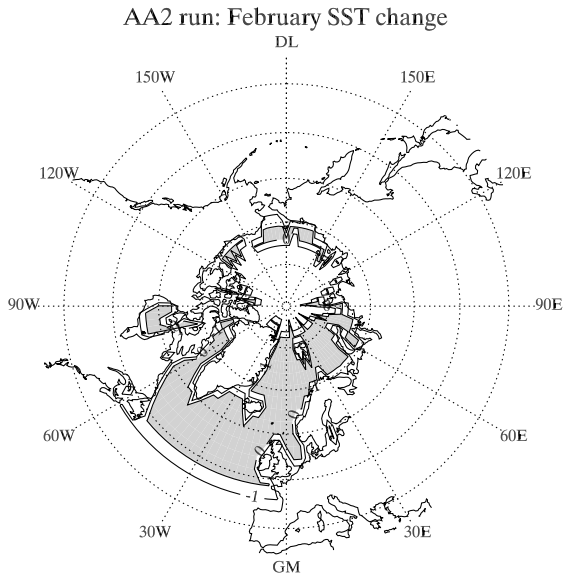

Figure 3.2: *The SST anomaly field from the AA2 run. The figure shows the February SST anomaly field corresponding changes are made for December and February, though small differences will arise because the sea ice coverage changes from month to month.*

Table 3.1: *This table yields a complete overview of all the modified runs that have been carried out in connection to this project and the changes made to both the SST field and the sea ice coverage field. The following abbreviations are used: A = Arctic, AA = north-Atlantic to Arctic, TML = Tropics to Mid-Latitudes, TA = Tropics to Arctic, NH = Northern Hemisphere, Lon = longitude, Lat = latitude. Lon region and lat region refers to the domains where the SSTs were increased.*

Run	SST anomaly	Lon region	Lat region	No sea ice NH
No ice	0 K	–	–	✓
A2	2 K	0 – 360°E	60 – 90°N	
A2 no ice	2 K	0 – 360°E	60 – 90°N	✓
A8	8 K	0 – 360°E	60 – 90°N	
A8 no ice	8 K	0 – 360°E	60 – 90°N	✓
AA2	2 K	270 – 30°E 0 – 360°E	45 – 65°N 66 – 90°N	
AA8	8 K	270 – 30°E 0 – 360°E	45 – 65°N 66 – 90°N	
AA8 no ice	8 K	270 – 30°E 0 – 360°E	45 – 65°N 66 – 90°N	✓
TML2	2 K	290 – 20°E *	45 – 34°S 33°S – 45°N	
TA2	2 K	290 – 20°E * 0 – 360°E	45 – 34°S 33°S – 65°N 66 – 90°N	
TA2 NH	2 K	0 – 360°E	45°S – 90°N	

** The longitudinal domain can be summarized to follow the American coastline in the west and the African and European coastline in the east.*

`change_sst` function in Appendix C or the `change_ice` function in Appendix D.

As previously mentioned, a total of 13 runs were performed using the CAM3 model including the control run with both high (T85) and low (T42) resolution in the horizontal. The modifications made to the runs consist of two things: changing the SSTs and changing the sea ice coverage. The modified runs include:

No ice run: Sea ice was removed from the entire Northern Hemisphere, no changes were made to the SSTs.

A2 run: SSTs were increased by 2 K in the Arctic with the Arctic being defined as the region north of 60°N.

A2 no ice run: same as A2 run, but with sea ice removed from all seasons in the Northern Hemisphere.

A8 run: same as A2, but SSTs were increased by 8 K.

A8 no ice run: same as A8 run, but with sea ice removed from all seasons in the Northern Hemisphere.

AA2 run: SSTs were increased by 2 K

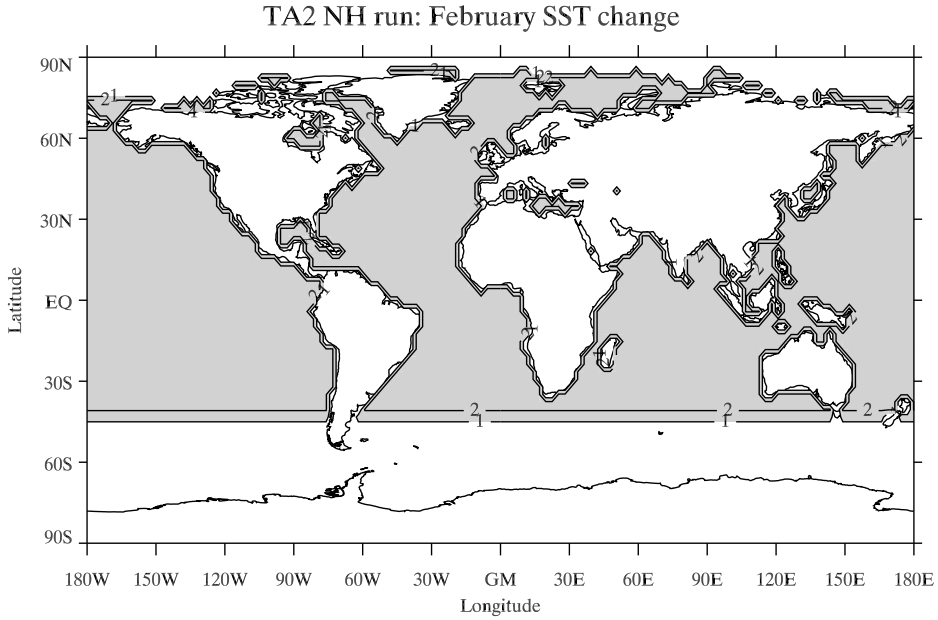

(a)

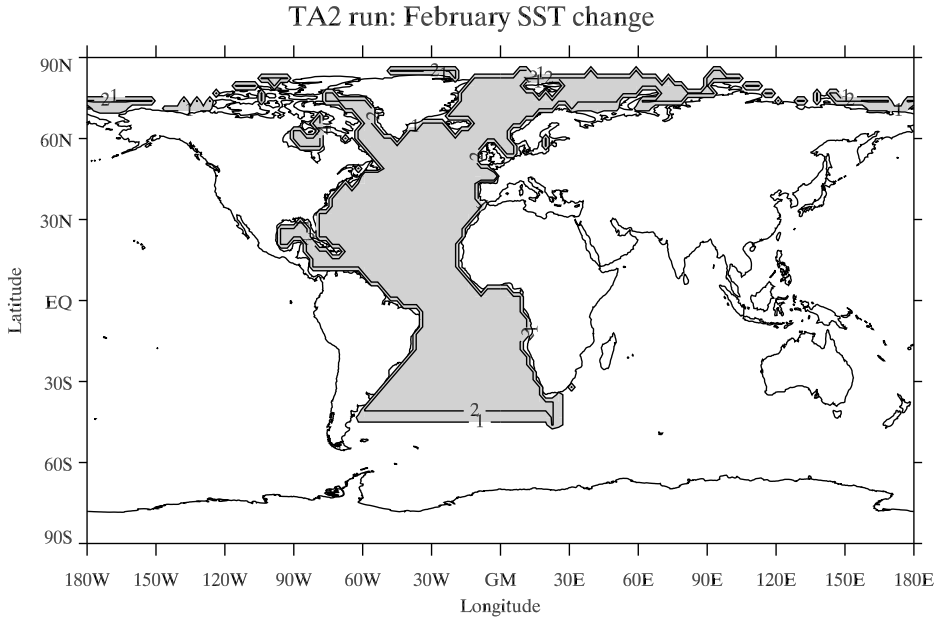

(b)

Figure 3.3: *(a) and (b) show the February SST anomaly field from the TA2 NH run and the TA2 run. Otherwise as in Figure 3.2*

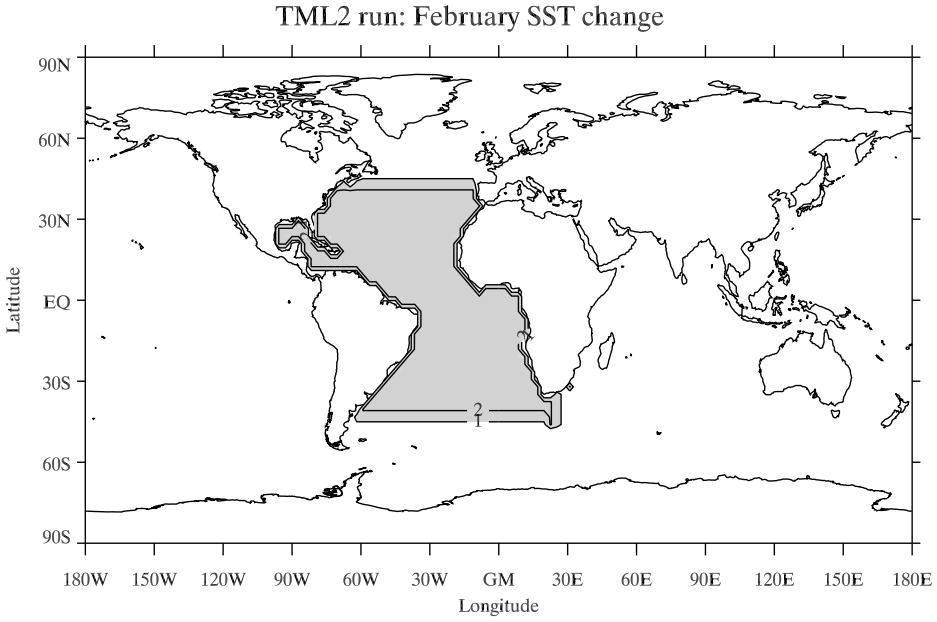

Figure 3.4: *The SST anomaly field from the TML2 run. Otherwise as in Figure 3.2*

in the Arctic everywhere north of 65°N and the North-Atlantic from 60°N down to 45°N.

AA8 run: same as AA2 run, but SSTs were increased by 8 K.

AA8 no ice run: same as AA8, but with sea ice removed from all seasons in the Northern Hemisphere.

TML2 run: SSTs were increased by 2 K in the Atlantic from 45°S to 45°N.

TA2 run: SSTs were increased y 2 K in the Arctic and Atlantic from 60°N all the way down to 45°S.

TA2 NH run: SSTs were increased by 2 K everywhere north of 45°S.

A more schematic overview of the modified runs is given in Table 3.1. The SST changes made in the TA2 NH, TA2, TML2 and AA2 runs are shown in Figure 3.3(a), Figure 3.3(b), Figure 3.4, and Figure 3.2, respectively. Notice that the gray area, representing the domain of SST change, does not extent all the way to the north pole because the SSTs were not changed in the presence of sea ice.

Results from the TA2 NH, TA2, TML2, AA2 and no ice run will be presented in section 5, the other runs will not be discussed any further.

3.2 NCEP/NCAR reanalysis

When studying the past climate using operational analysis, biases caused by sudden changes in the forecast models (such as resolution and parameterization) and data assimilation methods may be encountered. To avoid false trends created by technical

progress it is desirable to utilize analysis data made by one single model and one single data assimilation system. The NCEP/NCAR reanalysis 1 is one such data set. As indicated by its name, reanalysis data sets are made a posteriori. Reanalysises also differ from normal operational analysis in that observations of the state of the atmosphere are available for certain grid points at certain times throughout the entire time period. Using reanalysis data one avoids false trends caused by the model and data assimilation, but false trends due to inhomogeneities in the availability, quality and type of observations to a certain extent remain in the reanalysis product. Still, reanalysis products are considered the best possible estimate of the past state of the atmosphere.

The reanalysis data used in this project is from the NCEP/NCAR reanalysis 1 (from now on the 1 will be dropped for brevity). The NCEP/NCAR reanalysis was made in cooperation between the NCEP and NCAR. It is a global analysis including a variety of atmospheric fields such as sea level pressure, geopotential height at several pressure levels, air temperature, winds, and many more. Observations used in the data assimilation include among others observations from land surface, ships, rawinsondes, aircraft, satellites etc. It is run using the NCEP global spectral model implemented operationally at NCEP on the 11th of January 1995. The GCM runs with a T68 resolution in the horizontal and 28 vertical layers and the data is assimilated into the method using the 3D-VAR method. The reanalysis product is available for the time period 1948 - present. Both GCM and data assimilation are “frozen” throughout the time period of the reanalysis data. For more information about the NCEP/NCAR reanalysis, consult Kalnay et al. (1996).

NCEP/NCAR Reanalysis data was provided by the National Ocean & Atmosphere Administration/Outstanding Accomplishments in Research/Earth System Research Laboratory/Physical Sciences Division, Boulder, Colorado, USA, from their web site at `http://www.cdc.noaa.gov/`

Chapter 4

Methods

Storm tracks are generally investigated from either an Eulerian or a Lagrangian perspective. The most common Eulerian methods include bandpass filtering and feature point identification. Lagrangian methods involve finding the trajectory of each individual cyclone through feature point tracking methods.

In the following the three most common methods applied in storm track studies will be briefly discussed followed by short reviews of the methods applied in this project: bandpass filtering using the intrinsic IDL function `DIGITAL_FILTER` (ITT Visual Information Solutions, 2007) and feature point identification using a calculus-based cyclone identification (CCI) method. Both methods applied in this project investigate the storm tracks from an Eulerian perspective.

The bandpass filter method involves applying a bandpass filter to an atmospheric field in order to retain fluctuations within a given frequency range. As will be described in section 4.1 below, a bandpass filter acts to attenuate all frequencies outside a given frequency domain. Studies have shown that when retaining fluctuations with periods between about 2.5 and 6 days, the resulting field is dominated by developing baroclinic waves (Blackmon (1976), Blackmon et al. (1977)).

The bandpass filter method can be applied to any atmospheric field at any level, but some fields have proven to be more fruitful than others. Popular fields are among others sea level pressure, geopotential height, meridional velocity, meridional heat transport, and zonal momentum flux (e.g. Blackmon (1976), Blackmon et al. (1977), Hoskins and Hodges (2002), Chang and Orlanski (2002)).

When using this method it is important to realize that although the bandpass filtered fields are dominated by baroclinic waves (Blackmon (1976), Blackmon et al. (1977)) they are not caused by baroclinic waves alone. Other features fluctuating on similar timescales will contribute to the field.

A clear advantage of using bandpass filters is the fact that the method is less computationally demanding than e.g. feature point identification or feature point tracking. Also, it can easily be carried out at any altitude yielding a three-dimensional picture of the storm tracks Chang and Orlanski (2002).

Disadvantages of this approach are mainly not having the opportunity to study aspects

of the individual storms such as lifetimes, velocities, deepening rates and preferred regions of cyclogenesis and cyclosis (Gulev et al. (2001), Hoskins and Hodges (2002)).

The feature point identification method involves locating low-pressure centers (feature points) and counting them. A typical simple method is the "nearest neighbor approach" in which the sea level pressure field in each grid point is compared to the sea level pressure field in a given number of surrounding grid points (typically four or eight), demanding for the pressure difference to be larger than some threshold value. Other restrictions can also be imposed (e.g. Gulev et al. (2001)). The CCI method presented in section 4.2 represents a more sophisticated way of locating feature points.

Feature point identification methods are generally more computationally demanding than the bandpass filtering. They are traditionally carried out on the sea level pressure field or geopotential height field, and more recently on the relative vorticity field (Hoskins and Hodges, 2002). Like bandpass filtering, feature point identification yields no information about lifetimes, traveling velocities, deepening rates nor preferred regions of cyclogenesis or cyclosis. Unlike bandpass filtering, feature point identification yields data representing properties tied to the cyclones alone. Also, the results from feature point identification methods are also often biased towards slow or quasi-stationary features (like mature cyclones that have become quasi-stationary) when using sea level pressure field due to over-counting (Hoskins and Hodges, 2002). Another bias may be concealment of features in their initial development stage by the background flow and large-scale features such as the Icelandic low (Hoskins and Hodges, 2002). This can be avoided by using the vorticity field, or improved by filtering the sea level data before use. *Feature point identification methods yields information about where low pressure centers statistically are observed most frequently.*

The feature point tracking methods involves computing the trajectories of the individual cyclones, following the feature points from cyclogenesis to cyclosis. Such methods will typically consist of some feature point identification method followed by a routine that calculates the most probable trajectories of each cyclones (Hodges, 1994). Early methods would typically try to find trajectories by looking at a feature point at a specific time and searching for the feature point which is closest one time step later, imposing criterias of maximum allowed traveling velocity between time steps etc. This approach is biased due to the simple fact that the feature point which is closest at the next time step does not necessarily belong to the same trajectory. Thus it is useful to impose a smoothness requirement upon the trajectories. For more details about feature point tracking, consult Hodges (1994) and Hodges (1999).

The great thing about feature point tracking is that it yields the information you cannot get from bandpass filtering or feature point identification such as lifetimes, traveling velocities, deepening rates and regions of preferred cyclogenesis and cyclosis.

Notice that feature point identification is sometimes combined with feature point tracking to enable imposing requirements such as that the feature point must exist for

at least a given time period or/and have a traveling velocity greater than some threshold value (e.g. Hoskins and Hodges (2002), Paciorek et al. (2002), McCabe et al. (2001)). This improves the results with respect to the aforementioned biases tied to feature point identification.

4.1 The bandpass filter method

Temporal filtering of digital data series is commonly applied to reject or attenuate specific frequencies from the field. In atmospheric sciences the most common filters are the highpass, bandpass and lowpass filters described below.

The highpass filter rejects fluctuations with frequencies *lower* than the *high frequency cut-off value* f_H. As can be induced from its name, the highpass filters let fluctuations with high frequencies (higher than f_H) pass. In terms of period rather than frequency *the highpass filter retain fluctuations with periods shorter than some threshold value*.

The lowpass filter resembles the highpass filter, but rejects fluctuations with frequencies *higher* than the *low frequency cut-off value* f_L. *The lowpass filter retain fluctuations of periods larger than the threshold value*.

The bandpass filter is a combination of the highpass and lowpass filter. The bandpass filter rejects fluctuations with frequencies higher than f_H and lower than f_L, meaning that it keeps fluctuations within a frequency band determined by f_L and f_H.

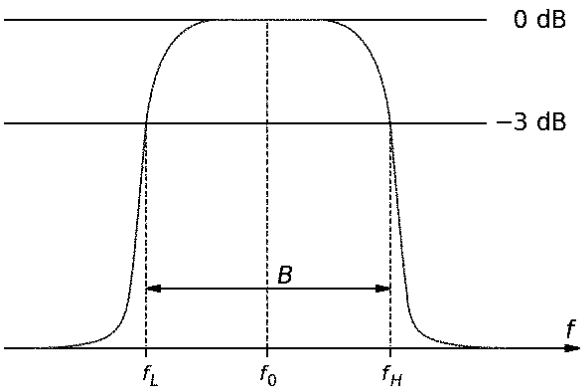

Figure 4.1: *Illustration of a hypothetical bandpass filter attenuation of output power signal as a function of frequency.* f_L *is the low frequency cut-off value,* f_H *is the high frequency cut-off value and* f_0 *is the center frequency. The stippled lines indicate the high and low cut-off frequencies and the solid line indicates the output power signal. At the cut-off frequencies, the output power signal is reduced compared to center frequency, but not completely rejected as it would have been in an ideal bandpass filter. The value* $f_H - f_L$ *is the filter bandwidth B. The figure is retrieved from* `http://en.wikipedia.org/wiki/Bandpass_filter` *May 31, 2009*

The effect and properties of the bandpass filter are illustrated in Figure 4.1.

Motivation

Atmospheric field such as the sea level pressure field or the geopotential height field fluctuate on many different timescales. The fluctuations in the fields are caused by various phenomena, for example the diurnal cycle, the passage of cyclones and anticyclones

and low-frequency features such as quasi-stationary mature cyclones and planetary waves. By applying filters to the fields it is possible isolate fluctuations with different timescales.

Blackmon (1976) studied the 500 hPa geopotential height field and discovered that the variance of the full un-filtered field closely resembled the variance of the low-pass filtered field. The lowpass filter used in Blackmon (1976) was made to retain fluctuations with periods longer than 10 days. Blackmon et al. (1977) found similar results for the sea level pressure field and the 300 hPa geopotential height field. The conclusion was made that the full atmospheric pressure and geopotential height fields are dominated by low frequency features with periods longer than 10 days. Higher frequency phenomena such as developing baroclinic waves are consequently concealed in the full atmospheric fields.

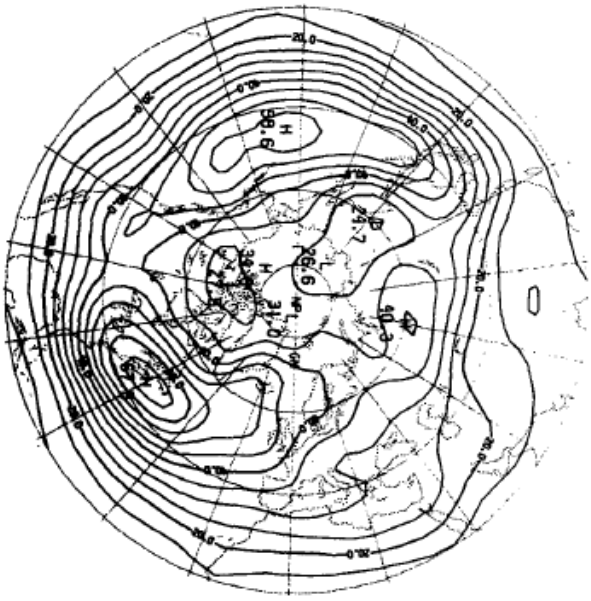

Figure 4.2: *500 hPa geopotential height bandpass RMS field from Blackmon (1976). Contour interval is 5 m. The bandpass filter retains fluctuations with periods between 2.5 and 6 days.*

Variations caused by growing baroclinic waves can by beautifully captured using a bandpass filter with suitable high and low cutoff values. The bandpass filter in Blackmon (1976) and Blackmon et al. (1977) retained fluctuations with periods between 2.5 and 6 days. Figure 4.2 shows the 500 hPa geopotential height bandpass Root-Mean-Square (RMS) field from Blackmon (1976). The figure clearly demonstrates two regions of particularly large RMS values, one in the Pacific and one in the North Atlantic. The location of both regions fits remarkably well with areas of known high cyclone frequency.

Blackmon et al. (1977) extended the study of Blackmon (1976) to include several other atmospheric fields, including sea level pressure, 300 hPa geopotential height, 500 hPa wind field, and 850 hPa meridional heat transport. Bandpass maxima corresponding well to the areas of high cyclone occurrence were found in all respective fields, though the exact location and extent of the maxima vary somewhat in space from field to field. The bandpass geopotential height fields at 500 and 300 hPa were more zonal than the bandpass sea level pressure field (Blackmon et al., 1977).

IDLs `DIGITAL_FILTER`

The specific bandpass filter applied in this project was made using the intrinsic IDL `DIGITAL_FILTER` function described in ITT Visual Information Solutions (2007). The bandpass filter was constructed by using the `DIGITAL_FILTER` function to find

the filter coefficients and then convolving the filter coefficients with the time series of atmospheric data at each grid point.

The IDL DIGITAL_FILTER is a finite impulse response filter, in which the response to an impulse in the time domain of the filter decays and goes to zero after a finite amount of time. This is in contrast to infinite response filters. The filter is applied non-recursively by convolving its impulse response with the data (time series of atmospheric data at each grid point). A non-recursive filter uses the current and previous input data of the filter to compute the filtered output. This is in contrast to a recursive filter which also uses previous output data, that is, already filtered data.

Input parameters of the DIGITAL_FILTER function are the high- and low-frequency cut-off values, the filter order and the filter power. The filter order is the number of previous elements of the input data that are used when computing the output data in the convolution process. The filter power is the size of the Gibbs Phenomenon variations, which are the oscillations resulting from abrupt truncation of an infinite fast Fourier transform series. ITT Visual Information Solutions (2007) recommends the filter power to be set to 50 dB.

The DIGITAL_FILTER function was applied with a low frequency cut-off frequency equivalent to 2.5 days, and a high frequency cut-off equivalent to 6 days, filter order of 25 (experiments showed that doubling the filter order did not alter the results) and a filter power of 50 dB. The DIGITAL_FILTER function returns a vector with length corresponding to the filter order plus one. At each grid point the coefficients were convolved with the complete time series of the atmospheric field at that specific grid point. Now, what is convolution?

The convolution of two functions f and g is in a special kind of product between two functions. The general infinite convolution is defined as (Farlow, 1993):

$$(f * g)(x) = \frac{1}{\sqrt{2\pi}} \int_{-\infty}^{\infty} f(x - \xi) g(\xi) d\xi$$

In fact, the convolution of function f and g is the inverse Fourier transform of the product of Fourier transforms of f and g (an operation often needed when solving partial differential equations) (Farlow, 1993):

$$(f * g)(x) = \mathscr{F}^{-1} \{\mathscr{F}[f]\mathscr{F}[g]\}$$

The intrinsic IDL CONVOL function was applied to convolve the filter coefficients and the time series. The CONVOL function was used without scaling and is defined as follows (ITT Visual Information Solutions, 2007):

$$R_t = \begin{cases} \sum_{i=0}^{k-1} (A_{t+i-\frac{k}{2}} K_i) & \text{if } \frac{k}{2} \leq t \leq n - \frac{k}{2} - 1 \\ 0 & \text{otherwise} \end{cases}$$

where A is an n-element vector to be convolved (the time series), K is a k-element vector used to convolve the A vector (the coefficients found using the DIGITAL_FILTER function), t is time, i is a counter and $n > k$. $k/2$ is found by integer division.

4.2 Feature point identification by the CCI method

The cyclone statistics created using feature point identification differs from that created

using bandpass methods in several ways. As previously mentioned, feature point identification yields information about low-pressure centers and low-pressure centers only. Bandpass filters yields the part of a field associated with variations of specific periods. As long as cyclones are not the only atmospheric phenomena with periods corresponding to those retained by the bandpass filter, other phenomena, such as anticyclones, will also be captured in the bandpass filtered data. So even though the bandpass filtered fields in the appropriate frequency domain are dominated by the mid-latitude storm tracks, there is no preventing other phenomena such as anticyclones from being a part of the field.

Another thing is that feature point identification methods do not care if the low-pressure center identified belongs to a growing, mature or decaying cyclone. All low-pressure centers that are identified by the method, regardless of what kind of cyclone they belong to, will be a part of the results from a feature point identification method. Bandpass filters on the other hand only yield information about growing cyclones. Mature and decaying cyclones are often slow or even quasi-stationary with periods too long to be captured by the bandpass filter.

In this project, feature point identification was performed using the CCI method (Benestad, 2008) developed by Rasmus Benestad at the Norwegian Meteorological Institute. The method was presented in Benestad and Chen (2006). The method was written in the R environment, and is freely available from the the R project website: `http://cran.r-project.org`.

The use of other feature point identification methods will, doubtlessly, yield different results due to the differences in the algorithms and threshold values utilized by the various methods. Differences in temporal and spatial resolution of the input data will also affect the results.

For storm tracking and feature point identification it is not necessarily obvious which field is the most suited. By and large, there is a widespread use of the sea level pressure field and the vorticity field. Both having their advantages and disadvantages. CCI uses the sea level pressure filed to locate the low-pressure centers. Benestad and Chen (2006) argues that sea level pressure is well suited because of this field having the most complete observational records and is an observed quantity used in the data assimilation, unlike vorticity which is a model-derived quantity.

Compared to other methods, CCI is more sophisticated. In short, the CCI method estimates the meridional and zonal sea level pressure profiles in form of a truncated Fourier series. The coefficients are computed using linear multiple regressions. Having analytical expressions for the sea level pressure profiles in both horizontal directions, analytical expressions for the first-order and second-order derivatives are easily found (Benestad and Chen, 2006). Sea level pressure minima can then be found from zero-crossing points of the first-order derivatives where the second-derivatives are positive (negative indicates anti-cyclones) (Benestad and Chen, 2006). This is illustrated by Figure 4.3.

Below is a mathematical description of the CCI method following Benestad and Chen (2006).

Given a two-dimensional pressure field

$P(x, y)$ or $P(\theta, \phi)$ (where ϕ is latitude and θ is longitude), the attained Fourier approximations for $p(\theta)$ and $p(\phi)$ are:

$$\begin{aligned} p(\theta) &= p_0 + \sum_{i=1}^{N_\theta}[a_\theta(i)\cos(\omega_\theta(i)\theta) + \\ &\quad b_\theta(i)\sin(\omega_\theta(i)\theta)] \\ p(\phi) &= p_0 + \sum_{i=1}^{N_\phi}[a_\phi(i)\cos(\omega_\phi(i)\phi) + \\ &\quad b_\phi(i)\sin(\omega_\phi(i)\phi)] \end{aligned}$$

where

The number of harmonics N_θ and N_ϕ are the number of harmonics applied. According to Benestad and Chen (2006), choosing 10 harmonics gives accurate results, and increasing this number gives little improvement to the results.

Longitude and latitude θ and ϕ are discrete variables with length n and m, respectively, and a step size $\delta\theta = \theta_2 - \theta_1$ and $\delta\phi = \phi_2 - \phi_1$. The intervals are defined as $\Delta\theta = \theta_n - \theta_1$ and $\Delta\phi = \phi_m - \phi_1$.

Spatial scales are given by θ and $\omega_\theta(i) = \frac{2\pi i}{\Delta\theta}$ in the longitude direction and ϕ and $\omega_\phi(i) = \frac{2\pi i}{\Delta\phi}$ in the latitude direction.

Coefficients $a_\theta(i)$, $b_\theta(i)$, $a_\phi(i)$ and $b_\phi(i)$ are estimated through multiple linear regression. The approximations of the coefficient found by linear regression are denoted as $\hat{a}_\theta(i)$, $\hat{b}_\theta(i)$, $\hat{a}_\phi(i)$ and $\hat{b}_\phi(i)$

The constant p_0 is arbitrary, and may vary from profile to profile.

Form this, the best approximations to the first-order derivatives are given by:

$$\begin{aligned} \frac{d\hat{p}(\theta)}{d\theta} &= p_0 + \sum_{i=1}^{N_\theta}[-\hat{a}_\theta(i)\sin(\omega_\theta(i)\theta) + \\ &\quad \hat{b}_\theta(i)\cos(\omega_\theta(i)\theta)] \\ \frac{d\hat{p}(\phi)}{d\phi} &= p_0 + \sum_{i=1}^{N_\phi}[-\hat{a}_\phi(i)\sin(\omega_\phi(i)\phi) + \\ &\quad \hat{b}_\phi(i)\cos(\omega_\phi(i)\theta)] \end{aligned}$$

Second-derivatives are obviously found by differentiating these expressions again with respect to the index variables.

The first order meridional and zonal gradients are easily found as follows (similar for the second order gradients):

$$\begin{aligned} \frac{d\hat{p}(x)}{dx} &= \frac{1}{a\cos(\phi)}\frac{d\hat{p}(\theta)}{d\theta} \\ \frac{d\hat{p}(y)}{dx} &= \frac{1}{a}\frac{d\hat{p}(\phi)}{d\phi} \end{aligned}$$

Now, local pressure minima are identified when:

$$\begin{aligned} \frac{\partial\hat{p}(x)}{\partial x} = \frac{\partial\hat{p}(y)}{\partial y} &= 0 \text{ and} \\ \frac{\partial^2\hat{p}(x)}{\partial x^2} &> 0 \text{ and} \\ \frac{\partial^2\hat{p}(y)}{\partial y^2} &> 0 \end{aligned}$$

Secondary cyclones near deeper ones are removed.

Settings

In this project, the CCI method was used to identify cyclones on the Northern Hemisphere. The method was applied with 16

harmonics and was restricted to detecting 10 simultaneous cyclones. Investigations conducted in Benestad and Chen (2006) using both 25 and 10 harmonics showed that changing the number of harmonics does not significantly alter the results. The input data was interpolated to a $1^\circ \times 1^\circ$ grid.

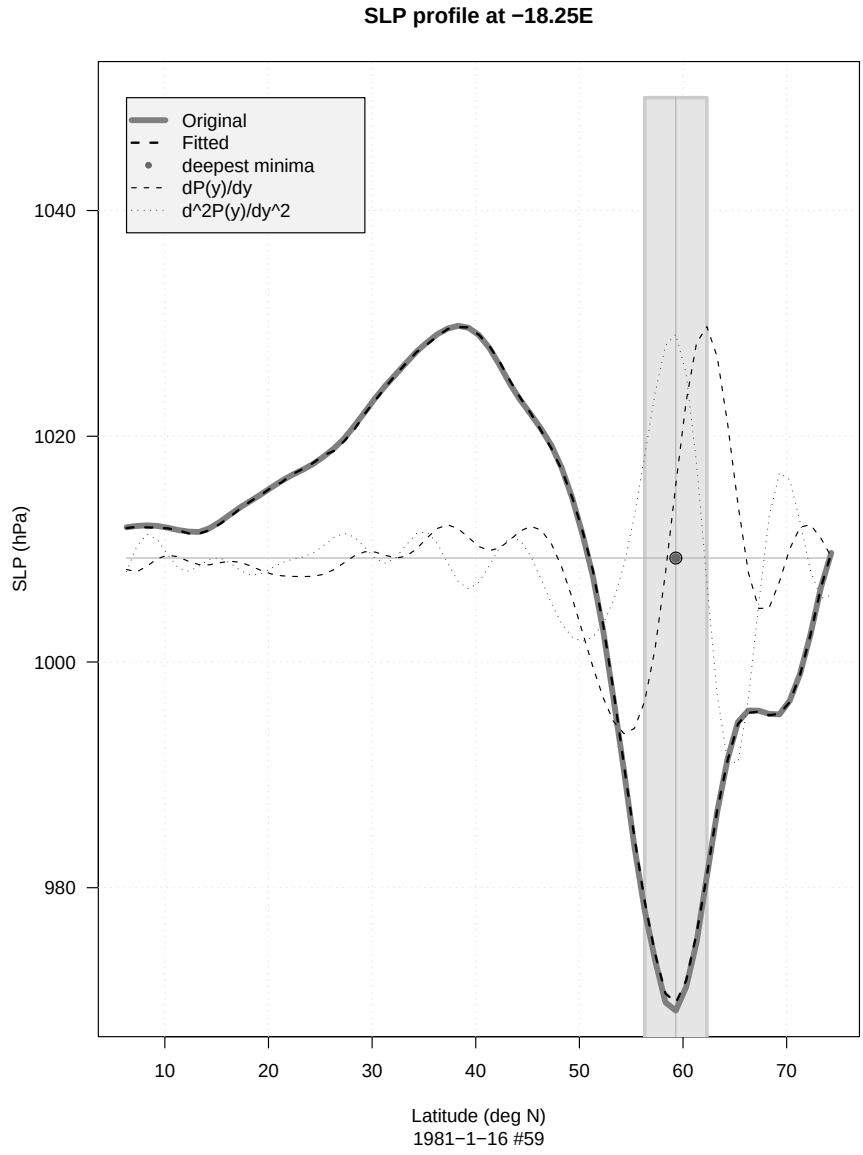

Figure 4.3: *Zonal sea level pressure profile showing the workings of the CCI. The thick grey line is the original sea level pressure filed from the input data. The thick dashed line which is more or less overlapping the thick grey line is the Fourier approximation. The thin dashed line is the first-order derivative, and the dotted line is the second-order derivative. The circle marks the cyclone center identified by CCI. Notice that the circle is at the zero-crossing point of the first-order derivative, and that the second-order derivative is positive as required by CCI. Notice also that the thin horizontal line illustrates 0 hPa as the thin dashed line and the stippled line have been moved up relative to the ordinate axes.*

Chapter 5

Results

This chapter presents results from this project. Unless stated otherwise, all results in this chapter are taken from the time period 1. November 1980 – 31. March 1990 using the Northern Hemisphere winter season (DJF).

All NCEP/NCAR reanalysis data presented in this chapter was taken from the same time period as the CAM3 data, and subjected to the exact same methods (e.g. bandpass filtering and feature point identification) and plotting routines as the CAM3 data. The only difference being in the cases where the CAM3 data has been interpolated from the CAM3 hybrid sigma-pressure coordinates to pressure coordinates. The NCEP/NCAR reanalysis data is in pressure coordinates by default, and therefore not in need of interpolation.

In sections of this chapter where results from both the high-resolution (T85) and low-resolution (T42) control run are presented, the low-resolution control run will be referred to as the T42 control run, and the high-resolution control run will be referred to as the T85 control run. In sections which only presents or discusses results from the T42 control run, "T42" will be omitted for brevity.

In the first section, fields from the T42 control run are presented and compared to the corresponding fields from the NCEP/NCAR reanalysis. The comparison will show that CAM3 accurately simulates the structure and magnitudes of the fields presented, and is well suited for performing sensitivity studies.

The second section presents results from the T85 control run and compares them to the T42 control run and the NCEP/NCAR reanalysis. The comparison will show that some aspects of the fields improve, while others actually worsen, and that the improvements are not sufficient to warrant performing all the modified CAM3 runs with T85 resolution in the horizontal taking the dramatically increased run-time into account.

The third section presents results from the TA2 NH run where the SSTs have been increased by 2 K in all oceanic grid points north of 45°S. The results will show that the North-Atlantic storm track shifts northeast in response to the SST anomaly, that no clear latitudinal shift in seen in the Pacific storm track, and that the zonally averaged temperature and zonally averaged Eady parameter fields are remarkably similar to results obtained with fully coupled climate models, in which C02 has been increased Yin (2005)

The fourth section investigates the effects of latitudinal and longitudinal variations in the SST anomaly domain, presenting results from the TA2, TML2 and AA2 runs. Results will show that changing the SST anomaly domain in the latitudinal or longitudinal direction yields strong changes in all fields investigated, and that low latitude heating is the most important forcing in these runs.

The fifth section investigates results from the no ice run where the ice cover has been removed from the entire Northern Hemisphere. Results will show that removing the ice cover yields storm track changes of similar magnitudes as high-latitude heating.

The sixth and final section presents results from the CCI method in terms of cyclone count from the T42 control run, the NCEP/NCAR reanalysis, the T85 control run and the TA2 NH run. Results will show that cyclone counting is a less robust measure for investigating storm track changes than bandpass variance.

5.1 The control run

Abstract

In this section the bandpass SLP, bandpass $Z_{500\,\mathrm{hPa}}$, u, Eady parameter, zonally averaged u and zonally averaged Eady parameter fields are presented and compared to NCEP/NCAR reanalysis data.

Bandpass SLP: *Maxima are found in both storm track regions. NCEP/NCAR reanalysis and control run are similar in the storm track regions. Bandpass variance is too high over high topography, and the North-Atlantic storm track is somewhat too zonal.*

Bandpass $Z_{500\,\mathrm{hPa}}$: *Storm track maxima are well simulated, but the North-Atlantic maximum is somewhat too zonal. Topographically related problems are reduced compared to bandpass SLP.*

u: *Maxima correspond to the position of the bandpass maxima, though shifted somewhat upstream and equatorward. Control run compares well to the NCEP/NCAR reanalysis. u is consistent in structure and magnitude with zonally averaged u.*

Eady parameter: *Maxima are found in the storm track entrance regions. Structure is similar to u, and the control run relates to the NCEP/NCAR reanalysis as in u. Results are consistent with Hoskins and Valdes (1990). Eady parameter structure and magnitude is consistent with the zonally averaged Eady parameter. Zonal average maxima are located in regions of strong vertical wind shear, and the general structure is very similar to results from Yin (2005).*

The main conclusion from this section is that CAM3 yields fields which closely resemble the NCEP/NCAR reanalysis. Therefore, CAM3 can be used to perform meaningful sensitivity studies.

In this section, results from the control run[1] are presented and compared to the NCEP/NCAR reanalysis data for the purpose of assessing whether CAM3 captures the structure and magnitude of the fields well enough to be suited for sensitivity studies.

In the following, the bandpass filtered SLP field, the bandpass filtered $Z_{500\,\mathrm{hPa}}$ field, the u field, the Eady parameter field, the zonally averaged u field and the zonally averaged Eady parameter field will be investigated and compared to NCEP/NCAR reanalysis data.

Bandpass SLP

In this section and the four following section in this chapter, the storm tracks will be investigated using the bandpass method. Recall from section 4.1 that bandpass filtering involves rejecting all frequencies *not* within a specified range of frequencies, and that according to Blackmon et al. (1977), choosing this range of frequencies to be equivalent to all time periods between 2.5 and 6 days yields a field which is *dominated* by growing baroclinic waves. Blackmon et al. (1977) applied such a bandpass filter to the SLP field, and found the North-Atlantic and Pacific storm tracks to be represented by two large maxima in the bandpass variance field.

Apart from the fact that the SLP field is a suitable choice for bandpass filtering, additional motivation is the desire to compare results from the bandpass filter method to results from the CCI method later in this chapter, a process with goes much smoother

[1] Notice that the control run presented in this section is the T42 control run

when the two methods have been applied to the same field.

The SLP field is not the only field suited for bandpass filtering in storm track studies. The $Z_{500\,\mathrm{hPa}}$ field, the meridional velocity field, the zonal momentum flux field and the meridional heat flux field have all been proven suited for bandpass filtering (Blackmon (1976), Blackmon et al. (1977)). In this project, the SLP field and the $Z_{500\,\mathrm{hPa}}$ field have been subjected to bandpass filtering. Both fields are presented in this section.

The 6 h SLP field was bandpass filtered using the intrinsic IDL function `DIGITAL_FILTER` as described in section 4.1 on page 41. The filter was made to retain fluctuations in the field with periods between 2.5 and 6 days, following Blackmon (1976) and Blackmon et al. (1977).

Figure 5.1(a) shows the bandpass filtered instantaneous 6 h SLP standard deviation field[2] from the control run. Bandpass variance is therefore expected to be high at mid- and high-latitudes, and low in the subtropics and tropics. This is exactly what is shown in Figure 5.1(a). Bandpass variance increases northward from the tropics and reaches its largest values in a circumpolar belt between 40 and 70°N. Bandpass variance is generally higher over the oceans than over continents except from in the near proximity of high topography.

The bandpass SLP field shows three large maxima; a Pacific maximum starting northeast of Japan, a North-American maximum over and downstream from the Rockies, a North-Atlantic maximum starting at east coast of North-America. *The two oceanic maxima correspond to the Pacific and North-Atlantic storm tracks, respectively*, confirming the results of Blackmon et al. (1977). Notice that, in terms of bandpass SLP, the North-Atlantic maximum is stronger than the Pacific maximum. Also, notice that the North-Atlantic maximum is partly located over the North-American east coast while the Pacific storm track maximum is located entirely over the ocean.

Additional bandpass variance is seen near topographic features in the proximity of Greenland and over Central Asia, the latter being associated with the Himalayas.

The large North-American maximum associated with the Rockies requires further attention. A similar feature was discovered by Blackmon et al. (1977), but not as pronounced as in Figure 5.1(a). Blackmon et al. (1977) attributed this feature to shallow systems, as upper-level fields did not reveal enhanced variability in this region. A corresponding relationship will be revealed later in this section.

The *strength* of the maximum associated with the Rockies may be associated with a bias in the CAM3 model. Hurrell et al. (2006) compared the mean DJF SLP field from the CAM3 model to corresponding data from ERA40. They found the difference fields to be very noisy with absurd magnitudes in regions of high topography. This indicates that extrapolation of the SLP field in such areas is an issue with the CAM3 model. Nevertheless, bandpass variance over regions of high topography is not the focus of this project. The greatest concern is the ability of the CAM3 model to properly simulate the storm track related maxima in the North-Atlantic and Pacific oceans.

[2] From now on referred to as the "bandpass SLP field" for brevity

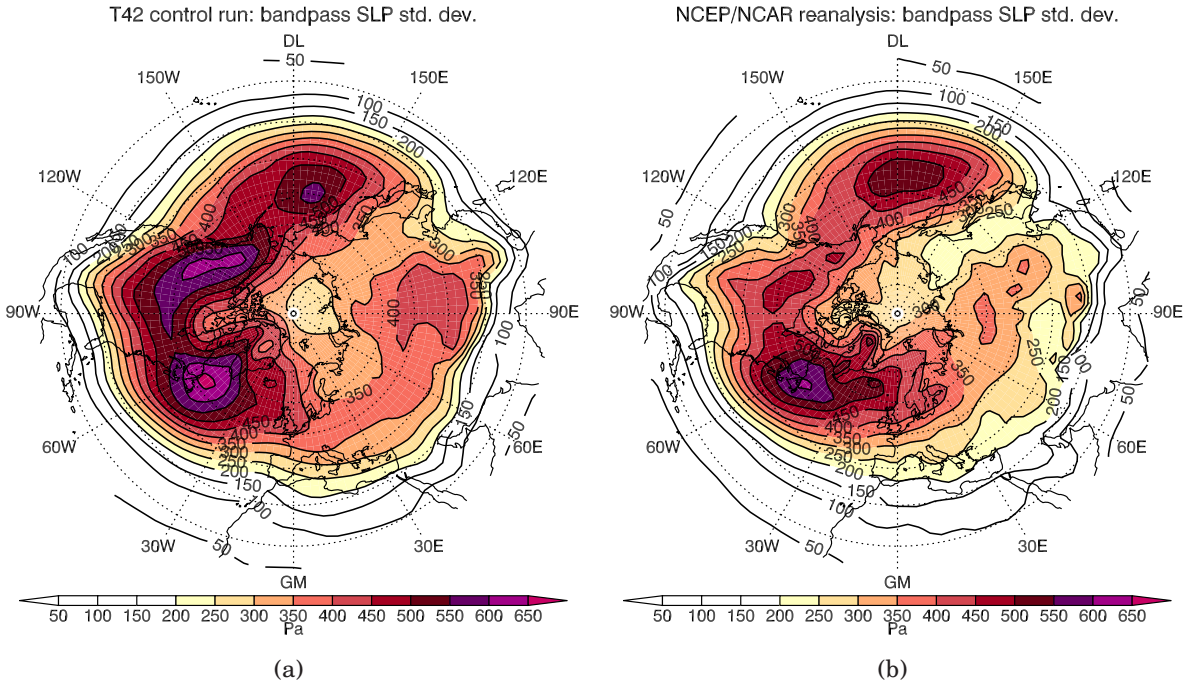

Figure 5.1: *Standard deviation of the bandpass filtered SLP field from the control run (Figure (a)) and the NCEP/NCAR reanalysis (figure (b)).*

Figure 5.1(b) shows the bandpass SLP field from the NCEP/NCAR reanalysis. The structure is very similar to the control run in Figure 5.1(a). Bandpass variance increase when moving from the tropics towards the pole and peaks in a circumpolar band between 30 and 70°N, and is relatively low over the Arctic Ocean. As in the control run, large maxima are found in the Pacific and the North-Atlantic corresponding to the Pacific and North-Atlantic storm tracks, the North-Atlantic maximum being stronger than the Pacific maximum. Enhanced variability is also found downstream from the Rockies, over Greenland and to some degree over Central Asia. Variability is low over western Asia upstream from the Pacific maximum and over the Arctic Ocean in both figures. A "trough" feature is found over Mexico and western Asia in both figures. It is clear that CAM3 captures all features present in the NCEP/NCAR reanalysis.

The largest differences between the control run and the NCEP/NCAR reanalysis are in areas of high topography and in the North-Atlantic storm track exit region. The NCEP/NCAR reanalysis display reduced bandpass variance over and downstream from the Rockies and the Himalayas. The strong reduction of the intensity of these feature, particularly associated with the Rockies, contributes to the suspicion that the CAM3 model fails to properly extrapolate the SLP field over high topography. Over Greenland it seems that the relatively large values of bandpass variance located west of Greenland in the control run have shifted east and are located more di-

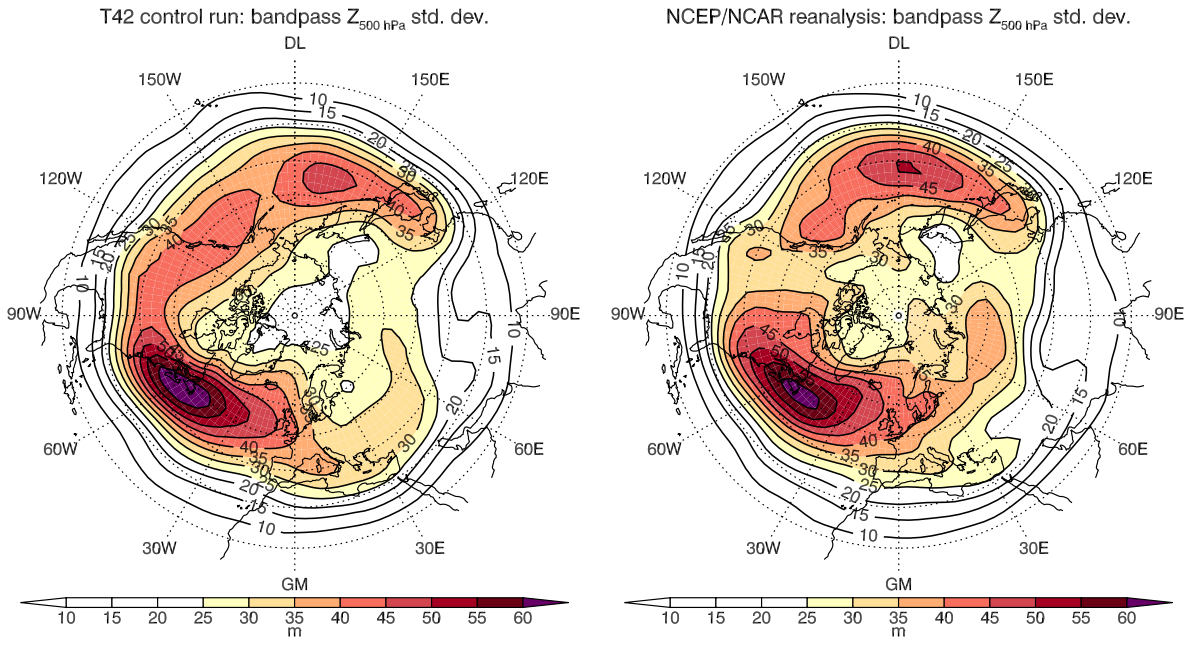

Figure 5.2: *Bandpass filtered $Z_{500\,\mathrm{hPa}}$ standard deviation field from the control run and the NCEP/NCAR reanalysis.*

rectly over Greenland in the NCEP/NCAR reanalysis.

The North-Atlantic storm track has a more pronounced northward tilt in the NCEP/NCAR reanalysis as bandpass variance is higher in the traditional storm track exit region (Norwegian and Barents Sea). The structure of the North-Atlantic storm track in the NCEP/NCAR reanalysis is consistent with the traditional perception that the North Atlantic storm track stretches from the east coast of North-America and all the way to the Barents Sea. The North-Atlantic storm track is known for being more tilted in the northward direction than its Pacific counterpart.

The fact that the northward tilt is not apparent in the control run is consistent with the results of Hurrell et al. (2006). Hurrell et al. (2006) investigated the bandpass statistics from CAM3 in terms of eddy kinetic energy ($\sqrt{u'^2 + v'^2}$) and transient momentum flux ($u'v'$) filtered to retain synoptic variations fluctuations with variations between 2 and 8 days. Findings from the eddy kinetic energy field were that the general features were well simulated, but with a general overestimation of variability and a more zonally elongated structure in the North-Atlantic during DJF compared to ERA40. Hurrell et al. (2006) commented that the missing tilt of the North-Atlantic storm track is consistent with an observed bias in the mean zonally averaged wind field. According to Black and Dole (2000), the North-Atlantic storm track is commonly seen to be too zonal in GCM studies, a result which may be related to a bias in the upper-level barotropic deformation

field which is believed to be instrumental to storm track termination (e.g. Chang and Orlanski (2002)).

Apart from over regions of high topography and in the North-Atlantic storm track exit regions, differences between the control and the NCEP/NCAR reanalysis are small. The North-Atlantic maximum experience some reduced variability in the region south of Greenland (13% at most) and the Pacific storm track region (5 % at most).

Bandpass $Z_{500\,\mathrm{hPa}}$

As stated in relation to the bandpass SLP field, the $Z_{500\,\mathrm{hPa}}$ field is also suited for bandpass filtering (Blackmon, 1976). There are several reasons for investigating an upper level field in addition to a surface-level field, the most important being that, as pointed out by among other Chang and Orlanski (2002), one of the great advantages of bandpass filtering compared to other methods is the fact that it can be carried out at all altitudes, yielding a three-dimensional picture of the storm tracks. Also, cyclones are not only surface features, but have a characteristic vertical structure which allows baroclinic wave activity to dominate the geopotential height field at all levels from the surface to about 200 hPa. According to Blackmon et al. (1977), the distribution of bandpass filtered SLP, $Z_{500\,\mathrm{hPa}}$ and $Z_{300\,\mathrm{hPa}}$ are qualitatively similar with bandpass variance increasing by a factor 1.7 from sea level to 300 hPa.

In the previous discussion of the bandpass SLP field, the CAM3 SLP field yielded a relatively large bandpass variance maxima in regions of high topography. Though, as noted by Blackmon et al. (1977), enhanced variability is observed to be associated with high topography and is therefore expected in such areas, comparison with the NCEP/NCAR reanalysis revealed that bandpass variance is in fact too large in these regions in CAM3. Hurrell et al. (2006) also found the SLP field to be biased in regions of high topography and attributed this to the extrapolation process. *It is therefore likely that an upper-level field, such as the $Z_{500\,\mathrm{hPa}}$, will not be exposed to the same biased extrapolation as the SLP field, and thus be a better choice.* In the following the bandpass filtered $Z_{500\,\mathrm{hPa}}$ field will be presented and compared to NCEP/NCAR reanalysis data.

The instantaneous 6 h $Z_{500\,\mathrm{hPa}}$ field[3] from the control run and the 6 h $Z_{500\,\mathrm{hPa}}$ field from the NCEP/NCAR reanalysis were bandpass filtered using the same procedure as before.

Figure 5.2(a) shows the bandpass $Z_{500\,\mathrm{hPa}}$ field from the control run. The structure is very similar to the bandpass SLP field, with bandpass variability increasing northward from the tropics, reaching maximum values between 40 and 60°N and subsequently decreasing towards the pole. *Bandpass variability is large in a circumpolar band with maxima off the east coasts of North-America and Asia corresponding to the North-Atlantic and Pacific storm tracks.* Once again, the North-Atlantic maximum is stronger than the Pacific maximum.

Compared to the bandpass SLP field, the bandpass $Z_{500\,\mathrm{hPa}}$ field is more zonally symmetric, narrower in the meridional direction and less noisy. While the band-

[3] As with the SLP field, "bandpass $Z_{500\,\mathrm{hPa}}$ field" refers to the bandpass filtered $Z_{500\,\mathrm{hPa}}$ standard deviation field for brevity

pass SLP field displayed topography related variability over North-America, Asia and Greenland, the bandpass $Z_{500\,\mathrm{hPa}}$ field does not display bandpass variance maxima in these regions. Some enhanced variability is evident over North-America, but the North-Atlantic or Pacific maxima are much stronger. There is little evidence of enhanced variability associated with the Himalayas or Greenland. *The reduction in the intensity of these features is probably due to two things: as noted by Blackmon et al. (1977), the features causing these maxima in the bandpass SLP field are shallow, and the $Z_{500\,\mathrm{hPa}}$ field is probably not exposed to the same extrapolation related problems as the SLP field*.

Figure 5.2(b) shows the bandpass $Z_{500\,\mathrm{hPa}}$ field from the NCEP/NCAR reanalysis. The structure is very similar to the control run in Figure 5.2(a). As seen when investigating the bandpass SLP fields, the Pacific maximum is actually stronger in the NCEP/NCAR reanalysis field than the SLP field. Bandpass variance in the North-Atlantic storm track entrance regions is reduced while bandpass variance has increased slightly in the Norwegian and Barents Seas, over Norway, Sweden, Finland and northeastern Russia. Again, the North-Atlantic maximum seems to be exhibiting a more pronounced northward tilt in NCEP/NCAR reanalysis compared to the control run.

The NCEP/NCAR reanalysis yields a reduction in bandpass variance over the Rockies indicating that CAM3 overestimates variability in this region. Still, it is not as pronounced as with the bandpass SLP field.

Thus, the bandpass $Z_{500\,\mathrm{hPa}}$ field captures the main features well and does not exhibit the same degree of topography related overestimation of bandpass variance as the bandpass SLP field. This is consistent with Hurrell et al. (2006)[4], as they found the $Z_{500\,\mathrm{hPa}}$ field to be well simulated in CAM3.

The $Z_{500\,\mathrm{hPa}}$ corresponds better to the NCEP/NCAR reanalysis than the SLP field. Because of this, the bandpass $Z_{500\,\mathrm{hPa}}$ can be argued to be more all over reliable, and perhaps a better choice for the purpose of bandpass filtering in the modified runs presented later in this chapter. It will still sometimes be of interest to investigate the responses in the bandpass SLP field for the purpose of comparing the bandpass filter method to the CCI method.

Mean u

Recall from section 2.2 that cyclones are closely tied to the westerlies and the westerlies are closely tied to the cyclones. The cyclones exist because the westerlies are baroclinically unstable, that is, small perturbations are able to grow feeding on the energy of the mean flow (Vallis, 2005). These small perturbations turn into cyclones. They preferential form in highly baroclinic regions, that is, sites of strong meridional temperature gradients, which by thermal balance is equivalent to strong vertical wind shear. Climatologically, cyclones act to reduce the baroclinicity of the mean flow by transporting heat and momentum in such a way as

[4] In particular, Hurrell et al. (2006) found the major troughs in the mean $Z_{500\,\mathrm{hPa}}$ field to be captured (e.g. off the east coast of Asia and North-America during NH winter) along with ridge features such as that over Russia, the west coast of North-America and the eastern Atlantic. Ridge features off the west coast of North-America and in the eastern Atlantic was on the other hand shifted westward and the Atlantic ridge was too weak.

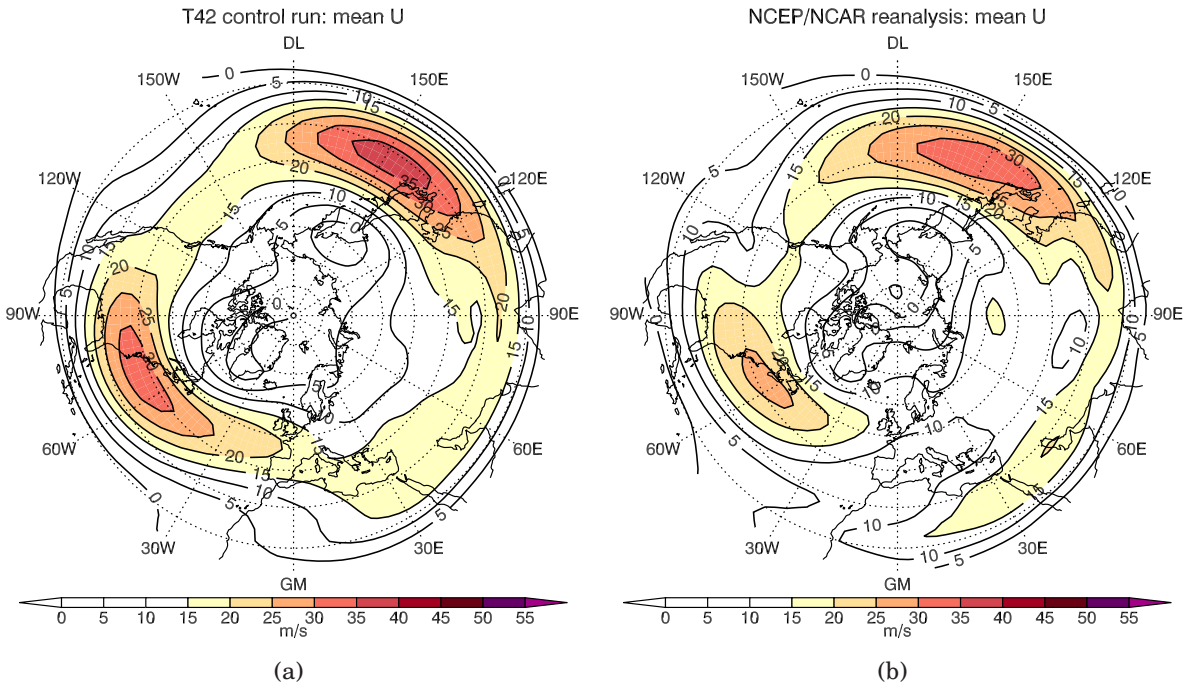

Figure 5.3: *(a) and (b) show u from the control run and the NCEP/NCAR reanalysis, respectively. In (b), the monthly averaged u from the control run was interpolated from the CAM3 hybrid sigma-pressure coordinate system to pressure coordinates. In both figures, u is plotted at the 500 hPa surface.*

to lower the atmospheric center of mass/ weaken the meridional temperature gradient.

A two-way relationship between the mean circulation and bandpass eddies was established by Branstator (1992) and Branstator (1995). Branstator (1992) showed that anomalies in the bandpass variance field, on the timescales between 1 and 7 days, act to maintain anomalies in the temporally averaged u field[5]. Three years later, Branstator (1995) showed that anomalies in u acts to maintain anomalies in the bandpass variance field. Thus, a two-way feedback effect is established between anomalies in the bandpass eddie field and u.

Because of this two-way feedback effect, it is of interest to investigate the changes in u that accompany the changes in the bandpass variance fields. In the following, the u field from the control run will be presented and compared to NCEP/NCAR reanalysis data.

The u fields were found using the monthly averaged u from the control run and the NCEP/NCAR reanalysis and averaging in time for the entire time period. The monthly averaged u field from the control run was interpolated from the CAM3 hybrid sigma-pressure coordinate system to pure pressure coordinates using the intrinsic IDL function `INTERPOL`. Subsequently

[5]From now on, "u" will refer to the temporally averaged u field for brevity

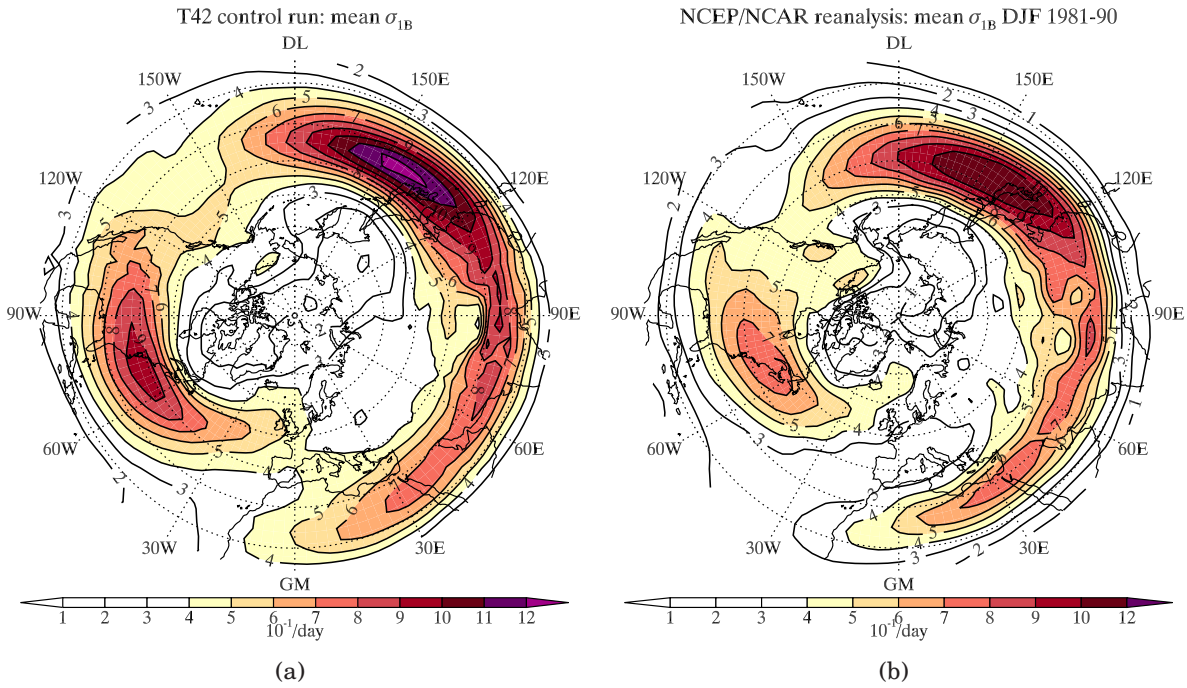

Figure 5.4: *(a) and (b) show the Eady parameter from the control run and the NCEP/NCAR reanalysis, respectively. The Eady parameter is computed using equation (2.6) with finite difference approximations taken between the 500 hPa and 700 hPa pressure levels. Both spatial derivatives are represented numerically by forward in space finite difference approximations.*

the u *was plotted at the 500 hPa surface* to facilitate comparison between the u and the bandpass $Z_{500\,\mathrm{hPa}}$ field and the Eady parameter later in this section.

Figure 5.3(a) shows u from the control run. Large values are found in a band around the North Pole similar to the structure of the bandpass $Z_{500\,\mathrm{hPa}}$ field in Figure 5.2(a). Again, maxima are located off the east coasts of North-America and Asia, but this time the Pacific maximum is stronger than the North-Atlantic maximum. This runs counter to what was seen with the bandpass SLP and $Z_{500\,\mathrm{hPa}}$ fields where the North-Atlantic maximum was stronger than the Pacific maximum. The band of high u values is narrower and maxima are more zonally elongated compared to the bandpass SLP and $Z_{500\,\mathrm{hPa}}$ fields. Also, the bandpass variance maxima are shifted slightly northward and downstream compared to the maxima in u.

The observation that maximum u and maximum bandpass variance are coincident in time and space, is consistent with the assumption that baroclinic growth is triggered in areas of large meridional temperature gradients and large vertical wind shear yielding upper-level maxima in u.

u from the NCEP/NCAR reanalysis data is shown in Figure 5.3(b). *The structure compares very well to the control run*. The North-Atlantic and Pacific maxima are located in approximately the same regions, both longitudinally and latitudinal, values

are relatively low in both storm track regions compared to the entrance regions, and a band of values exceeding 15 m/s is found over Asia.

Comparing the NCEP/NCAR reanalysis to the control run, values are somewhat smaller. In the North-Atlantic and Pacific maximum, values are about 5 m/s larger in the control run. The Pacific maximum is slightly more zonally elongated and extends further downstream. The starting point, in terms of the 25 m/s contour, is also shifted slightly downstream. Unlike the Pacific maximum, the North-Atlantic maximum is shorter in the zonal direction. There are also indications of a northward tilt in the storm track exit region, seen by investigation the 10 m/s contour, not evident in the control run. The control run does not yield a northward tilt in the storm track exit region, rather the structure is more zonal and values are too high over western Europe. This was also noted by Hurrell et al. (2006).

CAM3 manages to capture the structure and magnitudes of u compared to the reanalysis. Values are slightly too large and the North-Atlantic u maxima is too zonal, consistent with the bandpass SLP and bandpass $Z_{500\,\mathrm{hPa}}$ fields.

Eady parameter

Is is now established that bandpass variance maxima coincide in time and space with maxima in u. Maximum u were as expected found off the east coast of North-America and Asia where large meridional temperature gradients caused by the contrast between the cold continents and the warm western boundary currents yields strong vertical wind shear and strong upper level winds. It is now interesting to see how the Eady parameter, which is a measure of atmospheric baroclinicity presented in section 2.2.5, relates to these maxima and how it compares to NCEP/NCAR reanalysis data.

The Eady parameter as shown in this thesis was computed from equation (2.6) on page 16 using monthly averaged air temperature as T, and then averaged for the entire time period. The temperature field was interpolated from the hybrid sigma-pressure coordinates in CAM3 to pressure coordinates using the intrinsic IDL function `INTERPOL`. The Brunt-Väisälä frequency was computed using a forward in space finite difference approximation in the vertical where the geopotential height difference was approximated using equation (1.20) in Holton (2004):

$$d\phi = -RTd\ln p$$

Where ϕ is the geopotential, T is temperature, R is the gas constant of dry air and p is pressure.

The meridional temperature derivative was also represented by a forward in space finite difference approximation. Finally, the Eady parameter was plotted at the 500 hPa surface to avoid spurious maxima caused by interactions with the planetary boundary layer.

Figure 5.4(a) shows the Eady parameter from the control run. *The structure is remarkably similar to u.* This similarity is not surprising as the Eady parameter is proportional to the meridional temperature gradient and, by thermal wind balance, to the vertical wind shear. Large values are found in the storm track entrance regions slightly upstream from the maxima in the band-

pass SLP field (Figure 5.1(a)) and bandpass $Z_{500\,\mathrm{hPa}}$ field (Figure 5.2(a)), consistent with the findings of Hoskins and Valdes (1990). As the Eady parameter is a growth rate indicating regions of large potential baroclinic growth, it is logical for the baroclinic waves to reach their peak intensity downstream from regions where growth is initiated.

The North-Atlantic Eady parameter maximum starts off the west coast of North-America and increases in value towards the east coast where its reaches its peak value. Large values continues across the North-Atlantic with a weak northward tilt. The Pacific maximum starts over China and increases in magnitude until it reaches the east coast of Japan, subsequently it continues towards the middle of the Pacific. The Pacific maximum is more zonally symmetric than the northeastern Atlantic maximum. Also, the Pacific maximum is much stronger, a relationship which also shows up in the u field. *Judging from the Eady parameter alone, one would expect stronger baroclinic growth and stronger baroclinic wave activity in the Pacific than the North-Atlantic.* This runs counter to what is seen from the bandpass SLP and $Z_{500\,\mathrm{hPa}}$ fields. For some reason, *bandpass variance is largest in the storm track with the lowest Eady parameter values*. This is not an exceptional observation. Nakamura (1992) observed that while the atmospheric baroclinicity in the Pacific reaches its peak value during mid-winter, while the bandpass variance experience what is referred to as "the mid-winter minima" (see section 2.4.1 on page 24). The relationship between atmospheric baroclinicity and bandpass variance is not properly understood (Chang and Orlanski, 2002).

Another feature which stands out in Figure 5.4(a) is the large values found in a band stretching from North-Africa and over Asia all the way to the Pacific, but there is no corresponding maximum in the bandpass SLP, bandpass $Z_{500\,\mathrm{hPa}}$, or u fields. From this, conclude that *having large values in the Eady parameter is not enough to guarantee baroclinic growth*. It is likely that the large values over Africa and Asia do not result in baroclinic wave growth because of the lack of oceanic latent heat sources.

Figure 5.4(a) is qualitatively similar to the Eady parameter plot in Hoskins and Valdes (1990), displayed in Figure 2.9 on page 18. Notice that the domain is slightly different as Figure 2.9 includes all latitudes in the Northern Hemisphere, while Figure 5.4(a) excludes latitudes south of 15°N. Notice also that Figure 2.9 is taken at the 780 hPa surface, with regions likely to be in the planetary boundary layer blackened, while Figure 5.4(a) is taken at the 500 hPa surface. Figures are also made from different data.

Figure 5.4(b) shows the Eady parameter from the NCEP/NCAR reanalysis. Again, *the over all structure is very similar to the control run*. Large maxima are seen in the storm track entrance regions in the North-Atlantic and the Pacific, and relatively low values are seen in the exit regions. Also, the same band of relatively large values of the Eady parameter extends from northern Africa, over Asia and all the way to the Pacific maximum.

Again, the peak values in the NCEP/NCAR reanalysis maxima are not as high as in the control run, meaning that the CAM3 model slightly overestimates the strength of the Eady parameter in both storm track entrance regions. This effect is also seen

to some degree in the eastern Pacific upstream from the Rockies. The Pacific maximum stretches further downstream and the North-Atlantic maximum is shifted slightly downstream over the North-America continent in the NCEP/NCAR reanalysis compared to the control run. The North-Atlantic maximum also appears to exhibit a more pronounced northward tilt with enhanced values in the Norwegian Sea. This is consistent with what was seen when investigating the bandpass SLP, bandpass $Z_{500\,\mathrm{hPa}}$ and u fields, all indicating that the North-Atlantic storm track is too zonal.

The differences between the NCEP/NCAR reanalysis and the control run are very similar to the differences found with u.

Zonally averaged u

Now, having investigated the zonally averaged u and the zonally averaged Eady parameter fields in the xy-plane, it is interesting to see how these fields relate to the zonally averaged fields plotted as a function of latitude and pressure and to compare the control run fields to NCEP/NCAR reanalysis data. Zonally averaged u will be investigated first.

The zonally averaged u plots were made taking the zonal average of the monthly averaged u field for the entire time period. As before, the control run data was interpolated from the CAM3 hybrid pressure-sigma coordinate vertical coordinate to constant pressure surfaces using the intrinsic IDL function `INTERPOL`.

Figure 5.5(a) shows the zonally averaged u from the control run. A large maximum is found at 30 – 40°N at tropopause level

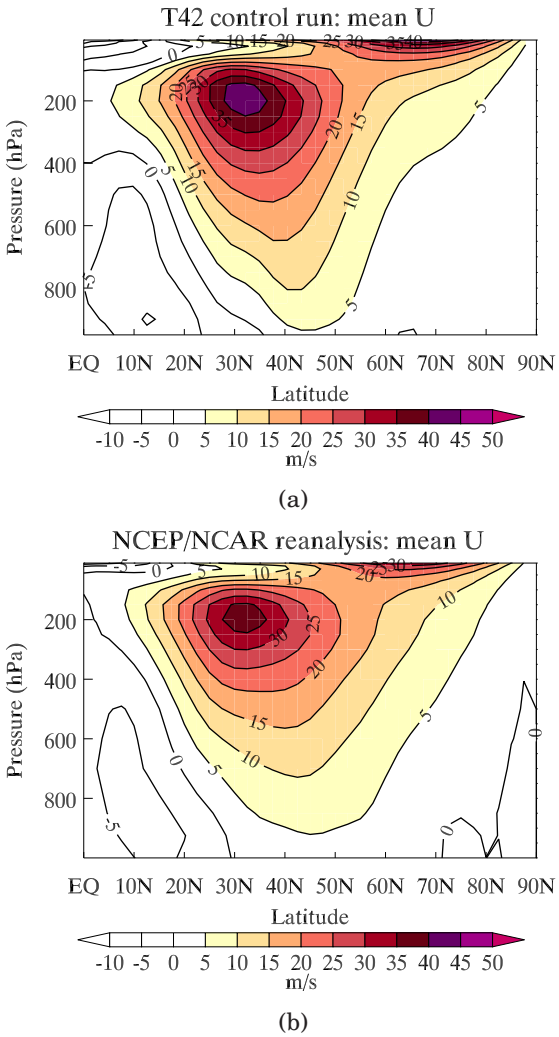

Figure 5.5: *(a) and (b) shows zonally averaged u from the control run and the NCEP/NCAR reanalysis, respectively. Notice that in the NCEP/NCAR reanalysis data, pressure coordinates is default so the NCEP/NCAR reanalysis data has not been interpolated in the plotting routine.*

(about 200 hPa), corresponding to the jet stream. *Notice the strong vertical wind shear below the maximum which must exist due to the meridional temperature gradient and the prevailing thermal wind balance which exists at the respective latitudes.*

Investigating the relationship between the zonally averaged u and u in Figure 5.3(a), it must be kept in mind that u is taken at the 500 hPa surface. At this level, peak values in the zonally averaged u field are between 15 and 20 m/s at 30 – 40°N. This is consistent with both position and strength of the u field maxima, taking smoothing resulting from taking the zonal average into account.

Another maximum is seen at the upper boundary between 45 and 80°N. This is probably caused by the stratospheric jet[6] which is westerly in the winter hemisphere and reaches its peak velocity at about 60 km altitude (corresponding to approximately 0.3 hPa) (Holton, 2004). The southern hemisphere has an easterly jet which can be spotted as a minimum at the upper boundary between the equator and 20°N. The vertical resolution in the stratosphere is too low to properly resolve these features.

Figure 5.5(b) shows zonally averaged u from the NCEP/NCAR reanalysis. Again, *the structure of the NCEP/NCAR reanalysis plot and the control run plot are very similar* with a strong maximum at about tropopause level at 30 – 40°N corresponding to the jet stream, evidence of a positive maximum at the upper boundary between 45 and 85°N, evidence of a negative maximum at the upper boundary between the equator and 20°N, and easterlies at low-levels between 5 and 20°N.

Similar to what was observed when comparing the u plots from the NCEP/NCAR reanalysis and the control run, zonally averaged u peak values are once again approximately 5 m/s weaker. This is consistent with Hurrell et al. (2006), as they found the zonally averaged westerlies in CAM3 to be slightly stronger than in ERA40 in the region between 35°N and 55°N, an effect which is seen by comparing Figure 5.5(a) and Figure 5.5(b).

By and large, small differences do exist, but the zonally averaged u in the control run and the NCEP/NCAR reanalysis are remarkably similar.

Zonally averaged Eady parameter

As with the u field, it is interesting to see how the Eady parameter field in the xy-plane relates to the zonally averaged Eady parameter plotted as a function of latitude and pressure. Also, the zonally averaged u field clearly picked out the regions of strong vertical wind shear. Comparing the zonally averaged u and the zonally averaged Eady parameter fields enables investigating whether maximum Eady parameter values are really located in regions of maximum vertical wind shear. As with the previous fields, the zonally averaged Eady parameter field will be compared to NCEP/NCAR reanalysis data, and the capability of CAM3 to accurately reproduce the field will be assessed.

Finally, the relative contributions to the Eady parameter from the meridional temperature gradient and the Brunt-Väisälä frequency in terms of $\sigma_{1B,N}$ and $\sigma_{1B,\,dT/dy}$, as defined equation (2.8) and equation (2.7) on page 17, will be investigated to see which quantity makes the greatest contribution to the structure and magnitude of the zonally averaged Eady parameter.

Like the Eady parameter in Figure 5.4(a) and Figure 5.4(b), the zonally averaged

[6] For reference, consult Figure 12.2 in Holton (2004)

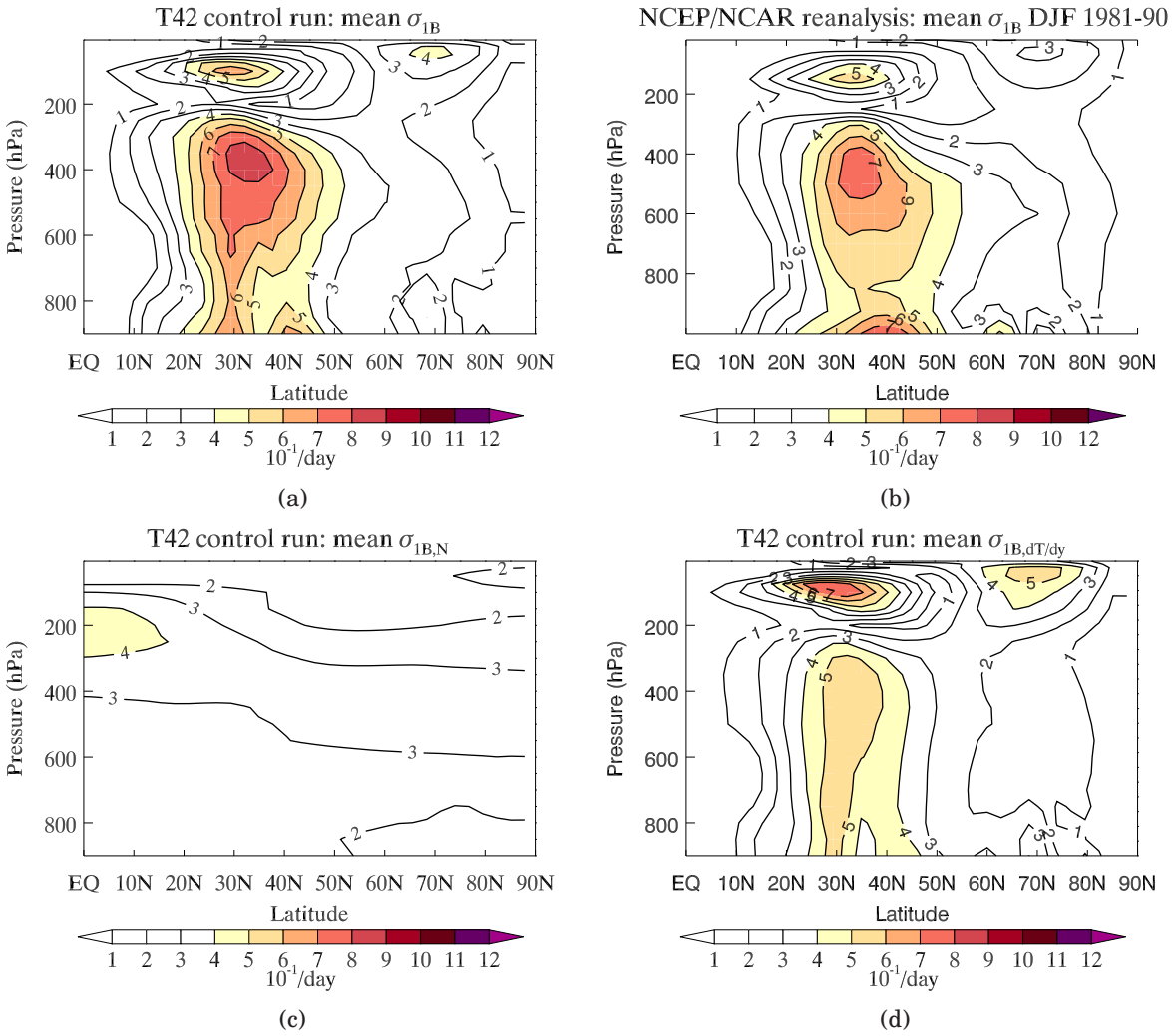

Figure 5.6: *(a) and (b) shows the zonally averaged Eady parameter from the control run and the NCEP/NCAR reanalysis defined in equation (2.6) on page 16. (c) shows the relative contribution to the Eady parameter from the Brunt-Väisälä frequency as defined in equation (2.8) on page 17. (d) shows the relative contribution to the Eady parameter from the meridional temperature gradient as defined in equation (2.7) on page 17. Otherwise as in Figure 5.4.*

Eady parameter was found from equation (2.6) on page 16 using the same approximations and fields. Once again, the control run data was interpolated from the CAM3 hybrid sigma-pressure coordinates to pressure coordinates using the intrinsic IDL function `INTERPOL`.

Figure 5.6(a) shows the zonally averaged Eady parameter from the control run. The main feature of this figure is the large maximum located between 30 and 40°N between the 400 and 300 hPa surfaces. Comparing this to the structure and magnitudes in Figure 5.4(a) and taking smoothing into account, values are both quantitatively and

qualitatively consistent.

Underneath the main maximum in the zonally averaged Eady parameter, values decrease with increasing pressure. Two weaker maxima are located at higher levels, the first one directly above the largest maximum at approximately 100 hPa. The second weak maximum close to the upper boundary at 70°N is associated with the stratospheric jet in Figure 5.5(a). Notice that atmospheric baroclinicity as measured by the zonally averaged Eady parameter is relatively large at low-levels where values generally decrease from 0.6/day at 30°N to 0 - .1/day at 80 – 90°N. Some caution should be taken with respect to the low-level values as there is probably interference with the planetary boundary layer.

Notice that *all maxima are located in regions of strong vertical shear*, consistent with equation (2.5) on page 16 which states that the Eady parameter is proportional to the strength of the meridional temperature gradient which by thermal wind balance corresponds to the strength of the vertical wind shear. Since the Eady parameter in equation (2.5) is proportional to the absolute value of the meridional temperature gradient, strong negative wind shear corresponds to positive values, which explains why the upper-level maximum at 100 hPa and 30°N is positive.

It is interesting to compare the full zonally averaged Eady parameter in Figure 5.6(a) to the findings of Yin (2005). The expression for the Eady parameter in this project and in Yin (2005) are the same, making them suitable for comparison (section 2.2.5 on page 15). The full Eady parameter from Yin (2005) is shown in black solid contours in the upper left figure in Figure 2.14 on page 28. Contour interval is 0.2/day, twice as large as in Figure 5.6(a). Consistent with this, Figure 2.14 reveals less fine structure. *The zonally averaged Eady parameter from the control run is quantitatively and qualitatively very similar to the corresponding field from Yin (2005).*

Figure 5.6(a) shows the zonally averaged Eady parameter from the NCEP/NCAR reanalysis. Notice that the large dominating maximum at 400 – 300 hPa and 30 - - 40°N in the control run is also present in the NCEP/NCAR reanalysis, only shifted slightly towards higher pressures. Also, maxima are about 0.1/day higher in the control run, consistent with findings in the zonally averaged u field. Over all, both the magnitude and location of this primary feature are consistent between the two figures. Other minor maxima seen in the control run are also present in the NCEP/NCAR reanalysis such as the upper-level maximum located directly above the main large maximum, and the smaller upper-level maximum associated with the stratospheric jet. Observe that the height levels are not identical as the control run extends down to 900 hPa while the NCEP/NCAR reanalysis extends all the way down to 1000 hPa. When taking this into account, low-level features are also very similar. *The zonally averaged Eady parameter from the control run relates very well to the NCEP/NCAR reanalysis.*

"Decomposition" of the Eady parameter

Section 2.2.5 on page 17 explains how the Eady parameter can be "decomposed" into two parts: one representing the contribution to the Eady parameter from the Brunt-Väisälä frequency, $\sigma_{1B,N}$, and another rep-

resenting the contribution from the meridional temperature gradient, $\sigma_{1B,\,dT/dy}$. The definitions of $\sigma_{1B,N}$ and $\sigma_{1B,\,dT/dy}$ are given in equation (2.8) and equation (2.7) on page 17. $N_{\text{reference}}$ was taken as the temporally, longitudinally, latitudinally and vertically averaged Brunt-Väisälä frequency field from the control run. Similarly, $|\frac{dT}{dy}|_{\text{reference}}$ was taken to be the temporally, longitudinally, latitudinally and vertically averaged meridional temperature gradient from the control run. These reference values were also applied to the modified runs to be presented in later sections. *It is important to understand that the Eady parameter is not strictly speaking decomposed as the full Eady parameter cannot be found as a superposition of $\sigma_{1B,\,dT/dy}$ and $\sigma_{1B,N}$, hence the quotation marks*.

Figure 5.6(c) and Figure 5.6(d) show the zonally averaged $\sigma_{1B,N}$ and $\sigma_{1B,\,dT/dy}$ from the control run, respectively. Comparing these two figures to the full Eady parameter in Figure 5.6(a), its obvious that the zonally averaged Eady parameter is dominated by $\sigma_{1B,\,dT/dy}$. That is, *the zonally averaged Eady parameter is dominated by the meridional temperature gradient rather than the Brunt-Väisälä frequency*. All features present in the full Eady parameter in Figure 5.6(a) are also present in the $\sigma_{1B,\,dT/dy}$ plot in Figure 5.6(d), though magnitudes are somewhat different.

Conclusions

In this section, the bandpass SLP, bandpass $Z_{500\,\text{hPa}}$, u, Eady parameter, zonally averaged u and zonally averaged Eady parameter fields from the control run were presented and compared to NCEP/NCAR reanalysis data. The main conclusions are:

The bandpass filter method: The bandpass SLP and bandpass $Z_{500\,\text{hPa}}$ field both display large maxima in the North-Atlantic and Pacific oceans corresponding to the two major Northern Hemisphere storm track, confirming *that bandpass filter is a reasonable approach for storm track studies* when applied to the respective fields.

The bandpass variance fields: Maxima in the bandpass variance field are located in approximately the same regions as maxima in u and the Eady parameter. This confirms that *there is a close connection between bandpass variance, the general circulation and the Eady parameter*.

Validation: The bandpass SLP, bandpass $Z_{500\,\text{hPa}}$, u, Eady parameter, zonally averaged u and zonally averaged Eady parameter all compare very well to corresponding fields from the NCEP/NCAR reanalysis. Magnitudes and structures are generally remarkably similar in all fields. The most prominent difference between CAM3 and the NCEP/NCAR reanalysis is associated with the extrapolation of the SLP field in regions of high topography (Hurrell et al., 2006), but this does not seem to affect the storm track maxima. Also, the North-Atlantic storm track is too zonal in the exit region in the control run.

The most important conclusion from this section is that *CAM3 is able to produce fields which closely resemble the NCEP/NCAR reanalysis, and is therefore suited for sensitivity studies.*

5.2 The T85 control run

Abstract

This section presents the bandpass SLP, bandpass $Z_{500\,\mathrm{hPa}}$, u and Eady parameter fields from the T85 control run and compares the fields to the T42 control run and the NCEP/NCAR reanalysis to find effects of increasing the horizontal resolution. Findings are:

Bandpass SLP: *The Pacific maximum is weakened and the North-Atlantic maximum is strengthened, thus the agreement with the NCEP/NCAR reanalysis is worse except in the North-Atlantic storm track exit region where the increase yields a more pronounced northward tilt.*

Bandpass $Z_{500\,\mathrm{hPa}}$: *The Pacific maximum is strengthened and thus improved. The North-Atlantic maximum is increased and thus worsened, except from in the storm track exit region where it yields an improved northward tilt.*

u: *The Pacific maximum yields decreased values and is overall improved. The North-Atlantic maximum is mostly unaltered except in the exit region where again increased values yield a northward tilt relative to the T42 control run.*

Eady parameter: *Changes are as seen in u, with improvements in the Pacific and the North-Atlantic storm track exit region.*

The general conclusion is that increasing the horizontal resolution from T42 to T85 yields small differences which are not necessarily improvements with respect to the NCEP/NCAR reanalysis.

Given the dramatic increase in run-time when using T85 resolution, we decided to focus on T42 resolution for the sensitivity studies.

A question which naturally comes to mind when comparing results from AGCMs like CAM3 to reanalysis data is: "will the fields improve with respect to the reanalysis with higher resolution?". If the answer is yes, another question naturally follows: "are the fields improving enough to make up for the increased run-time?". This section will answer these questions for the purposes of this project.

As mentioned in section 3.1, the control run was run twice: once with T42 resolution and once with T85 resolution in the horizontal. Notice that the NCEP/NCAR reanalysis was run with T68 resolution, meaning that the T85 control run has higher resolution in the horizontal than the NCEP/NCAR reanalysis. Recall that results from the T42 control run were presented in the previous section. In this section, results from the T85 control run are presented in terms of bandpass SLP, bandpass $Z_{500\,\mathrm{hPa}}$, u and the Eady parameter and compared to both the T42 control run and the NCEP/NCAR reanalysis, taking the NCEP/NCAR reanalysis to be "the truth".

Bandpass SLP

Figure 5.7(a) shows the bandpass SLP field from the T85 control run. Comparing this figure to the corresponding figure from the T42 control run in Figure 5.1(a) on page 53, several features have changed slightly. In the storm track regions, the North-Atlantic maximum has intensified while the Pacific maximum has diminished. In the previous section it was seen that compared to the NCEP/NCAR reanalysis in Figure 5.1(b), the T42 control run bandpass SLP field displayed a storm track maximum in the North-Atlantic which was too strong and a storm track maximum in the Pacific which

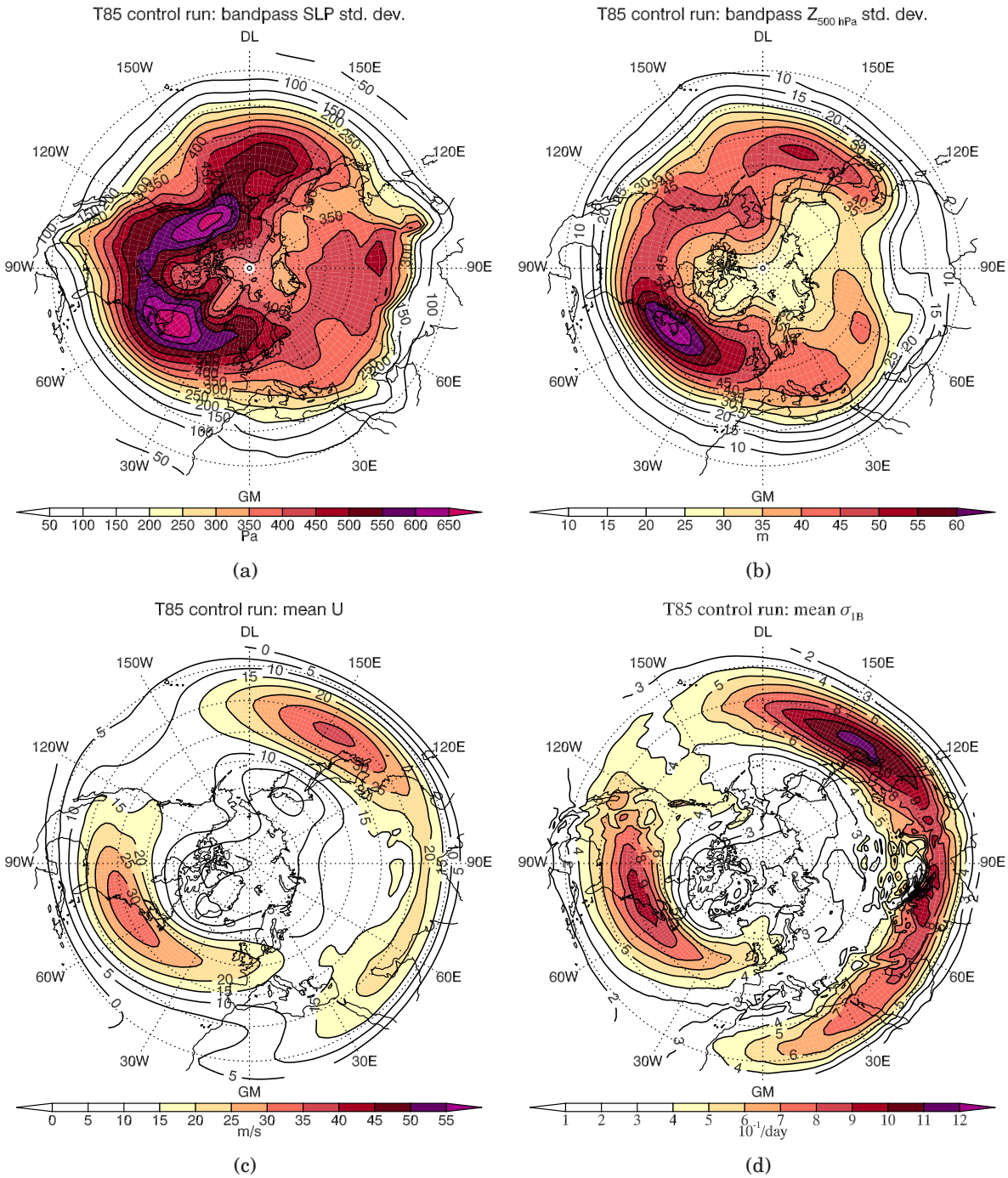

Figure 5.7: *(a), (b), (c) and (d) show the bandpass SLP, bandpass $Z_{500\,\mathrm{hPa}}$, u and Eady parameter fields from the T85 control run.*

was generally too weak. Thus, *increasing the horizontal resolution does not improve the magnitude of the storm track maxima in terms of bandpassed SLP with respect to the NCEP/NCAR reanalysis.*

In the North-Atlantic storm track exit region, bandpass variability has increased somewhat in the Norwegian Sea yielding a more pronounced northward tilt. *Thus, increasing the horizontal resolution improves storm track structure in the North-Atlantic storm track region with respect to the NCEP/NCAR reanalysis.*

In the previous section, it was seen that bandpass variability was too large over high topography in the T42 control run. Looking at Figure 5.7(a), variability has increased over the Rockies and Central Asia near the Himalayas. *Increasing horizontal resolution does not improve the topography related biases in the bandpass SLP field.*

Bandpass $Z_{500\,\mathrm{hPa}}$

Figure 5.7(b) shows the bandpass $Z_{500\,\mathrm{hPa}}$ field from the T85 control run. The corresponding figure from the T42 control run is shown in Figure 5.2(a) on page 54. Comparing these two, it is obvious that bandpass variability has generally increased everywhere in the T85 control run. In particular, the North-Atlantic and Pacific storm track maximum are stronger. This improves the Pacific maximum with respect to the NCEP/NCAR reanalysis in Figure 5.2(b) on page 54. The North-Atlantic maximum on the other hand, was already too strong in the T42 run, and is now even stronger compared to the NCEP/NCAR reanalysis. *Increasing the horizontal resolution improves the magnitude of the Pacific maximum and worsens the magnitude of the North-Atlantic maximum with respect to the NCEP/NCAR reanalysis.*

In the North-Atlantic exit region, bandpass variability has again increased in the Norwegian sea yielding a more pronounced northward shift. *Increasing the horizontal resolution improves the structure of the North-Atlantic maximum in the storm track exit region.*

u

Figure 5.7(c) shows u from the T85 control run, and Figure 5.3(a) on page 57 shows the corresponding figure from the T42 control run. Comparing the figures, the Pacific maximum is reduced in the T85 control run. This is an improvement with respect to the NCEP/NCAR reanalysis in Figure 5.3(b) on page 57, as the Pacific maximum is too strong in the T42 control run. The North-Atlantic maximum is pretty much left unaltered in the T85 control run, except in the exit region where the 20 m/s contour is displaced slightly northward in the T85 control run consistent with a more pronounced tilt observed in the bandpass SLP and bandpass $Z_{500\,\mathrm{hPa}}$ fields. Accompanying the northward tilt are reduced values over the Mediterranean. *Increasing the horizontal resolution improves the magnitude of the Pacific maximum and the structure of the North-Atlantic maximum.*

The u field is overall improved with respect to the NCEP/NCAR reanalysis except from in the eastern Pacific, where values are too low.

Eady parameter

Figure 5.7(d) shows the Eady parameter from the T85 control run, and Figure 5.4(a) on page 58 shows the corresponding figure from the T42 control run. Again, comparing the two figures, the Pacific maximum is clearly reduced in the T85 control run compared to the T42 control run. This improves the Pacific maximum with respect to the NCEP/NCAR reanalysis in Figure 5.4(b) on page 58. As with the u field, the magnitude of the North-Atlantic maximum is left pretty much unaltered, except in the exit region where values have increased in the Norwegian Sea. *Increasing the horizontal resolution yields improvements in the magnitude all over of the Pacific storm track and in the North-Atlantic storm track exit region*.

Magnitudes have decreased over the Mediterranean and in the eastern Pacific, also improving the Eady parameter field with respect to the NCEP/NCAR reanalysis. Other changes are evident over the Rockies and the Himalayas where the T85 control run field displays more fine-structure.

Conclusions

In this section, the bandpass SLP, bandpass $Z_{500\,\mathrm{hPa}}$, u and Eady parameter fields from the T85 control run were compared to the T42 control run and the NCEP/NCAR reanalysis to see whether increasing the horizontal resolution improves CAM3 with respect to the NCEP/NCAR reanalysis. Findings are:

The North-Atlantic storm track: The magnitude of the North-Atlantic storm track maximum worsen with respect to the NCEP/NCAR reanalysis in both the bandpass SLP and the bandpass $Z_{500\,\mathrm{hPa}}$ field and is unaltered in u and the Eady parameter except in the exit region.

The structure of the North-Atlantic maximum improves in all fields, yielding a more pronounced northward tilt.

The Pacific storm track: The magnitude of the Pacific storm track maximum improve with respect to the NCEP/NCAR reanalysis in the bandpass $Z_{500\,\mathrm{hPa}}$ field, u and the Eady parameter, and worsen in the bandpass SLP field.

SLP bias: The topography related issues in the bandpass SLP field (see section 5.1) are not improved.

Some aspects of the fields have improved slightly, other aspects have actually worsened. Although increasing the model resolution is believed to improve the results, particularly in SST anomaly studies (Lau, 1997), the opposite is true for some aspects of the fields presented in this section actually worsen.

Due to the dramatic increase in run-time associated with increasing the horizontal resolution from T42 to T85 combined with the fact that the fields are not sufficiently large to justify the increased run time. *T42 resolution is considered sufficient for sensitivity studies*.

5.3 The TA2 NH run

Abstract

This section investigates the changes in the bandpass $Z_{500\,\mathrm{hPa}}$, bandpass SLP, u, Eady parameter, zonally averaged Eady parameter, diabatic heating and zonally averaged temperature fields to a 2 K SST anomaly in all oceanic grid points north of 45°S in the TA2 NH run. Findings are:

Bandpass $Z_{500\,\mathrm{hPa}}$: *Warming yields a northeastward shift in the North-Atlantic and an intensification in the Pacific storm track regions.*

Bandpass SLP: *Warming yields similar changes as in bandpass $Z_{500\,\mathrm{hPa}}$.*

u: *Warming yields a northeastward shift in both storm track regions.*

Eady parameter: *Difference maxima are found in the North-Atlantic and Pacific storm track entrance regions. Changes are clearly linked to changes in mean u. The zonally averaged Eady parameter shifts upward and poleward, corresponding to results in Yin (2005). The response in the zonally averaged Eady parameter is caused by changes in $\sigma_{1B,\,dT/dy}$.*

Diabatic heating: *Latent heat flux is the main contributor, and generally increases over the Northern Hemisphere oceans, particularly at low-latitudes.*

Zonally averaged temperature: *Warming yields an increased high-level and a decreased low-level temperature gradient. The change is not symmetric. Findings are again consistent with Yin (2005).*

The changes in the zonally averaged temperature and the zonally averaged Eady parameter are remarkably similar to results in Yin (2005), a climate scenario study. This suggests that ocean warming is the primary factor affecting observed changes in the storm tracks.

This section presents results from the TA2 NH run. As described in section 3.1, in this run *a SST anomaly of 2 K was added to the SST field in all oceanic grid points north of 45°S*. The SST anomaly was imposed in all 12 months. The ice coverage field was left unaltered as well as temperature in grid points located over land or ice. The SST anomaly in TA2 NH run is shown in Figure 3.3(a) on page 35, and represents the only difference between the TA2 NH run and the control run. Remember that all the modified runs have T42 resolution in the horizontal.

In the following the bandpass $Z_{500\,\mathrm{hPa}}$, bandpass SLP, u, Eady parameter, zonally averaged Eady parameter, latent heating and zonally averaged temperature field from the TA2 NH run will be shown as full field plots and as difference plots. *Difference plots are always defined as the difference between the full field from the respective modified run, in this case the TA2 NH run, and the corresponding field from the control run.* Difference plots display the response to the SST anomaly.

Bandpass $Z_{500\,\mathrm{hPa}}$

Figure 5.8(a) shows the bandpass $Z_{500\,\mathrm{hPa}}$ field from the TA2 NH run. The full $Z_{500\,\mathrm{hPa}}$ field from the TA2 NH run is very similar to the corresponding field from the control run (Figure 5.2(a) on page 54). To investigate the response to SST anomaly, the main focus will be on the difference plot. This is true for all the remaining fields presented in this section.

Figure 5.8(b) shows the bandpass $Z_{500\,\mathrm{hPa}}$ difference plot. The pink contours are the 40 m and 45 m contours from the con-

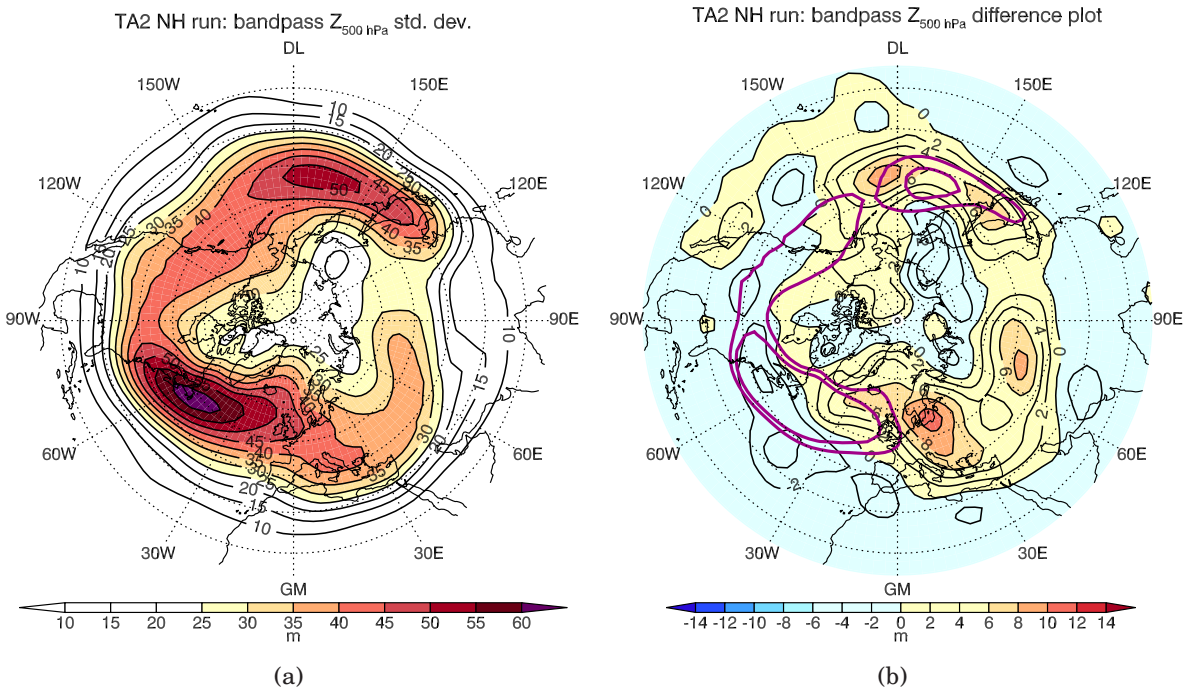

Figure 5.8: *(a) shows the full bandpass $Z_{500\,\mathrm{hPa}}$ field and (b) shows the difference plot, that is the difference between (a) and Figure 5.2(a) on page 54. The pink contours are the 40 m and 45 m contours from the control run representing the approximate position of the storm track in terms of the bandpass $Z_{500\,\mathrm{hPa}}$ field.*

trol run (Figure 5.2(a) on page 54) which helps indicate the approximate position of the storm track in terms of the bandpass $Z_{500\,\mathrm{hPa}}$ field.

In the Atlantic and over North-America, bandpass variance has generally decreased south of 50°N and increased in a band north of this latitude, though the changes are not symmetric. The most pronounced change is over northern Europe, the largest change being centered over the Baltic Sea. Thus, *bandpass variance has decreased in the North-Atlantic storm track entrance region and increased in the exit region*. Judging from the pink contours, it is not obvious that these changes represent a northward shift in the North-Atlantic storm track. Rather, it looks like a *northeastward shift*.

In the western Pacific, bandpass variance had generally increased allover the storm track region with maxima over North-Japan and in the middle of the Pacific. *There is no obvious shift in the latitudinal position of the Pacific storm track*.

Over Europe, bandpass variance has increased in the region between 30 and 80°N. This band continues throughout eastern Europe and Asia, narrowing somewhat in the meridional direction, and displays a maximum over Central Asia. Bandpass variance is found to decrease slightly over parts of the Arctic Ocean, west of Greenland and northern Russia with a minima over the Chukchi Peninsula.

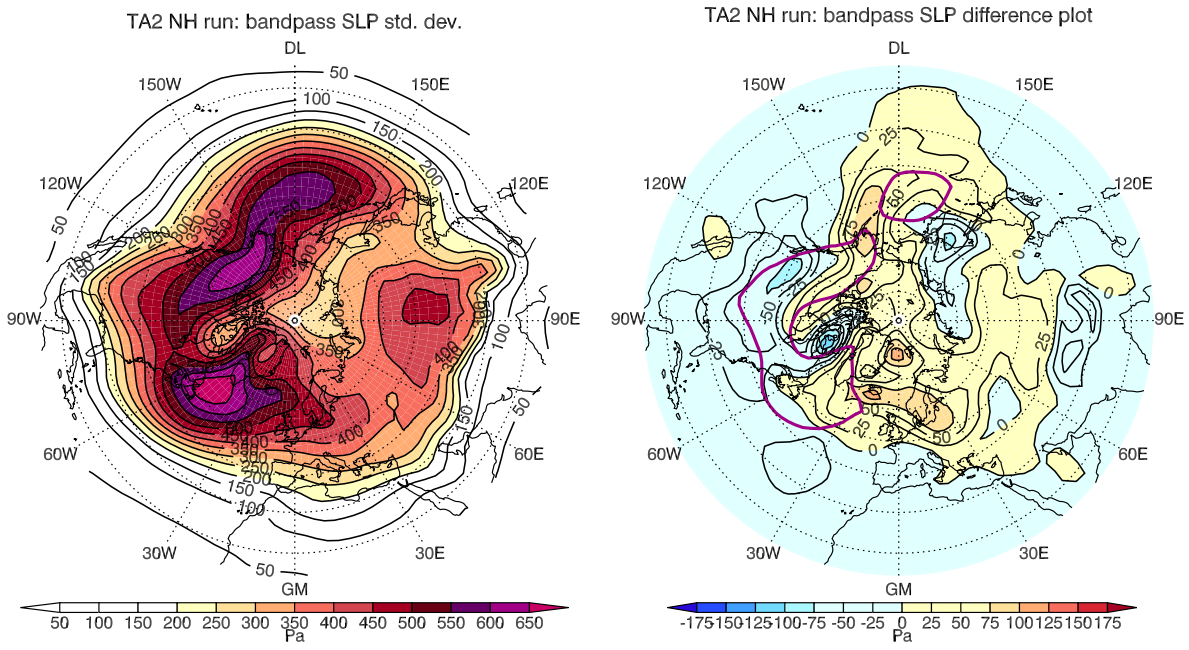

Figure 5.9: *(a) shows the full bandpass SLP field from the TA2 NH run and (b) shows the difference plot from the same run. The pink contours are the 500 Pa contours from the control run in Figure 5.1(a) on page 53, indicating the approximate position of the storm track in terms of the bandpass SLP field.*

Bandpass SLP

The bandpass SLP difference plot shown in Figure 5.9(b). The pink contours are the 500 Pa contours from the controle run in Figure 5.1(a) on page 53. The pink contours are included to help indicate the approximate position of the storm track in terms of the bandpass SLP field.

The response to the SST anomaly in the bandpass SLP field is similar, but not identical, to the response in the bandpass $Z_{500\,\mathrm{hPa}}$ field. In the North-Atlantic, bandpass variance is reduced over North-America and parts of the storm track entrance region south of 50°N. North of 50°N, bandpass variance has generally increased with maxima southeast and northeast of Greenland. Relatively large values are also seen over the Baltic Sea where the largest maximum was found in the bandpass $Z_{500\,\mathrm{hPa}}$ difference plot. *There are indications of a northeastward shift in the North-Atlantic storm track*, but the changes are not symmetric.

In the Pacific, bandpass variance has generally increased allover the storm track region, similar to the bandpass $Z_{500\,\mathrm{hPa}}$ field. A maximum is found southwest of Alaska. Again, *there appears to be a downstream shift in the Pacific storm track*.

Over Central Europe, positive values extend into eastern Europa and Asia, but not as far south as in the bandpass $Z_{500\,\mathrm{hPa}}$ dif-

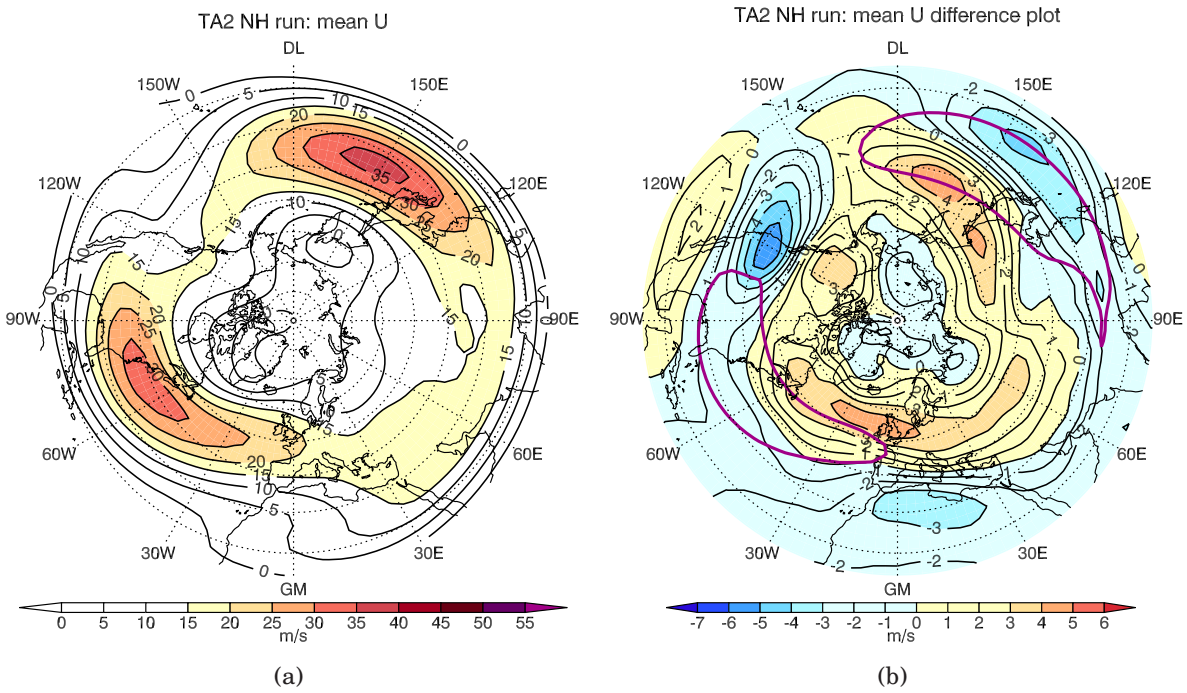

Figure 5.10: *(a) shows the full mean u plot from the TA2 NH run and (a) shows the difference plot. The pink contours corresponds the 20 m/s contours from the control run Figure 5.3(a) on page 57.*

ference plot, and there is no maximum corresponding to that found over Central Asia in the bandpass $Z_{500\,\mathrm{hPa}}$ difference plot.

Over the Arctic, bandpass SLP field values have generally increased. The only exceptions are over the Chukchi Peninsula, a feature also seen in the bandpass $Z_{500\,\mathrm{hPa}}$ field, and over Baffin Island. The minimum over Baffin Island must be caused by shallow features, as it is not seen in the bandpass $Z_{500\,\mathrm{hPa}}$ field.

u

Figure 5.10(b) shows the u difference plot. The pink contours are the 20 m/s contours from the control run in Figure 5.3(a) on page 57 to help determine where the changes happen with respect to the u maxima in the control run.

Figure 5.10(b) clearly shows that u has increased in a band around the Arctic ocean with maxima in the eastern North-Atlantic over Great Britain, in the western Pacific and a smaller maximum just east of Alaska. South of this positive band is a band of negative values, also surrounding the pole. Minima are approximately located south of the previously mentioned maxima, though changes are not symmetric. With respect to the pink contours, *there seems to be a northeastern shift in u in the North-Atlantic and the Pacific. Thus, the mean circulation changes in response to the SST anomaly*.

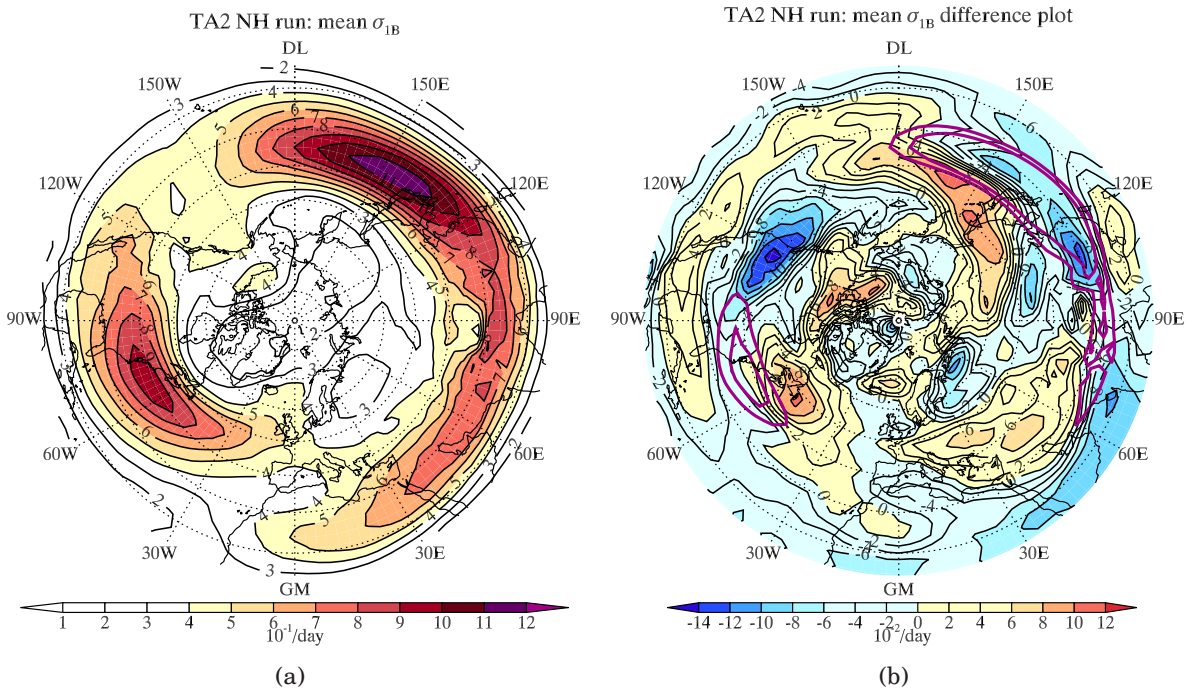

Figure 5.11: *(a) shows the full Eady parameter (σ_{1B}) plot from the TA2 NH run, and (b) shows the difference plot. The pink contour is the 0.8/day 0.9/day contour from the control run in Figure 5.4(a). Notice that the scale on the difference plot is one order of magnitude smaller than the full field plot.*

Eady parameter

Figure 5.11(b) shows the Eady parameter difference plot. The pink contours are the 0.8/day and 0.9/day contours from the control run in Figure 5.4(a) on page 58. The most important features of the Eady parameter difference plot are in the storm track entrance regions where maxima are found off the east coast of North-America and Asia.

Comparing the Eady parameter and the $Z_{500\,\mathrm{hPa}}$ bandpass fields in Figure 5.4(a) and Figure 5.2(a), maxima in the bandpass $Z_{500\,\mathrm{hPa}}$ field are located downstream from the maxima in the Eady parameter. From this one might expect maxima in the Eady parameter difference plot to be found upstream from the maxima in the $Z_{500\,\mathrm{hPa}}$ bandpass difference plot. This is consistent with what is observed the North-Atlantic where, as previously mentioned, the Eady parameter difference plot displays maxima in both storm track entrance region while the bandpass $Z_{500\,\mathrm{hPa}}$ difference plot display maxima in the storm track exit region. Similarly, the reduction in bandpass variance in the bandpass $Z_{500\,\mathrm{hPa}}$ difference plot over North-America and the storm track entrance is located downstream from the strong minimum of the Eady parameter difference plot over the west coast of North-America. In the Pacific on the other hand, maxima in the Eady parameter difference plot and bandpass $Z_{500\,\mathrm{hPa}}$ difference plot

are almost in the same location.

In section 5.1 a remarkable resemblance was seen between the u field (Figure 5.3(a)) and the Eady parameter (Figure 5.4(a)). Now, a similar resemblance is seen between the main features of the Eady parameter difference plot and the u difference plot in Figure 5.10(b). E.g. the maximum-minimum-maximum structure over western North-America, the minimum-maximum structure off the east coast of Asia and positive values in the North-Atlantic storm track entrance region and over central Europe. *Changes in the Eady parameter appear to be tied to changes in* u.

It must be noted that it is difficult to properly infer how changes in the Eady parameter are actually related to changes in bandpass variance. The Eady parameter is a measure of atmospheric baroclinicity, and at mid-latitudes, change in atmospheric baroclinicity in a region is expected to change the cyclogenesis rate in the same area. To properly assess the relationship between changes in the Eady parameter and storm track features, a Lagrangian method would doubtlessly by superior as it tracks cyclones from cyclogenesis to cyclosis and therefore reveals where cyclones are formed.

Zonally averaged Eady parameter

Figure 5.12(b), Figure 5.12(c), Figure 5.12(d) shows the zonally averaged Eady parameter, $\sigma_{1B,N}$ and $\sigma_{1B,\,dT/dy}$difference plot, respectively. Remember from section 2.2.5 and section 5.1 that $\sigma_{1B,N}$ and $\sigma_{1B,\,dT/dy}$ are the contributions to the Eady parameter from the Brunt-Väisälä frequency and the meridional temperature gradient, as defined in equation (2.8) and equation (2.7) on page 17. The reference values are as in section 5.1. The pink contours are the 0.6/day and 0.7/day contours from the control run in Figure 5.6(a) on page 63.

Figure 5.12(b) shows a large maximum at tropopause level with a minimum and smaller maximum directly above it. The response at high-levels (above 400 hPa) north of this maximum is generally positive. The response below the large maximum is generally negative. The figure clearly shows *an upward and poleward shift in the zonally averaged Eady parameter* with respect to the pink contours.

These findings are remarkably similar to the results of Yin (2005). As described in section 2.4.4, Yin (2005) performed a climate scenario study investigating the atmospheric response in increased greenhouse gases to, among other fields, the eddy kinetic energy field and the Eady parameter field. Yin (2005) found the storm tracks, in terms of bandpass filtered eddy kinetic energy variance, to shift upward and poleward. Consistent with changes in the storm track, the Eady parameter was also found to shift upward and northward. The filled contours in the upper left figure in Figure 2.14 shows to response in the Eady parameter to the greenhouse gas forcing in Yin (2005). This is very similar to the changes in the zonally averaged Eady parameter in Figure 5.12(b). The only difference is that in Figure 2.14, the response in the zonally averaged Eady parameter is negative at low levels in the entire Northern Hemisphere. According to Yin (2005), this is caused by an off-set in the low-level Northern Hemisphere temperature gradient due to a reduction in the hor-

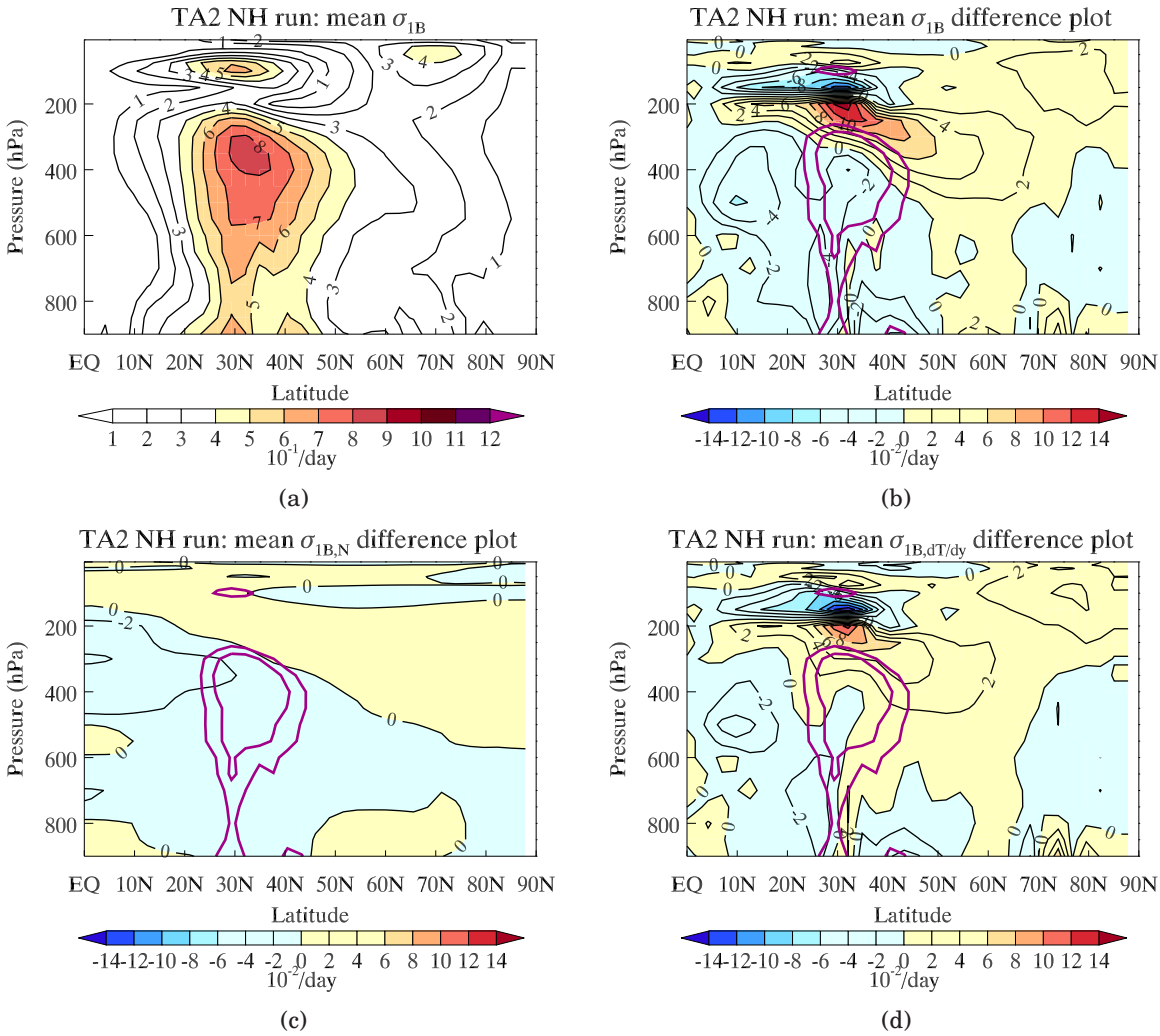

Figure 5.12: *Zonally averaged eady parameter plots for the TA2 NH run. (a) is the complete zonally averaged eady parameter and (b) is the difference from the corresponding plot from the control run (not shown). (d) is $\sigma_{1B,\,dT/dy}$ difference plot and (c) is the $\sigma_{1B,N}$ difference plot. $\sigma_{1B,\,dT/dy}$ and $\sigma_{1B,N}$ are as defined in in equation (2.8) and equation (2.7) on page 17 with reference values identical to those in section 5.1. The pink contours are the 0.6/day and 0.7/day contours from the control run in Figure 5.6(a).*

izontal and vertical extent of sea ice. As the CAM3 model was run with prescribed ice coverage, and the ice coverage field was left unaltered in the TA2 NH run, such effects cannot affect the results in the zonally averaged Eady parameter in Figure 5.12(b). At low levels, the TA2 NH run response in the zonally averaged Eady parameter is more similar to what is seen in the Southern Hemisphere in Figure 2.14 where ice has not significantly influenced the results. Thus, the changes in the zonally averaged Eady parameter are consistent with the results of Yin (2005) taking the differences in

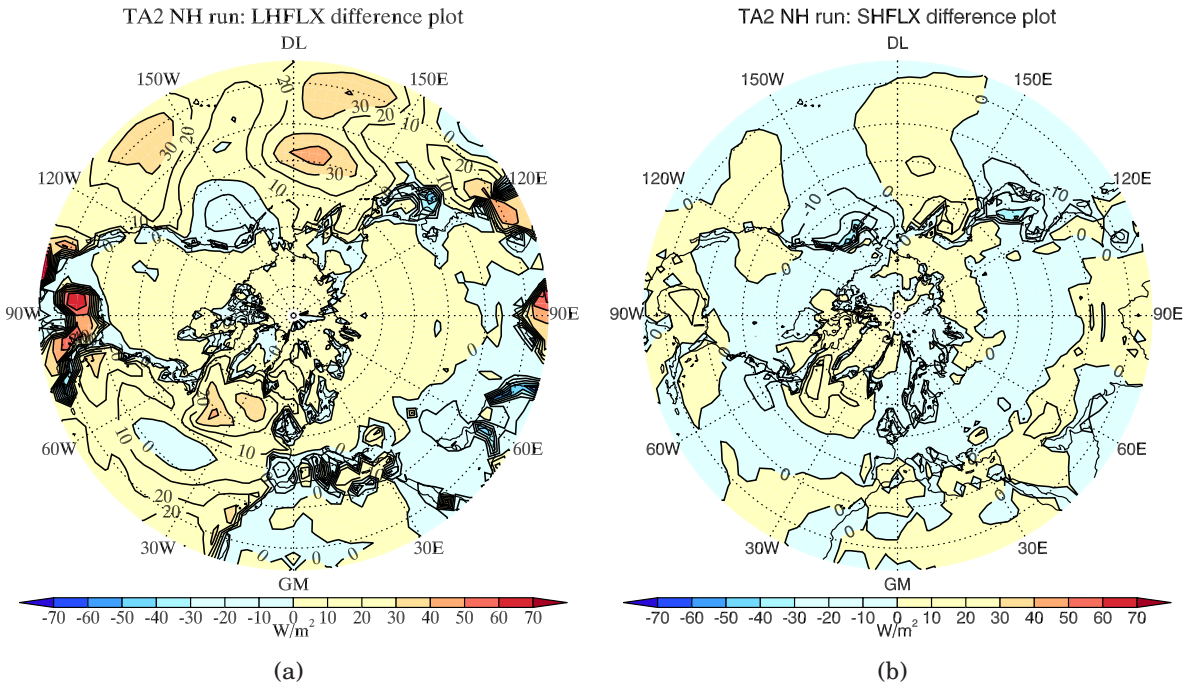

Figure 5.13: *(a) and (b) show the surface latent and sensible heat flux difference plots, respectively.*

the representation of ice into account.

Comparing Figure 5.12(c) and Figure 5.12(d) to Figure 5.12(b), it is clear that the changes in the zonally averaged Eady parameter are very similar to the changes in zonally averaged $\sigma_{1B,\,dT/dy}$. *Changes in the zonally averaged Eady parameter are due to changes in the meridional temperature gradient.* By thermal wind balance, this mean that changes in the zonally averaged Eady parameter are caused by changes in the vertical wind shear.

Diabatic heating

So far, changes caused by the imposed SST anomaly have been examined in the bandpass $Z_{500\,\mathrm{hPa}}$, bandpass SLP, u, Eady parameter and zonally averaged Eady parameter fields. The difference plots have revealed that the storm tracks seem to shift northeastward in the North-Atlantic and intensify in the Pacific. The changes in bandpass variance in the storm track regions seem to follow the changes in u and the Eady parameter. The zonally averaged Eady parameter reveled an upward and northward shift in atmospheric baroclinicity which was caused by changes in the meridional temperature gradient.

The SST anomaly imposed in the TA2 NH run represents an energy source which changes the meridional temperature distribution, which in turn alters u and the atmospheric baroclinicity and ultimately affects the bandpass variance. Now, the changes in diabatic heating will be investigated. Dia-

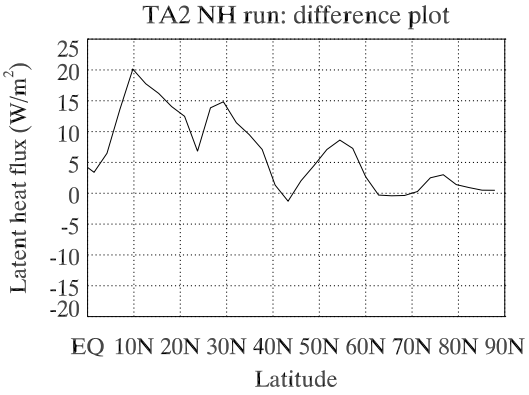

Figure 5.14: *Zonally averaged surface latent heat flux difference plot.*

batic heating is represented by the surface latent and sensible heat fluxes.

Figure 5.13(a) shows the surface latent heat flux difference plot. The field was made from the monthly averaged CAM3 surface latent heat flux field. The figure shows that the latent heat flux difference is generally positive everywhere. *The largest maxima are located south of 30°N* in the Gulf of Mexico, along the west coast of Mexico, and in the Bay of Bengal. In the sub-tropics, smaller maxima are also found in the Pacific. At mid-latitudes, the main maxima are found in the middle of the North-Pacific and North-Atlantic south of Greenland and Iceland. Values are also large over the Kuroshio Current and the Gulf Stream.

Figure 5.13(b) shows the surface sensible heat flux difference plot. The field was made from the monthly averaged CAM3 surface sensible heat flux field. Values are small compared to the surface latent heat flux difference plot. *The response in latent heat flux clearly dominates the response in sensible heat flux.*

Figure 5.14 displays the surface latent heat flux field as a function of latitude. Figure 5.14 displays the zonal average of the field in Figure 5.13(a). The zonally averaged latent heat flux field confirms the findings from Figure 5.13(a); the response is largest at low-latitudes and reaches peak value at 10°N. The second largest peak is found at 30°N, which is the same latitude as the largest maximum in the zonally averaged Eady parameter in Figure 5.12(a). The third largest peak is found at 55°N and the smallest peak is located at 75°N.

So, *the latent heat flux generally increases everywhere, but the increase is larger at low-latitudes*. A large maximum is found at the latitude corresponding to the latitude of maximum baroclinicity in the zonally averaged Eady parameter.

Zonally averaged temperature

Figure 5.15(b) shows zonally averaged temperature difference plot made from the monthly averaged temperature field (the same as was used to find the Eady parameter).

The figure shows that below 100 hPa, the zonally averaged temperature has increased everywhere. A high-level maximum is found in the tropics. Below this maximum, the temperature difference decreases with increasing pressure from the maximum where values exceed 4 K to 0 – 2 K at low-levels. The temperature response is smaller at mid- and high-latitudes where values generally decreases with increasing pressure from 2 – 3 K at low-levels to 0 K at 100 hPa.

It is clear from Figure 5.15(b) that the effect of the imposed SST anomaly in the TA2

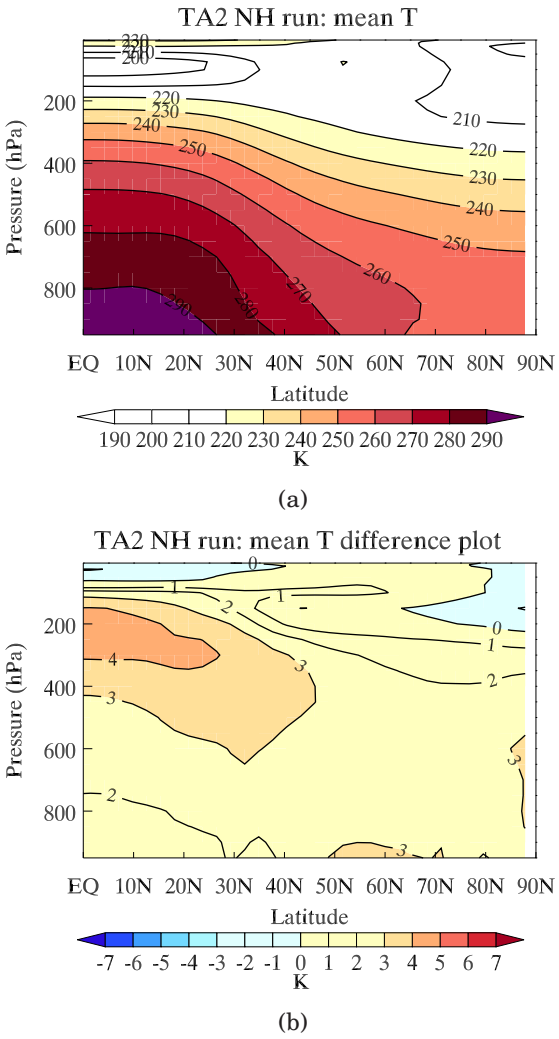

Figure 5.15: *(a) shows the full zonally averaged temperature field and (a) shows the difference plot from the TA2 NH run.*

NH run is to increase the meridional temperature gradient at high-levels and decrease the meridional temperature gradient at low-levels. Notice that the reduction in the low-level temperature gradient is smaller than the increase in the high-level temperature gradient.

Changes in the zonally averaged temperature field are consistent with the results of climate scenario studies (e.g. Yin (2005), Held (1993)). In Yin (2005), the response in zonal temperature to increased concentrations of greenhouse gases is very similar to the results in Figure 5.15(a), the only difference being the low-level warming at high-latitudes seen in Yin (2005). As noted in the previous discussion on the zonally averaged Eady parameter, (Yin, 2005) attributed low-level high-latitude heating to a reduction in the ice cover. As the ice is held fixed in the TA2 NH run, the absence of this particular effect is as expected.

The warming response in Figure 5.15(a) is consistent with the traditional expectation (see section 2.5 and references therein) that SST anomalies in the tropics penetrate further into the atmosphere and cause a greater response due to relatively low static stability and strong convection. SST anomalies at mid- and high-latitudes are unable to penetrate far into the vertical due to relatively strong static stability and are advected in the horizontal rather than in the vertical.

Figure 5.13(a) and Figure 5.13(b) revealed the diabatic heat response to be dominated by the changes in latent heating. *The high-level temperature response in Figure 5.15(b) is therefore probably caused by changes in latent heat flux*.

Conclusions

In this section, results from the TA2 NH run in which an SST anomaly of 2 K was added to all oceanic grid points north of 45°S are investigated in terms of the bandpass $Z_{500\,\mathrm{hPa}}$, bandpass SLP, u, Eady parameter, zonal Eady parameter, diabatic heating and zonal temperature field. Findings

are:

The North-Atlantic storm track: Storm track maximum shifts northeast in the bandpass $Z_{500\,\mathrm{hPa}}$, bandpass SLP field and u.

The Pacific storm track: Storm track maximum do not shift latitudinally in the bandpass $Z_{500\,\mathrm{hPa}}$ field nor the bandpass SLP field, but does appear to shift somewhat downstream in bandpass SLP. In terms of u, the bandpass maxima shifts northeast along with the North-Atlantic maximum.

Zonal averages and Yin (2005): The zonally averaged Eady parameter shifts upward and poleward in response to an increased high-level meridional temperature gradient and a decreased meridional temperature gradient at low-levels. The change in the meridional temperature gradient appears to be mainly attributed to an increase in low-latitude latent heating.

The change in both the zonally averaged temperature difference plot and the zonally averaged Eady parameter difference plot are remarkably similar to results in Yin (2005). This is interesting because Yin (2005) is a climate scenario study investigating the atmospheric response to increased levels of greenhouse gases while this project investigates the response to SST anomalies. *The fact that the response is so similar indicates that ocean warming is the primary factor affecting observed changes in the storm tracks*.

Indications are that the imposed SST anomaly increases the latent heat flux, mainly at low latitudes, yielding changes in the zonally averaged temperature gradient which in turn alter the zonally averaged Eady parameter. In the xy-plane, the general circulation is observed to shift northeast in response to the SST anomaly, accompanied by changes in the Eady parameter and a northeast shift in the North-Atlantic storm track. In the Pacific storm track, a clear latitudinal shift is not seen.

5.4 SST sensitivity

Abstract

In this section, the effects of longitudinal and latitudinal variations in the oceanic heating domain will be investigated by defining three sub-domains of the TA2 NH domain representing heating in high-latitudes (AA2 run), low-latitudes (TML2 run) and all latitudes (TA2 run) in the Atlantic and Arctic (the Pacific being excluded).

TA2 run: *Compared to the TA2 NH run, the bandpass $Z_{500\,\mathrm{hPa}}$, the Eady parameter, u and the latent heat flux are all seen to decrease in the Pacific and increase in the Atlantic, mainly south of 40°N. Excluding the Pacific ocean from the SST anomaly domain obviously yields large changes at low-latitudes in all fields investigated both relative to the control run and the TA2 NH run. There is a strong similarity in structure between the bandpass $Z_{500\,\mathrm{hPa}}$, Eady parameter and u in the TA2 run.*

TML2 run: *Response to oceanic heating in the latent heat flux field is very similar to the results from the TA2 run, indicating that heating the high-latitudes is not important for the response in the presented field.*

AA2 run: *The response to oceanic heating in the latent heat flux field is weak and does not reproduce the main features from the TA2 run and TML2 run.*

The general conclusion is that excluding the Pacific from the heating domain yields large changes in all fields, mainly at low-latitudes south of 40°N where values decrease in the Pacific and increase in the Atlantic.

Comparing the latent heat flux difference fields from the TA2, TML2 and AA2 runs, it is clear that low-latitude heating is the main driver of these changes.

Section 5.3 discussed the TA2 NH run, in which an SST anomaly of 2 K was added to the SST field in all oceanic grid points north of 45°S. The SST anomaly domain is shown in Figure 3.3(a) on page 35.

The change in the zonally averaged temperature field caused by the SST anomaly is very similar to the response seen in Yin (2005), with a increase in the high-level temperature gradient and a decrease in the low-level temperature gradient. In response to the changes in the meridional temperature gradient, the zonally averaged Eady parameter shifted upward and northward, a change consistent with the results in Yin (2005).

In this section, the response longitudinal and latitudinal changes in the SST anomaly domain will be investigated. Three different runs will be presented in which the same SST anomaly of 2 K have been imposed in three different domains, all of which are sub-domains the TA2 NH domain. The three sub-domains are as follows:

High-latitudes and low-latitudes (TA2): This domain stretches from 45°S in the Atlantic all the way up to and including the Arctic Ocean. *A 2 K warming in this specific domain is implemented in the TA2 run*. The domain is shown in Figure 3.3(b) on page 35.

Low-latitudes (TML2): This domain stretches from 45°S to 45 °N in the Atlantic, and is therefore a sub-domain of the larger domains in both the TA2 NH run and the TA2 run. *A 2 K warming in this domain is implemented in the TML2 run*, illustrated in Figure 3.4 on page 36.

High-latitudes (AA2): This domain

stretches from 45°N in the Atlantic into and including the Arctic Ocean. As the low-latitude domain, this domain is a sub-domain of those implemented in the TA2 NH run and the TA2 run. *The high-latitudes domain was implemented with a 2 K warming in the AA2 run* shown in Figure 3.2 on page 33.

For a more complete description of the TA2, TML2 and AA2 runs, consult section 3.1.

In the following, the results from the TA2 run will be presented in terms of bandpass $Z_{500\,\mathrm{hPa}}$, latent heat flux and the Eady parameter and u. The fields will be compared to the TA2 NH run to assess the effect of excluding the Pacific from the SST anomaly domain. Subsequently, the latent heat flux field from the TML2 and AA2 will be presented and compared to the TA2 run to assess the effect of the low-latitude and high-latitude SST anomalies on latent heating.

The TA2 run

Bandpass $Z_{500\,\mathrm{hPa}}$

Figure 5.16(a) shows the bandpass $Z_{500\,\mathrm{hPa}}$ difference plot from the TA2 run. The figure has similar features as in the TA2 NH run in Figure 5.8(b) on page 71. For example, increased bandpass activity over northern Europe and Central Asia, and in the northern Pacific.

Differences are mainly found south of 40°N over the North-Atlantic, Pacific and USA where bandpass activity has increased in the eastern Pacific, over USA and in the North-Atlantic and decreased in the western Pacific. Changes are also found at high-latitudes, e.g. the band of positive bandpass activity in the TA2 NH run located over northern Europe and the Norwegian Sea to have shifted north-west in the TA2 run.

In the TA2 NH run, the North-Atlantic storm track was found to shift northeastward in response to the SST anomaly. Such a shift is not evident in the TA2 run. Instead, the storm track entrance region shifts south, while the exit region shifts north. In the Pacific on the other hand, the storm track appears to shift north. This runs counter to the TA2 NH run where the Pacific storm track position did not display a clear latitudinal shift.

The TA2 run does not yield a clear uniform shift in the North-Atlantic storm track, while the Pacific storm track appears to shift north. Compared to the TA2 NH run, the largest change in bandpass variance is seen at low-latitudes where the North-Atlantic experiences an increase while the Pacific experiences a decrease. Bandpass variance magnitudes are similar in the two runs.

The Eady parameter

The Eady parameter difference plot from the TA2 run is shown in Figure 5.16(b). *The figure shows a clear northward shift in the Pacific* with negative values in the region of the Pacific maximum in the control run (as indicated by the pink contours) and strong positive values in a band north of the pink contours.

In the North-Atlantic, the entrance region appears to shift south while the exit region shifts north with positive values over the maximum region from the control run indicated by the pink contours and a strong maximum southeast of the pink contours.

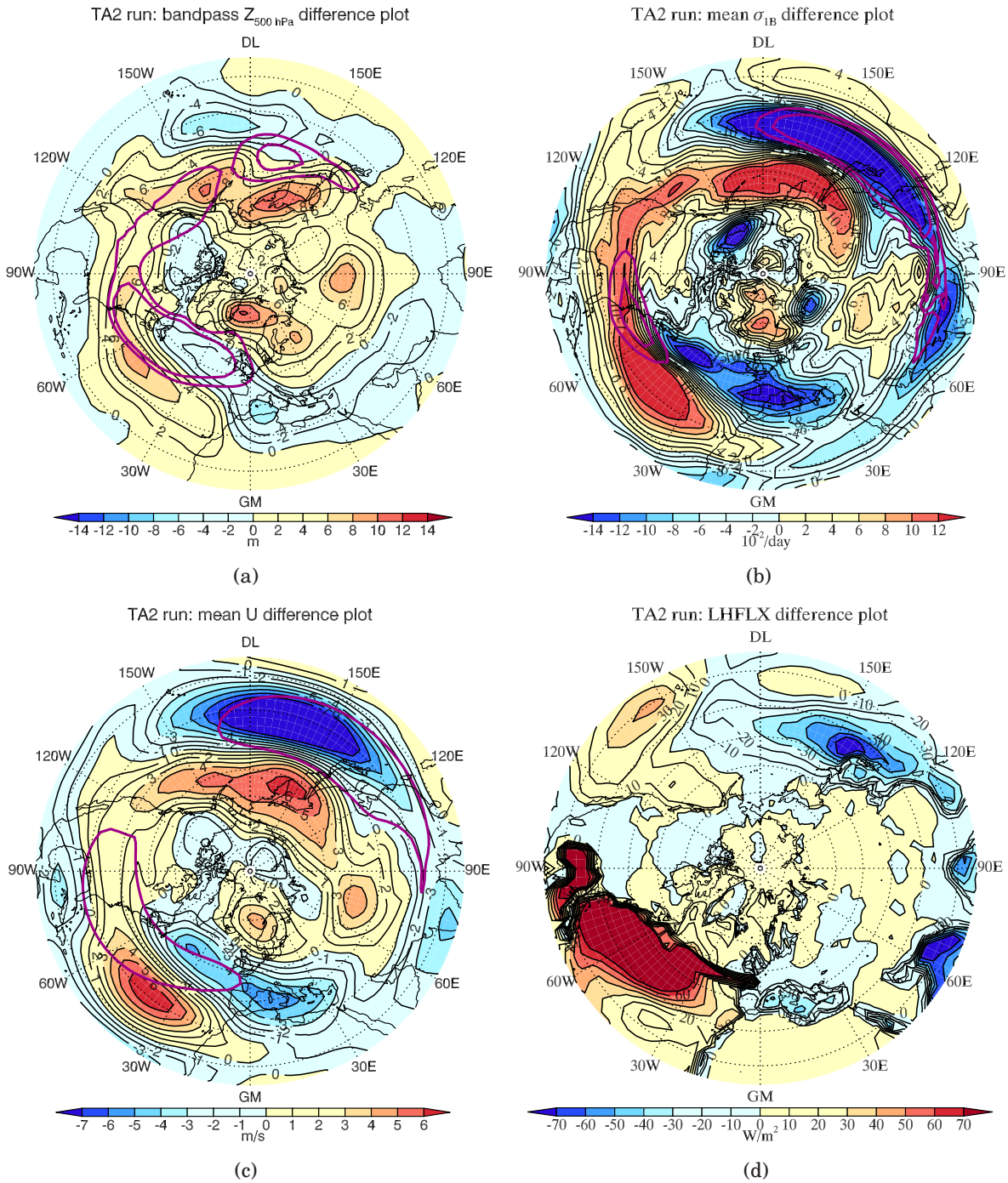

Figure 5.16: *(a), (b), (c) and (d) show the bandpass $Z_{500\,\mathrm{hPa}}$, Eady parameter, u and latent heat flux difference plots from the TA2 run. Pink contours are as in Figure 5.8(b), Figure 5.11(b), Figure 5.10(b) and Figure 5.13(a) on pages 71, 74, 73 and 77.*

North of the band of positive values is a band of negative values. Positive values are again found east of Greenland.

Compared to Figure 5.11(b) on page 74 from the TA2 NH run, there are a few similarities in structure, such as the northward shift in the Pacific and positive values in the North-Atlantic entrance region. *There is no question that the amplitudes of the maxima have greatly intensified in the TA2 run compared to the TA2 NH run, and that the structure has changed significantly in several places.*

One of the most striking tings about the Eady parameter difference plot from the TA2 run is the way the North-Atlantic display a strong maximum at 30°N while the Pacific display a strong minimum at the same latitude. At 50°N, the North-Atlantic display a strong minimum while the Pacific display a strong maximum. This effect is not seen in the TA2 NH run. It is clear from looking at the Eady parameter difference plot from the TA2 run that zonal averaging lead to too much cancellation to make much sense.

Comparing the Eady parameter difference plot to the bandpass $Z_{500\,\mathrm{hPa}}$ difference plot in Figure 5.16(a), it is clear that changes of opposite signs in the two oceans are found in both fields. *There is a clear connection between the Eady parameter and the bandpass $Z_{500\,\mathrm{hPa}}$ field.*

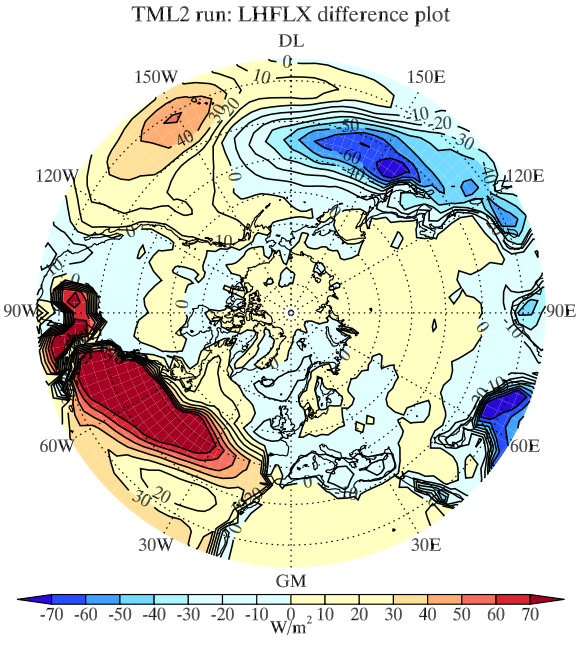

(a)

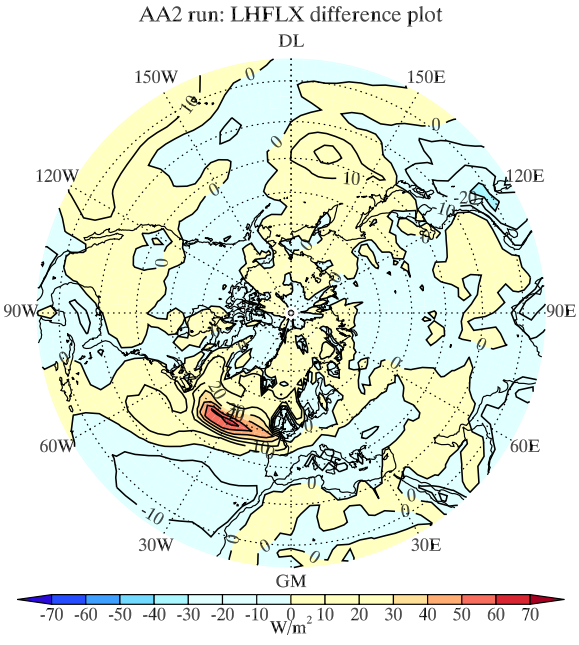

(b)

Figure 5.17: *(a) and (b) show the surface latent heat flux difference plot from the TML2 and AA2 runs, respectively.*

u

Figure 5.16(c) shows the u difference plot from the TA2 run. First of all, the similarity to the Eady parameter difference plot in Figure 5.16(b) is striking. Positive and neg-

ative values are found in the same places and the meridional shifts are the same.

Compared to the TA2 NH run in Figure 5.10(b) on page 73, amplitudes are generally much stronger in the TA2 run. Structure has also changed, particularly in the North-Atlantic, but also in the Pacific. Structure is more zonal in the Pacific in the TA2 run and has shifted northward. In the North-Atlantic, locations of positive values in the TA2 run correspond to negative values in the TA2 NH run. A similar effect is seen over North-America.

The similarity in structure between bandpass $Z_{500\,\mathrm{hPa}}$, Eady parameter and u field from the TA2 run is very strong and again proves the strong connection between the fields. Again the largest difference between the TA2 run and the TA2 NH run is found at low-latitudes.

Latent heat flux

Figure 5.16(d) shows the latent heat flux difference plot from the TA2 run. This figure represents the most dramatic difference between the TA2 run and the TA2 NH run shown in Figure 5.13(a) on page 77. In the TA2 run, a huge maximum is found in the Gulf of Mexico continuing northeastward along the east coast of North-America and crossing the North-Atlantic at about 50°N. In the western Pacific, a large minimum is located over the Kuroshio and a relatively weak maximum is found in the southeastern Pacific. This is in contrast to the TA2 NH run where positive values in the North-Atlantic are much lower than in the TA2 run, and no minimum is found over the Kuroshio.

Excluding the Pacific, yields increased values in the Atlantic and decreased values in the western Pacific. Latent heating south of 50°N represents the largest difference between the TA2 and TA2 NH run.

It is interesting that the latent heat flux decreases in the Pacific. Evidently, the air is warmer, after passing over the Atlantic, so by the time it reaches the Pacific, the air-sea temperature difference is less than it is in the control run. Thus there is less latent heating in the Pacific sector and a smaller change in the Eady parameter.

The TML2 run

In the previous, the TA2 run was compared to the TA2 NH run, and revealed that only heating the Atlantic ocean and neglecting the Pacific lead to large differences in latent heating, primarily at low-latitudes south of 40°N. In the Pacific, latent heat flux was seen to decrease while in the Atlantic, latent heat flux increased at these latitudes. Now, changes in the latent heat flux field resulting from only warming the low-latitudes of the Atlantic in the TML2 run will be investigated.

Figure 5.17(a) shows the latent heat flux difference field from the TML2 run. The figure is very similar to the corresponding figure from the TA2 run with a large minimum in the western Pacific and a large maximum in the Atlantic. A similar relationship is found from investigating the sensible heat flux difference plots from the TA2 run and TML2 run (not shown).

Changes in the bandpass $Z_{500\,\mathrm{hPa}}$ (not shown) and Eady parameter field (also not shown) difference plots from the TML2 run

are very similar to the TA2 run.

Heating low-latitudes and heating both low-latitudes and high-latitudes in the Atlantic yields strikingly similar results in terms of the latent heat flux difference fields.

The AA2 run

As stated in the beginning of this section, the AA2 run represents the high-latitude heating. Now, the latent heat flux from the TA2 run and the AA2 run will be compared.

Figure 5.17(b) show the latent heat flux difference plots from the AA2 run. Obviously, differences from the TA2 run are large. In the North-Atlantic, the TA2 run displays large positive values, particularly in the Gulf of Mexico and up along the east coast of North-America up to 50°N where the maximum stretches across the North-Atlantic towards Europe. The AA2 run difference plot displays a small maximum in the North-Atlantic between 40 and 50°N. South of this feature, values are generally negative. *In the Atlantic, the main difference in latent heat flux between the TA2 and AA2 run is the low-latitude heating*

In the Pacific, the TA2 run displays a maximum in the eastern Pacific and a minimum in the western Pacific as previously mentioned. In the AA2 run on the other hand, changes are small. Values are negative south-west of Japan and positive north-east of Japan and positive values are found at low-latitudes in the eastern Pacific. *In the Pacific, the main difference in the latent heat flux between the TA2 and AA2 run is again low-latitude heating.* The sensible heat flux difference plot (again not shown) displays similar results as the latent heat flux difference plots, only magnitudes are much smaller.

Comparing the latent heat flux difference fields from the TA2 run and AA2 run reveal that heating high-latitudes only yields a weak response to the latent heat flux field and that the primary features of the latent heat flux field from the TA2 run are not reproduced by high-level heating.

Conclusions

In this section, the effects of longitudinal and latitudinal variations in oceanic heating domains were investigated by defining three sub-domains of the TA2 NH domain representing heating in high-latitudes (AA2 run), low-latitudes (TML2 run) and all latitudes (TA2 run) in the Atlantic and Arctic. Findings are:

The Pacific: In the TA2 run, bandpass $Z_{500\,\mathrm{hPa}}$, the Eady parameter, u and latent heat flux all yield a minimum south of 40°N.

The North-Atlantic: Here the opposite effect is seen compared to the Pacific. In the TA2 run, bandpass $Z_{500\,\mathrm{hPa}}$, the Eady parameter, u, and latent hat flux all yield a strong maximum south of 40°N.

Low-latitude heating: The latent heat flux difference plot from the TML2 run closely resembles the corresponding field from the TA2 run. Consequently, the main features of the latent heat flux difference field can be quite accurately reproduced by neglecting the high-latitudes of the Atlantic and Arctic Ocean.

High-latitude heating: The latent heat flux difference plot from the AA2 run fails to reproduce the main features of the TA2 and TML2 run, and the changes are over all small compared to the changes seen in the other runs. Thus, the main latent heat flux difference field cannot be accurately reproduced by high-latitude heating alone.

The largest differences between the TA2 run and the TA2 NH run are found at low-latitudes south of 40°N. *At low-latitudes, excluding the Pacific from the heating domain yields a decrease in all fields investigated in the Pacific, while in the Atlantic all fields are seen to increase* It is interesting that heating the Atlantic and Arctic Ocean yields a decreased latent heat flux in the Pacific.

The similarity in structure between the bandpass $Z_{500\,\mathrm{hPa}}$, Eady parameter and u are again striking.

Comparing the latent heat flux difference field from the TA2 run, TML2 run and AA2 run reveals that the main features of the latent heat flux field resulting from heating both high-latitudes and low-latitudes can be accurately reproduced by low-latitude heating alone, but the same cannot be achieved with high-latitude heating.

From this, indications are that the low-latitude heating resulting from the imposed SST anomaly is the main driver of the observed atmospheric changes.

5.5 The no ice run

Abstract

This section investigates the effects of removing all ice from the Northern Hemisphere in the fields listed below to asses the influence on the storm tracks from reduced ice cover. Findings are:

Bandpass $Z_{500\,\mathrm{hPa}}$: *Changes in bandpass variance are of comparable magnitudes as in the AA2 run, but structure has changed. In terms of bandpass variance, removing the sea ice results in storm track changes of similar magnitudes as high-latitude heating.*

Latent heat flux: *In the storm track regions, the response in latent hating correspond well to observed changes in bandpass variance, the mean circulation and the Eady parameter. Latent heating generally increases in the Arctic, but a corresponding change is not seen in the mean circulation nor in the bandpass $Z_{500\,\mathrm{hPa}}$ field.*

Zonally averaged temperature: *The major change is at high-latitudes low-levels, consistent with the high-latitude increase in latent heating and sensible heating. The change in the zonally averaged temperature field is very similar to findings in Yin (2005).*

Zonally averaged Eady parameter: *Changes are mainly found at high-latitude low-levels. Over the Arctic, the low-level increase corresponds to changes in $\sigma_{1B,\,dT/dy}$.*

Removing the sea ice induces changes on the storm tracks of comparable amplitudes as seen in the AA2 run with the high-latitude heating. A shrinking sea ice cover is therefore not as important as low-latitude heating. The positive latent heat response in the Arctic appears to induce local changes in static stability which does not affect the storm track regions.

In section 5.4, low-latitude heating was seen to be the main driver of the observed latent heat flux changes in the TA2 run. Suggestions are that the storm tracks are not particularly sensitive to high-latitude heating. This proposes that the same might be true for changes in the ice cover. In the TA2 NH, TA2, TML2 and AA2 runs, the ice coverage field was left unaltered. According to the IPCC Fourth Assessment Report (Trenberth et al., 2007), the ice coverage is observed to shrink, thus possible effects of these changes should not be neglected. In this section, the effect of removing all ice from the Northern Hemisphere, will be investigated to determine whether the storm tracks are insensitive to changes in the ice cover.

This section presents results from the no ice run in which all ice has been removed from the entire Northern Hemisphere. Notice that the sea ice coverage in the Southern Hemisphere was left unaltered. Modifications were only made in the ice coverage field in the initial condition data set file as described in section 3.1. Fields presented in this section comprise the bandpass $Z_{500\,\mathrm{hPa}}$ field, the latent heat flux field, the zonal temperature field, zonally averaged diabatic heating (including both latent and sensible heat fluxes) and the zonally averaged Eady parameter field.

Bandpass $Z_{500\,\mathrm{hPa}}$

The bandpass $Z_{500\,\mathrm{hPa}}$ difference plot is shown in Figure 5.18(a). *A general decrease in bandpass activity is seen at high-latitudes* everywhere north of about 50°N, with minima over northern Canada and in the northern Pacific.

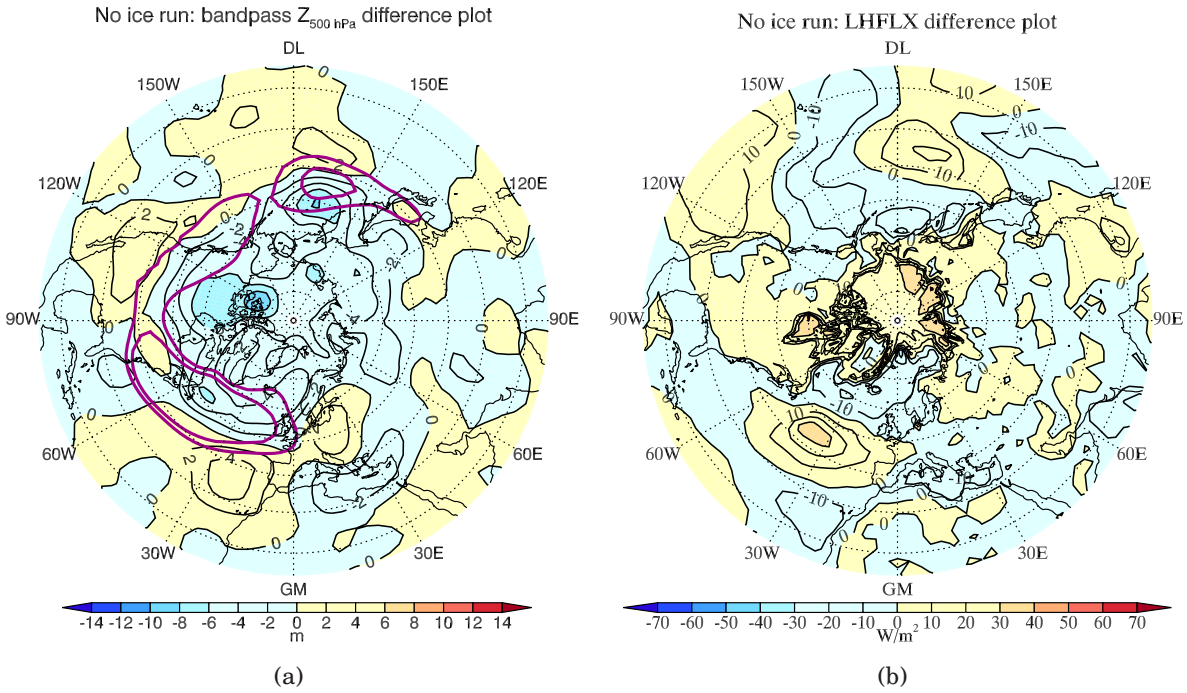

Figure 5.18: *(a) and (b) show the bandpass $Z_{500\,\mathrm{hPa}}$ and latent heat flux difference plots from the no ice run. Pink contours are as in Figure 5.8(b) on page 71.*

Over the oceans at lower latitudes, positive values are found in the eastern Atlantic, the Mid-Pacific and along the west coast of the USA. *There appears to be a southward shift of bandpass activity in both storm track regions*.

The southward shift in bandpass activity is accompanied by a southward shift in u (not shown) and the Eady parameter (also now shown) in the North-Atlantic and central Pacific. At high-latitudes, north of 50°N, the Eady parameter displays a positive response which does *not* correspond to increased bandpass activity *nor* u.

Removing the ice does to some extent affect the bandpass variance, but amplitudes are smaller than in the TA2 NH run and TA2 run difference plots (Figure 5.8(b) and Figure 5.16(a)) on pages 71 and 83). The amplitudes in the bandpass $Z_{500\,\mathrm{hPa}}$ difference plot from the no ice run are comparable to the amplitudes from the corresponding AA2 run plot (not shown), though structure is different.

Latent heat flux

The latent heat flux difference plot is shown in Figure 5.18(b). Compared to the latent heat flux difference field from the AA2 run in Figure 5.17(b), the largest reduction is in the Bering Sea and the North-Atlantic storm track region. Notice that the maximum in the North-Atlantic between 40 and 50 °N is present in both runs, but the magnitude is reduced in the no ice run. The largest increase is over the Arctic where *latent heat flux in the no ice run has generally*

increased where ice has been removed.

The sensible heat flux difference plot (not shown) displays very similar results, the only difference being small minima in the Bering Sea and southwest and northeast of Greenland. The effect of these minima shows up in the zonally averaged sensible heat flux field in Figure 5.19(d).

At latitudes south of 50°N, the maxima and minima in the latent heat flux are accompanied by corresponding maxima and minima in the Eady parameter difference plot (not shown). In the storm track regions, maxima and minima in the Eady parameter correspond well to maxima and minima in the bandpass $Z_{500\,\mathrm{hPa}}$ field. Over the continents and the Arctic, this correspondence is not seen, except from in a few regions.

Changes in u (not shown) correspond well to changes in the Eady parameter at latitudes below 50°N. At *high-latitudes, changes in the Eady parameter are not seen to correspond to changes in* u.

Indications are that *increased latent heating at high-latitudes yields changes in the Eady parameter which are not reflected in the mean circulation*, nor in the bandpass variance field. This runs counter to what is seen at lower latitudes where there is a more clear connection between the Eady parameter, the mean circulation and bandpass variance.

Zonally averaged temperature and diabatic heating

Figure 5.19(a) shows the zonally averaged temperature difference plot. The most striking feature in this figure is the strong low-level heating at high-latitudes, yielding a reduced meridional temperature gradient. A minima is located above the low-level maxima at about 200 hPa.

It is clear from Figure 5.19(a) that *the low-level meridional temperature gradient decreases in response to removing all ice in the Northern Hemisphere*. At high-levels, above 100 hPa, the meridional temperature gradient appears to increase.

Figure 5.19(c) and Figure 5.19(d) show the zonally averaged latent and sensible heat flux difference plots. The most important aspects of these figures is the large positive response in both latent and sensible hating of almost 25 W/m^2 between 70 and 90°N. *The large increase in zonally averaged latent and sensible heat flux justify the large low-level maxima in the zonal temperature field in this region.*

As previously mentioned, Yin (2005) found a low-level high-latitude maxima in the zonally averaged temperature in response to increased levels of greenhouse gases. He attributed the existence of the maxima to reduction of ice in a warmer climate. It is very interesting to notice the same feature is found in this project using an uncoupled atmospheric climate model with all ice removed.

Zonally averaged Eady parameter

The zonally averaged Eady parameter difference plot is shown in Figure 5.19(b). The most pronounced changes are happening at low-levels with a minima between 50 and 65°N and a maximum between 75 and 82°N. The minimum is probably due to the reduction in the low-level meridional temperature seen in Figure 5.19(a). The max-

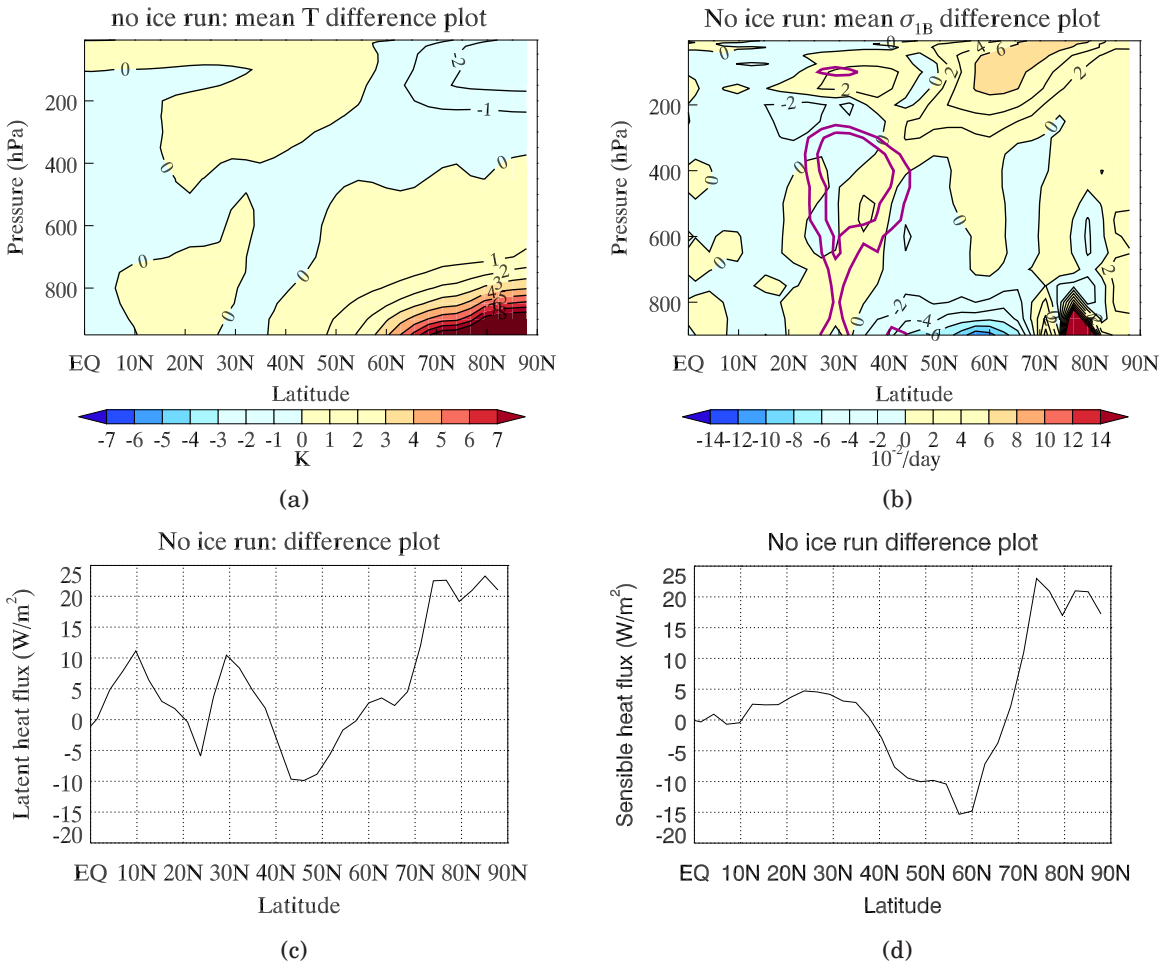

Figure 5.19: *(a), (b), (c) and (d) show the zonally averaged temperature, zonally averaged Eady parameter, zonally averaged latent heat flux and zonally averaged sensible heat flux difference plots, respectively. The pink contours are the same as in Figure 5.12(b) on page 76.*

imum may be some low-level effect over Greenland caused by removing all the inland ice.

In section 5.3, the general structure of the response in the zonally averaged Eady parameter was primarily due to the response in $\sigma_{1B,\,dT/dy}$. This is also primarily the case in the no ice run, except from at low-levels north of 82°N where positive $\sigma_{1B,N}$ values dominates over negative $\sigma_{1B,\,dT/dy}$ values, yielding positive Eady parameter values. Such a strong contribution from $\sigma_{1B,N}$ was not seen in the TA2 NH run (not shown).

It appears that the positive latent heat flux response resulting from removing the ice cover changes the static stability over the Arctic, and thus the response is greater in $\sigma_{1B,N}$ than $\sigma_{1B,\,dT/dy}$. Changes in $\sigma_{1B,N}$ does not appear to be tied to changes in bandpass variance. It is localized in the Arctic and geographically separated from the storm track regions which are further south.

Conclusions

In this section, the effects of removing the entire ice cover from the Northern Hemisphere was investigated to assess the influence of reduced ice cover on the storm tracks. Findings are:

Storm track region: Bandpass variance changes in both storm track regions. The magnitudes of the maxima and minima in the bandpass $Z_{500\,\mathrm{hPa}}$ difference plot are comparable to the AA2 run (not shown), but the structure is different.

Changes in the latent heat flux, Eady parameter (not shown) and u (not shown) difference fields over the storm track regions are consistent with the observed changes in bandpass variance.

The Arctic: As a result of removing the ice cover, the latent heat flux increases all over the affected region in the Arctic. In response to this, static stability changes along with $\sigma_{1B,N}$, but this does not yield corresponding changes in the mean circulation nor bandpass variance.

The general conclusion from this is that *removing the ice induces changes on the storm tracks of comparable amplitudes to those seen in the AA2 run with the high-latitude heating, and is therefore not as important as low-latitude heating*. The positive latent heat response in the Arctic appears to induce local changes in static stability which does not affect the storm track regions.

5.6 Cyclone count from the CCI method

Abstract

This section presents results from the CCI method from Benestad and Chen (2006) in terms of cyclone count from the T42 control run, the NCEP/NCAR reanalysis, the T85 control run and the TA2 NH run. Findings are:

The T42 control run: *Large cyclone count maxima in both storm track regions. Indications are that the CCI method is not as affected by the biased SLP field in regions of high topography as the bandpass filter method. The northward tilt of the North-Atlantic storm track is not accurately reproduced in the T42 control run.*

The NCEP/NCAR reanalysis: *Displays storm track regions that are stronger and more extended downstream compared to the T42 control run. A strong maximum is found in the Norwegian/Barents Sea yielding a pronounced northward tilt to the North-Atlantic storm track.*

T85 control run: *The Pacific storm track is unchanged from the T42 control run. The North-Atlantic storm track has intensified all over, and displays more pronounced northward tilt.*

The TA2 NH run: *Cyclone count have generally decreased in both storm track regions and increased at high-latitudes over the Arctic Ocean and parts of the storm track exit regions.*

Remember from section 4.2 that *the CCI method presented in Benestad and Chen (2006) is a feature point identification method which identifies low-pressure centers in the SLP field*. Feature point identification methods are commonly applied in storm track studies (e.g. McCabe et al. (2001), Hoskins and Hodges (2002)) and represent the storm track from an Eulerian perspective. Results from feature point identification methods yield information about where low-pressure centers reside the most, that is, where they are identified most often. The results have a tendency of being biased towards slow and quasi-stationary cyclones as their slow traveling velocities allow them to be counted many times (Hoskins and Hodges, 2002). A way around this problem is to combine feature point identification with feature point tracking to exclude low-pressure centers with e.g. traveling velocities smaller than a threshold value (e.g. McCabe et al. (2001)). Combining the CCI method with a feature point tracking procedure is beyond the scope of this project.

In this project, the CCI method was applied to the 6 h sea level pressure field from the CAM3 runs and the NCEP/NCAR reanalysis. This section presents results from the T42 control run, the NCEP/NCAR reanalysis, the T85 control run and the TA2 NH run.

Plotting

Sampling in boxes

Cyclone count plots were made by dividing the plotting domain into 14×14 boxes, counting the number of feature points identified within each box and making stereographic contour plots. Changing the number of boxes will, unavoidably, slightly alter the structure in the contour plots. Figure 5.20 shows the plotting domain divided into 14×14 boxes and the total cyclone count from the T42 control run within each box.

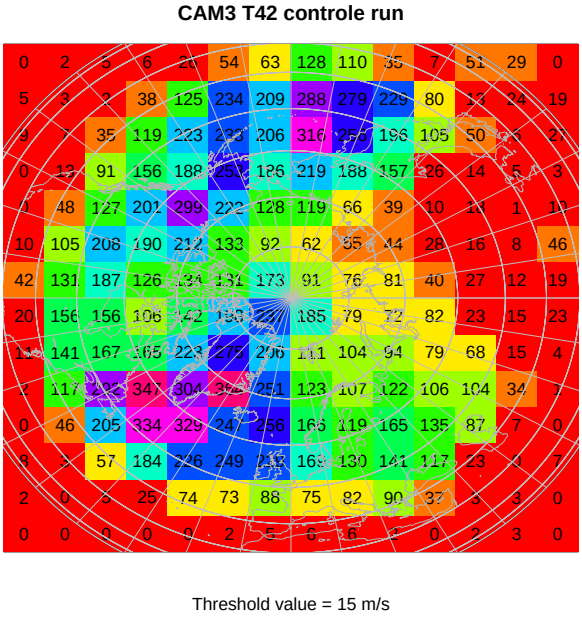

Figure 5.20: *Illustration of how the plotting domain is divided into boxes. The plotting domain includes all latitudes north of 30°N and has been divided into 14×14 boxes (colored squares) for plotting purposes. The black numbers inside the colored boxes are the number of cyclones identified within each square satisfying the threshold values from the T42 control run. The contour plot from the T42 run is shown in Figure 5.21(a).*

When counting the total number of cyclones within each box, a threshold value of some kind is needed to weed out weak low-pressure centers. Traditionally, there has been a widespread use of local minimum pressure to assess the strength of the cyclones (e.g. Benestad and Chen (2006)). Using minimum pressure to measure cyclone strength, a typical threshold value would be 1000 hPa. Then all identified feature points with minimum pressures greater than e.g. 1000 hPa would be rejected. Different threshold values will yield different results. Ulbrich et al. (2009) caution against using minimum pressure as a measure of cyclone intensity in cyclone count studies because of the fact that cyclone centers identified over regions of climatologically low pressures, such as Iceland, will be characterized with a "falsely" low minimum pressure as the difference between the minimum pressure of the cyclone and the background field is not necessarily large. In this way, shallow cyclones over areas climatologically low pressure will dominate the results. To avoid such issues in this project, *maximum wind speed was applied as a measure of cyclone intensity*.

Threshold value

The CCI method finds the gradient wind[7] at the inflection points of the zonal and meridional pressure profiles (the pressure profiles are illustrated in Figure 4.3 on page 47) and returns the maximum value of each identified low-pressure system. The gradient wind is calculated by the `gradient.wind` function in Benestad (2008). *The threshold field in this project is the maximum gradient wind speed, and the threshold value is chosen to be 15 m/s.*

[7]The gradient wind is the path velocity in a horizontal frictionless flow which is only affected by the pressure gradient force, the Coriolis force and the centrifugal force. It is often given in terms of geopotential in natural coordinates (Martin, 2006): $\frac{V^2}{R} + fV = -\frac{\partial \phi}{\partial n}$. where V is the path velocity, R is the radius of curvature, f is the Coriolis parameter, ϕ is the geopotential and n is the coordinate perpendicular to the flow, pointing towards the origin. Solving this for V yields an expression for the gradient wind: $V = -\frac{fR}{2} \pm \sqrt{\frac{f^2R^2}{4} - R\frac{\partial \phi}{\partial n}}$

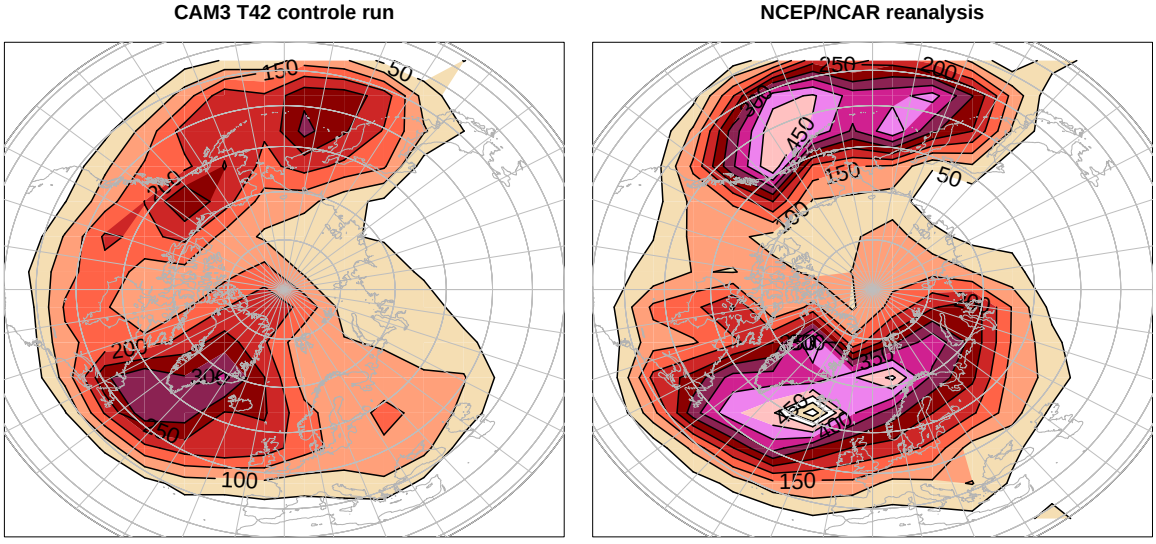

(a) (b)

Figure 5.21: *(a) and (b) show the total cyclone count for the T42 control run and the NCEP/NCAR reanalysis, respectively. The total cyclone counts is the number of observed low pressure centers stronger than the threshold value.*

The T42 control run

The total cyclone count from the T42 control run is displayed in Figure 5.21(a). The structure of the field bears likeness to the structure of the full bandpass SLP and bandpass $Z_{500\,\mathrm{hPa}}$ fields: values are generally low at low-latitudes (notice that the figures shows all latitudes from 30°N to the North Pole). Large values are found in a band stretching from the east coast of Asia to Northern Europe. The main two maxima are located in the North-Atlantic and Pacific, corresponding to the storm tracks. In the North-Atlantic, large values are found stretching from Cape Hatteras to northeast over Greenland and Iceland. In the Pacific, large values are found stretching from northeast of Japan to Alaska. A small maximum is located over Alaska, and a belt of relatively high values continue across North-America. Notice the North-Atlantic maximum is stronger than the Pacific maximum, consistent with the bandpass SLP and bandpass $Z_{500\,\mathrm{hPa}}$ fields in Figure 5.1(a) and Figure 5.2(a) on pages 53 and 54, respectively.

Notice also that the cyclone count maxima have shifted poleward compared to the bandpass SLP maxima. This is consistent with bandpass activity representing *growing baroclinic waves*, while cyclone counting captures more mature systems with longer timescales. Notice also that compared to the storm track region in terms of the bandpass SLP and bandpass $Z_{500\,\mathrm{hPa}}$ fields, storm track regions in terms of cyclone count maxima extend further downstream.

Also, the bandpass SLP maximum associated with the Rockies is not as pronounced in terms of cyclone count as in terms of bandpass SLP. It is weaker than both the North-Atlantic and the Pacific maxima. There is no cyclone count maximum in Asia associated with the Himalayas. *Indications are that the CCI method is not as sensitive to the biased SLP field in regions of high topography as the bandpass filter method.*

The NCEP/NCAR reanalysis

The total cyclone count from the NCEP/NCAR reanalysis is shown in Figure 5.21(b). The most eye catching property of this figure is the fact that *the total cyclone count exceeds the T42 control run cyclone count all over both storm track regions*. The difference is probably greatest in the Pacific where peak cyclone count is between 300 and 350 in the western Pacific in the T42 control run and between 400 and 450 in the same region in the NCEP/NCAR reanalysis. In the eastern Pacific, cyclone count in the T42 control run is between 200 and 250 while the NCEP/NCAR reanalysis displays cyclone counts between 450 and 500 in the same region. The effect is also to a great extent present in the North-Atlantic storm track region where the NCEP/NCAR reanalysis displays a strong maximum southwest of Iceland and in the Norwegian/Barents Sea. Neither of these features show up distinctly in the T42 control run. The presence of the maximum in the Norwegian/Barents Sea makes the storm track look more tilted in the meridional direction in the NCEP/NCAR reanalysis than the T42 control run. *CAM3 fails to accurately reproduce the northward tilt of the North-Atlantic storm track*.

Continuing the comparison between Figure 5.21(a) and Figure 5.21(b) , cyclone count is lower over North-America in the NCEP/NCAR reanalysis than the T42 control run, indicating that CAM3 overestimates the cyclone count in this region, though this is not as pronounced as in the bandpass SLP field.

Comparing the bandpass SLP fields from the T42 control run to the NCEP/NCAR reanalysis (Figure 5.1(a) and Figure 5.1(b)), the CAM3 model overestimated the baroclinic wave activity almost everywhere, except in the Pacific and the Norwegian and Barents Sea. A general overestimation was also seen with u, zonal u, the Eady parameter and the zonal Eady parameter. With the cyclone counting, similar effects are seen in the Pacific and the Norwegian/Barents Sea only much stronger, and the opposite effect is seen in the central North-Atlantic storm track region. *In terms of cyclone count, the CAM3 model underestimates the storm track intensity in both ocean basins.*

These issues may be related to resolution as CAM3 was run with T42 resolution in the horizontal and 26 vertical layers while the NCEP/NCAR reanalysis was run with T68 resolution in the horizontal and 28 vertical layers. Later in this section, the effect of increasing horizontal resolution will be investigated as the as the total cyclone count field from the T85 control run is presented.

In regions of high topography, bandpass activity in terms of the bandpass SLP field was reduced in the NCEP/NCAR reanalysis compared to the T42 control run. This effect is also seen over North-America in terms of cyclone count, though not as pronounced at in the bandpass SLP field. The Himalayas do not appear to be affected as cyclone count is very low in this region. This is generally

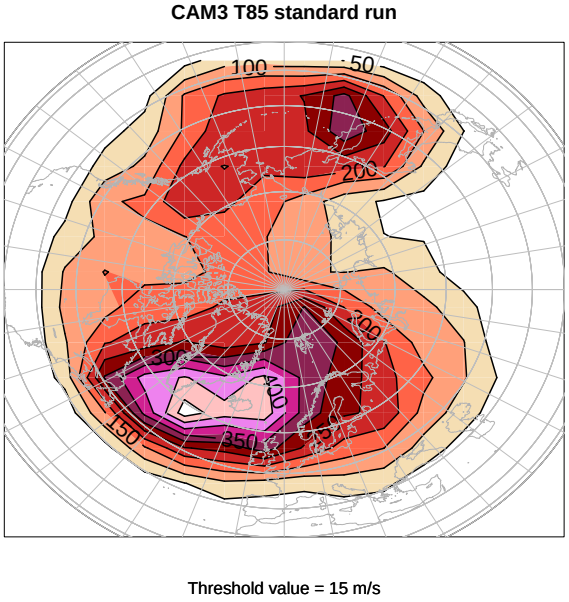

Figure 5.22: *Total cyclone count field from the T85 control run. Otherwise as in Figure 5.21(a)*

true over Central Asia.

The T85 control run

The total cyclone count from the T85 control run is shown in Figure 5.22. *In the Pacific storm track region, structure and intensity is similar to the T42 control run.* The small maximum located over Alaska in the T42 control run, is missing in the T85 control run, which is an improvement as the maximum is not present in the NCEP/NCAR reanalysis. Over North-America, cyclone count is generally reduced in the T85 control run, but cyclone count has increased over the Arctic Ocean, the latter is an effect which is not present in the NCEP/NCAR reanalysis.

In the North-Atlantic storm track region, structure and intensity has improved. Cyclone count has increased all over the storm track region from Cape Hatteras to the Norwegian and Barents Sea. Comparing the T85 control run with the NCEP/NCAR reanalysis, the maximum located southeast of Greenland in the NCEP/NCAR reanalysis have shifted somewhat southeast in the T85 reanalysis and the maximum over the Norwegian/Barents sea is missing. The cyclone count increase in the Norwegian and Barents sea improves the storm track structure with respect to the missing meridional tilt in the T42 control run, though the NCEP/NCAR reanalysis still comes off as more meridionally tilted.

Several features are seen to improve in response to increasing the horizontal resolution in CAM3, mostly tied to the North-Atlantic storm track and North-America. Still, the T85 control run and the NCEP/NCAR reanalysis are very different. The T85 control run fails to achieve as high cyclone counts in both storm track regions as the NCEP/NCAR reanalysis and overestimates the cyclone count over the Arctic Ocean, even though the horizontal resolution of the T85 control run exceeds that of the NCEP/NCAR reanalysis. This indicates that *horizontal resolution is not the main source of the differences between CAM3 and the NCEP/NCAR reanalysis*. Whether the differences are due to the extrapolation of the sea level pressure field or other internal differences between CAM3 and the NCEP global spectral model is beyond the scope of this project.

The TA2 NH run

Remember from section 3.1 and section 5.3 that the TA2 NH run is one of the modified

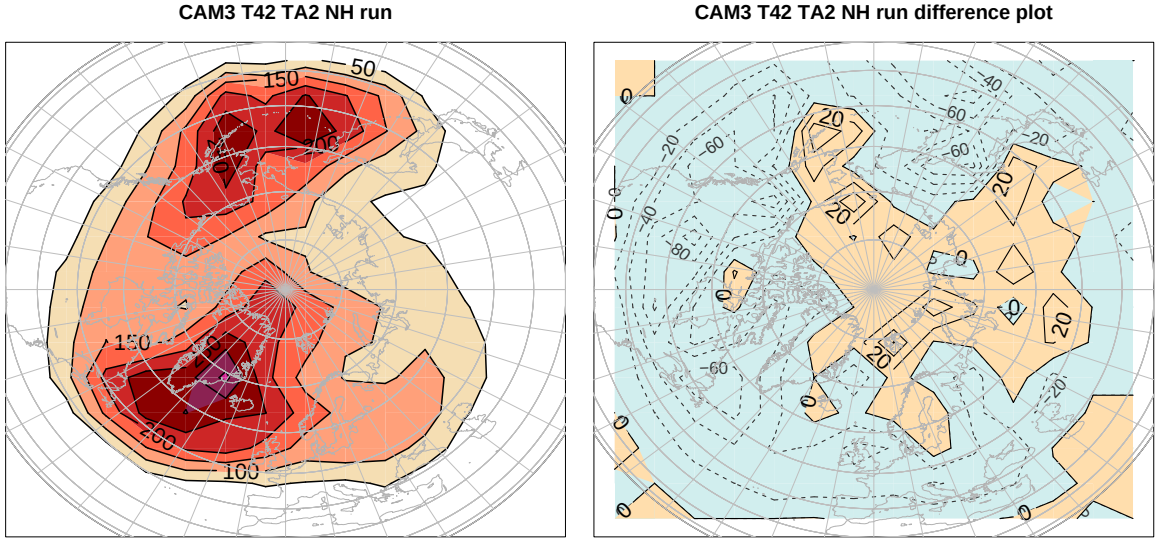

(a) (b)

Figure 5.23: *(a) and (b) show the total cyclone count field and the cyclone count difference field from the TA2 NH run, respectively. As in the previous sections of this chapter, difference plots are generated subtracting the total T42 control run cyclone count from the total cyclone count from the run the difference plot is made for. Otherwise as in Figure 5.21(a)*

T42 CAM3 runs in which a SST anomaly of 2 K was imposed at all oceanic grid points north of 45°S. The SST anomaly domain is shown in Figure 3.3(a) on page 35. In section 5.3 the North-Atlantic storm track was found to shift northeast in response to the oceanic warming while the Pacific storm track intensified slightly in terms of bandpass SLP. The changes seen in bandpass SLP in the storm track regions were consistent with the changes in bandpass $Z_{500\,\mathrm{hPa}}$, u and the Eady parameter.

Now, the response in the TA2 NH run from the imposed SST anomaly will be investigated in terms of the cyclone count difference field shown in Figure 5.23(b) and compared to the bandpass SLP difference field in Figure 5.9(b) on page 72.

Figure 5.23(b) displays a general reduction in cyclone count in both storm track regions and over North-America. The largest reduction sites are the Pacific and the North-Atlantic storm track entrance regions and Canada. The cyclone count is found to increase over the Arctic Ocean with maximum in the Barents Sea, Bering Sea and East Siberian Sea, and over Asia.

Some features in Figure 5.23(b) resemble Figure 5.9(b), such as the maximum northeast of Greenland, the maximum in the Bering Sea, positive values over the Arctic Ocean and Asia and negative values over North-America. In spite of these similarities, the major differences between the two figures are in the storm track regions and cannot be neglected. In the northwestern

Pacific, bandpass SLP display positive values while cyclone count yields a reduction and in the North-Atlantic exit region bandpass SLP and cyclone count difference field also show response of different signs.

Though the TA2 NH run cyclone count difference field resembles the bandpass SLP difference plot, the differences are harder to interpret. Local increases and decreases suggests that *cyclone count differences as a measure of change in storm track structure and intensity is less robust than bandpass variance. We believe this is so because the cyclone statistic is based on extreme events, and therefore the differences are less significant.* It is difficult to draw a conclusion on storm track changes in the TA2 NH run from the cyclone count difference plot.

Conclusions

In this section, results from the T42 control run, the NCEP/NCAR reanalysis, the T85 control run and the TA2 NH run was presented in terms of cyclone count from the CCI method. Findings are:

The CCI method: Applied to the NCEP/NCAR reanalysis, the CCI method yields two large maxima corresponding to the North-Atlantic and Pacific storm track regions with the North-Atlantic maximum being stronger, consistent with results from the bandpass method.

Compared to the storm track maxima in the bandpass variance fields, cyclone count maxima are shifted downstream and poleward. This reflects the fact that while the bandpass variance fields are dominated by growing baroclinic waves, the cyclone count fields are dominated by stronger and more mature cyclones.

The T42 control run: The T42 control run does not compare as well to the NCEP/NCAR reanalysis in terms of cyclone count as it did in terms of bandpass variance in section 5.1. Both magnitude and intensity of the cyclone count fields are very different. Southwest of Greenland, cyclone count is more than twice as large in the NCEP/NCAR reanalysis and in parts of the Norwegian Sea, cyclone count is four times as large. Differences are also large in the Pacific storm track region.

The North-Atlantic maximum does not display its characteristic northward tilt as the cyclone count is gravely underestimated in the storm track exit region. In the Pacific storm track exit region, cyclone count is too narrow in the meridional direction.

The T85 control run: Increasing the horizontal resolution improves the structure and intensity of the North-Atlantic maximum with respect to the T42 control run and the NCEP/NCAR reanalysis, but the T85 control run and the NCEP/NCAR reanalysis are still very different.

The Pacific maximum is very similar to the T42 control run in both structure and intensity.

Differences in horizontal resolution does not appear to be the main source of the inconsistencies between CAM3 and the NCEP/NCAR reanalysis. Finding the cause of these inconsistencies is beyond the scope of this project.

The TA2 NH run: The cyclone count difference plot resembles the bandpass SLP difference plot, but the same conclusions cannot be made. The differences are harder to interpret.

Large differences are seen between cyclone count structure and intensity between the T42 control run and the NCEP/NCAR reanalysis. The cyclone count field from CAM3 improves with respect to the NCEP/NCAR reanalysis in the North-Atlantic when increasing the horizontal resolution to T85, but differences are still large and the Pacific storm track was left almost unaltered.

The difference plots are hard to interpret. Indications are that cyclone counting is a less robust method than bandpass filtering in storm track sensitivity studies. Cyclone counting is believed to be less robust as it is based on extreme events, making differences less significant.

Chapter 6

Summary and discussion

This thesis presented results from an AGCM sensitivity study investigating the storm track response to increased SSTs. *The aim of this study was to investigate a potential northward shift in the North-Atlantic storm track in response to an imposed oceanic heating anomaly.* The project was motivated by observational studies cited in the IPCC Fourth Assessment Report (Trenberth et al., 2007) (e.g. McCabe et al. (2001), Gulev et al. (2001)) indicating a change in position and intensity of the Northern Hemisphere storm track during the last half of the 20th century which may be related to global warming. As the ocean warms in response to global warming (Trenberth et al., 2007), it is interesting to investigate the storm track response with oceanic heating as the only forcing.

To perform the necessary simulations, the NCAR CAM3 model was utilized. CAM3 was run with an Eulerian dynamical core, T42 and T85 resolution in the horizontal, 26 vertical levels and the Data Ocean Model (DOM). DOM was applied with 12 monthly prescribed SST and ice coverage field samples. Modifications to the SST and ice coverage fields were made in the initial condition data set files using the `change_sst` and `change_ice` functions in Appendix C and Appendix D.

The storm tracks were represented in terms of bandpass variance and cyclone count from the bandpass filter method (e.g Blackmon (1976) and Blackmon et al. (1977)) and the CCI method from Benestad and Chen (2006). The CCI method was applied to the 6 h SLP field and the bandpass filter method was applied to both the 6 h SLP field and the 6 h $Z_{500\,\mathrm{hPa}}$ field. The time period investigated was 1. December 198 – 28. February 1990 using the Northern Hemisphere winter months (DJF).

Results from seven CAM3 runs were investigated in this thesis including the high-resolution (T85) and low-resolution (T42) control run, four modified runs with the same 2 K SST anomaly imposed in four different geographical domains and one modified run in which the ice cover has been removed from the entire Northern Hemisphere. All the modified runs were run using T42 resolution in the horizontal. The T42 and T85 control runs were compared to corresponding data from the NCEP/NCAR reanalysis. The reanalysis data used in this project was taken from the NCEP/NCAR reanalysis 1, provided by the National Ocean & Atmosphere Administration (NOAA)/Outstanding Accomplishments in Research (OAR)/Earth System Research Laboratory (ESRL) Physical

Sciences Division (PSD), Boulder, Colorado, USA, from their Web site at `http://www.cdc.noaa.gov/`.

The control run: The bandpass filtered SLP field, the bandpass filtered $Z_{500\,\mathrm{hPa}}$ field, the Eady parameter field, the mean zonal velocity (u) field, the zonally averaged Eady parameter field and the zonally averaged u field from the T42 control run were investigated and compared to corresponding data from the NCEP/NCAR reanalysis for validation. Consistent with the findings of Blackmon (1976) and Blackmon et al. (1977), large maxima were found in both bandpass variance fields corresponding to the North-Atlantic and Pacific storm tracks, confirming that *the bandpass method is suited for storm track studies when applied to the SLP and $Z_{500\,\mathrm{hPa}}$ fields.* Maxima in u and the Eady parameter were found in approximately the same locations as the bandpass variance maxima in both storm track regions, confirming the strong relationship which exists between bandpass variance, atmospheric baroclinicity and the mean flow.

All the presented fields were seen to compare remarkably well to NCEP/NCAR reanalysis data. Issues were related to the bandpass SLP fields in regions of high topography, and the structure of the North-Atlantic maxima which was slightly too zonal in all fields investigated. *The general conclusion from the T42 control run was that CAM3 produce fields that closely resemble the NCEP/NCAR reanalysis and is therefore suited for storm track sensitivity studies.*

The high-resolution control run: It is argued by e.g. Lau (1997) that high resolution is instrumental to achieving an accurate response to mid-latitude and high-latitude SST anomalies in GCM sensitivity studies. To find out whether it is worth while to increase the horizontal resolution in CAM3 from T42 to T85, in spite of the dramatically prolonged run-time, the bandpass filtered SLP field, the bandpass filtered $Z_{500\,\mathrm{hPa}}$ field, the u field and the Eady parameter field from the T85 control run were compared to corresponding results form the T42 control run and NCEP/NCAR reanalysis. Results showed that the North-Atlantic maximum was generally worsened or unaltered, except in the exit region where increased values with respect to the T42 control run yielded *a more pronounced northward tilt in all fields*. The Pacific storm track was mostly improved except in the bandpass filtered SLP field. The topography related issues in the bandpass filtered SLP field worsened with increased resolution. The overall conclusion was that *T42 resolution is sufficient for sensitivity studies* as the fields did not exclusively improve and the prolonged run-time associated with performing all the modified runs in T85 resolution instead of T42 was dramatic and unrealistic within the short time span available for this project.

It is interesting to see that the structure of the North-Atlantic storm track improves with higher resolution. One can argue that this improvement could be very important when investigating changes in storm track location, as indications are that processes vital to the storm track structure in the North-Atlantic exit region are not properly resolved with T42 resolution. But even with T85 resolution, which is higher than the T68 resolution used in the NCEP/NCAR re-

analysis, the North-Atlantic storm track is still too zonal, indicating that the problem is not purely related to resolution. Black and Dole (2000) argue that GCMs lacking ability to accurately reproduce the meridional tilt of the North-Atlantic storm track might be related to a bias in the upper level deformation fields in the storm track exit region which is instrumental to storm track termination. These are issues which requires further investigation.

The fact that storm track amplitudes sometimes improve and sometimes worsen with respect to the NCEP/NCAR reanalysis with increased resolution is also an issue in need of further investigation

Warming the ocean by 2 K: In the T42 CAM3 TA2 NH run, the ocean was warmed by a realistic 2 K in all oceanic grid points north of 45°S. In response to the oceanic heating, the following changes were observed:

- The North-Atlantic storm track was seen to shift northeastward, while the Pacific storm track intensified without displaying a clear latitudinal shift.
- The changes in the North-Atlantic storm track region were similar in terms of bandpass $Z_{500\,\mathrm{hPa}}$, bandpass SLP, u and changes were seen in the Eady parameter corresponding to changes in bandpass variance in the storm track region.
- The Pacific storm track region was seen to shift northeastward along with the North-Atlantic storm track region in terms of u, while bandpass $Z_{500\,\mathrm{hPa}}$ did not yield an obvious shift, bandpass SLP yielded a downstream shift and changes in the Eady parameter corresponded well to changes in bandpass variance in the storm track region.
- The changes in diabatic heating were dominated by the latent heat flux.
- The meridional temperature gradient was seen to increase at high-levels and decrease at low-levels consistent with Yin (2005).
- The zonally averaged Eady parameter shifted upward and northward in response to changes in the meridional temperature gradient. These changes are consistent with results in Yin (2005).

Indications from these results are that the imposed SST anomaly yields increased diabatic heating, mainly associated with the latent heat flux, which alters the meridional temperature gradient. The latent heat flux increases the most in the tropics, which is also where the the meridional temperature gradient displays a strong high-level maximum. In response to the changes in the meridional temperature gradient, the zonally averaged Eady parameter shifts upward and poleward, a shift which is consistent with findings of Yin (2005).

The observed changes in the zonally averaged fields are consistent with the observed changes in the xy-plane, where changes in the mean circulation are seen corresponding to changes in the Eady parameter which in turn correspond to changes in bandpass variance. The exact mechanism by which heat is transported from the ocean surface to the atmosphere has not been properly investigated in this study, and is a topic ripe for further investigations.

Hoskins and Valdes (1990) argue that the Eady parameter is mainly maintained by local diabatic heating resulting from processes associated with the cyclones them selves. From this point of view the storm tracks are self-maintained, and one may argue that the observed changes in the Eady parameter at storm track latitudes could be caused by the actions of the cyclones themselves due to more available low-level heating. Further investigations are necessary to determine how much of the anomalous atmospheric heat transport is actually associated with the actions of the cyclones. Fields like $v'T'$ and $\omega'T'$ could be found by bandpass filtering the vT and ωT CAM3 fields and would doubtlessly yield much useful information about the atmospheric heat transport of the bandpass eddies.

Broccoli and Manabe (1992) on the other hand, argues that the storm track structure is maintained by the orographically induced stationary wave pattern. Branstator (1992) found that anomalies in the mean flow are caused by corresponding anomalies in the bandpassed eddie field, and Branstator (1995) found that anomalies in the mean flow cause corresponding anomalies in the bandpass eddie field. Storm track structure is obviously closely tied to the mean circulation, and any change in storm track structure is expected to be accompanied by a change in the mean circulation. This is consistent with what is observed in the TA2 NH run. As CAM3 is a nonlinear model including the two-way feedback processes established by Branstator (1992) and Branstator (1995) there is no way to separate these effects in this study. To what extent the storm track anomalies arise from mean flow anomalies, or the mean flow anomalies arise from storm track anomalies is impossible to determine. Further investigations with e.g. a linear model is necessary to assess the e.g. the effect of the storm track anomaly resulting from the imposed SST anomaly on the general circulation.

One of the main findings from the TA2 NH run, is that the observed changes in the zonally averaged temperature field and the zonally averaged Eady parameter are very similar to results in Yin (2005). As Yin (2005) performed a *climate scenario study* with 15 *coupled* GCMs in which the greenhouse gas concentrations had been increased in accordance with the A1B scenario from the IPCC Special Report on Emission Scenarios Nakicenovic et al. (2000), it is interesting that the results of Yin (2005) are consistent with findings from an *uncoupled* AGCM in which the only imposed change is a 2 K SST anomaly. *This indicates that ocean warming is the primary factor affecting the observed changes in Yin (2005).* This might also be true in observational storm track studies such as McCabe et al. (2001). McCabe et al. (2001) investigated trends in the second half of the 20th century using NCEP/NCAR reanalysis data and a feature point identification method. In terms of cyclone frequency, findings where an increase at high-latitudes (north of 60°N) and a decrease at lower latitudes (south of 60°N). The changes in winter cyclone frequency were significantly and positively correlated to changes with Northern Hemisphere winter temperature.

In the TA2 NH run, changes where seen in the North-Atlantic storm track region corresponding to a northeastward shift, while the Pacific storm track region did not yield a clear latitudinal shift. Several studies have claimed to observe northward shifts in the storm tracks. Yin (2005) reported a consistent northward shift in the zonally aver-

aged bandpass filtered eddie kinetic energy field, relative to the contours from the control run. This is similar to the approach of this study. McCabe et al. (2001) divided the Northern Hemisphere into two boxes, one north of 60°N and one south of 60°N and found the cyclone count to decrease in the low-latitude box while it increased in the high-latitude box and interpreted this as a northward shift. Wang et al. (2006) defines a mean storm track position and finds that it has shifted north during the second half of the 20th century. Different studies use difference indices of cyclone activity (e.g. bandpass variance, cyclone count, trajectory count). As commented by Paciorek et al. (2002), there is a widespread need for different cyclone activity indices as cyclones are complex features and whose changes may be associated with frequency, intensity, life times or location and the different measures are needed to capture the different aspects. But the use of various indices make results from different studies hard to compare, and the comparison is made even more difficult by the fact that there is no common definition of what a northward shift really is. E.g, is it necessarily true that the North-Atlantic and Pacific storm tracks will shift north because the zonally averaged bandpass filtered eddy kinetic energy does as was seen in Yin (2005)? How does this compare to a northward shift in the mean storm track position as was found in Wang et al. (2006)? There is an obvious need of a common way of defining what a northward shift should involve in terms of cyclone count, bandpass variance, cyclone trajectory count etc., e.g. a way of defining a storm track axis and assessing the meridional shift of this axis in the xy-plane in response to trends in the reanalysis data or imposed forcings in GCM studies.

SST sensitivity: To investigate longitudinal and latitudinal dependence to oceanic warming, the SST anomaly domain from the TA2 NH run was divided into three sub-domains which all excluded the Pacific ocean, one including the Atlantic and Arctic Ocean (high-latitudes and low-latitudes), one including low-latitudes in the Atlantic, and one including high-latitudes in the Atlantic and the Arctic Ocean. The same 2 K SST anomaly was imposed in all domains. From this, the response to longitudinal and latitudinal variations in oceanic heating were investigated revealing that:

- When excluding the Pacific from the SST anomaly domain and heating low-latitudes and high-latitudes in the Atlantic and Arctic, latent heating increases at low-latitudes (south of 40°N) in the Atlantic and decreases at similar latitudes in the Pacific. These changes are accompanied by similar changes in bandpass activity, u and the Eady parameter again confirming the strong relationship between these fields.
- The response in latent heating from warming both high-latitudes and low latitudes can be quite accurately reproduced by only heating low-latitudes.
- Heating high-latitudes only yields a very weak response in comparison to heating all latitudes or just low-latitudes.

Findings from the SST sensitivity study show that changes in bandpass $Z_{500\,\mathrm{hPa}}$, the Eady parameter, u and latent heating primarily happen in response to the low-latitude SST anomalies. The diabatic heating response caused by the imposed oceanic warming is dominated by latent heating

which in turn affects the bandpass variance, atmospheric baroclinicity and mean circulation in a consistent manner. By which mechanisms the energy is transferred from the ocean surface to the atmosphere is, as previously mentioned, a topic ripe for further investigations. It can nevertheless be concluded that *oceanic heating at latitudes south of 40°N is the main driver of the observed atmospheric changes*.

Removing the ice cover: Having established low-latitude heating as the main contributor to the observed atmospheric changes in bandpass variance, atmospheric baroclinicity and the mean circulation, indications are that high-latitude heating is not important. From this, one may question whether the same is true for a reduction in the ice cover at high-latitudes. This is a prominent issue as according to the IPCC Fourth Assessment Report (Trenberth et al., 2007), the ice cover is shrinking. To answer this question, the CAM3 ice cover was removed from the entire Northern Hemisphere in the no ice run. Findings where that:

- Changes in the storm tracks are of comparable magnitudes as those resulting from high-latitude heating, but structures are different. This indicates that high-latitude heating resulting from SST anomalies and removing the ice cover are of similar importance to storm tracks changes.
- A local increase in diabatic heating is seen in the Arctic where the ice cover had been removed. In response to this, the zonally averaged Eady parameter was seen to increase at low-levels due to the contribution from the Brunt-Väisälä frequency.

Having concluded that low-latitude heating is the main contributor to the observed atmospheric changes, and having seen that removing the entire sea ice coverage yields changes of comparable magnitudes to high-latitude heating, *indications are that removing the ice cover is not important compared to low-latitude heating in the fields investigated in this study*.

Removing the ice cover did yield local changes in the Arctic associated with the Brunt-Väisälä frequency. This might ultimately bring on changes in atmospheric fields not investigated in this study.

Cyclone counting: As mentioned, cyclone count is another measure commonly applied in storm track studies (e.g. McCabe et al. (2001), Benestad and Chen (2006)). To investigate the storm tracks and the response to a 2 K oceanic warming in terms of cyclone count in addition to bandpass variance, the CCI method from Benestad and Chen (2006) was applied to the T42 control run, the NCEP/NCAR reanalysis, the T85 control run and the TA2 NH run. The total cyclone count from the entire time period was taken to be all identified low-pressure centers stronger than the threshold value[1] north of 30°N.

- The CCI methods yields two regions of large cyclone count values in the North-Atlantic and Pacific corresponding to the North-Atlantic and Pacific storm

[1]The threshold field was chosen to be the maximum gradient wind, and the threshold value was 15 m/s.

tracks, with the North-Atlantic storm track being stronger than the Pacific storm track. Cyclone count maxima are shifted downstream and poleward compared to bandpass variance maxima, reflecting the fact that bandpass variance is dominated by baroclinic waves while cyclone count is dominated by stronger and more mature features.

- The T42 control run does not relate as well to the NCEP/NCAR reanalysis in terms of cyclone count as it did in terms of bandpass variance, both in structure and magnitude. Differences larger than 100% are found in both storm track regions.

- Increasing the horizontal resolution in CAM3 improved the North-Atlantic storm track in terms of both magnitude and structure with respect to the NCEP/NCAR reanalysis, but the Pacific storm track was almost unchanged.

- In response to the 2 K oceanic warming in the TA2 NH run, the cyclone count difference field from the TA2 NH run was seen to bear similarities to the bandpass SLP field, but cyclone count differences were more difficult to interpret.

In terms of cyclone count, CAM3 did not manage to successfully capture the structure and magnitude of the NCEP/NCAR reanalysis storm track regions. Increasing the horizontal resolution from T42 to T85 improved the North-Atlantic storm track in terms of magnitude and structure, yielding an improved northward tilt. Still, differences between the T85 control run and the NCEP/NCAR reanalysis are large and it is strange that only the North-Atlantic storm track improved in response to the increased resolution. Indications are that the differences between CAM3 and the NCEP/NCAR reanalysis are not merely related to resolution, particularly since the T85 control run was run with higher horizontal resolution than the NCEP/NCAR reanalysis. Assessment of the cause and importance of the differences between CAM3 and the NCEP/NCAR reanalysis should be carried out before storm track sensitivity studies with the CCI method and CAM3 can be properly interpreted.

The cyclone count difference plot from the TA2 NH run bared some resemblance to the bandpass variance difference plots, but displayed strange increases and decreases making interpretation difficult. Cyclone counting is based on extreme events, thus differences may be less significant. Also, the structure and magnitude of the difference field varies strongly dependent on choice of threshold field (minimum pressure, maximum pressure gradient, wind speed) and threshold value as well as the number of boxes/bins[2] in the plotting domain. *As a measure of changes in storm track structure and intensity, cyclone counting is therefore believed to be less robust than bandpass filtering.*

[2]Cyclone count plots were made by dividing the plotting domain into a certain number of boxes/bins, counting the number of feature points identified within each box and making stereographic contour plots.

Chapter 7

Future work

Heat transport by baroclinic eddies: To determine how oceanic warming alters the meridional temperature gradient through bandpass eddies, the 6 h vT and 6 h ωT fields should be bandpass filtered in all three spatial dimensions using the same bandpass filter settings as was applied to the 6 h SLP field and 6 h $Z_{500\,\mathrm{hPa}}$ field in this study.

Eddie forcing on the mean flow: The E-vector field ($\overline{u'v'}, \overline{v'^2 - u'^2}$) was introduced by Hoskins (1983) and applied by e.g. Hoskins and Valdes (1990) and Orlanski (1998). According to Hoskins and Valdes (1990), the divergence of the E-vectors in the storm track region indicates the tendency of the eddy field to force the mean flow. Applying bandpass filtering to the CAM3 6 h u and 6 h v fields and plotting the E-vectors will provide useful information about how the bandpass eddies force the mean flow.

Three-dimensional bandpass variance: The three-dimensional CAM3 6 h geopotential height field can be bandpass filtered to yield a proper three-dimensional picture of the storm tracks and the response to the 2 K oceanic warming. In particular, a zonal average plot should be made to determine whether the bandpass variance field shifts upward and northward in response to the oceanic warming in the TA2 NH run as was observed in the zonally averaged Eady parameter field. This is also interesting because Yin (2005) found a northward and upward shift in both the Eady parameter and the bandpass variance field. Notice that even though Yin (2005) applied the bandpass filter to the eddy kinetic energy field, a similar shift should be seen in the bandpass filtered geopotential height field.

SST sensitivity: To assess the sensitivity to high-latitude and low-latitude SST anomalies in the TA2 NH run, two more modified runs should be conducted which *includes all longitudes*: a low-latitude heating run where an SST anomaly of 2 K is imposed in all oceanic grid points between 45°S and 45°N, and a high-latitude heating run where a corresponding 2 K SST anomaly is added to all oceanic grid points north of 45°N. Notice that the low-latitude heating run is similar to the TML2 run investigated in this thesis, only including the Pacific. A similar relationship is seen between the new high-latitude heating run and the AA2 run investigated in this thesis. *The results from the new runs will hopefully*

confirm that the TA2 NH run is dominated by the low-latitude heating as was seen to be the case in the TA2 run in this thesis.

Feature point tracking: Important aspects of the storm track response to the imposed oceanic heating cannot be determined from an Eulerian framework. Changes in the individual cyclone trajectories will reveal whether the oceanic warming yields alterations in traveling cites, e.g. will more cyclones be "drawn" into the Norwegian and Barents Sea? A feature point tracking method will yield information about where each individual cyclone is formed and where it dies, making it possible to investigate whether the oceanic warming changes the preferred sites of cyclogenesis and cyclosis. It would also be interesting to compare cyclogenesis density plots to Eady parameter plots to see to how they relate to each other.

It would be preferable to apply a feature point tracking routine to the vorticity field as have been done in e.g. Hoskins and Hodges (2002) and Orsolini and Sorteberg (2009). By tracking vortices rather than low-pressure centers one will avoid problems related to the strong influence of the background flow and the features such as the Icelandic low in the SLP field (Hoskins and Hodges, 2002). Also, as the vorticity field allows one to focus one smaller scales, cyclones can be identified earlier in their life cycle (Hoskins and Hodges, 2002).

Appendices

Appendix A

Abbreviations

AGCM	Atmospheric General Circulation Model
APE	Available Potential Energy
CAM3	Community Atmosphere Model version 3.0
CCI	Calclulus-based Cyclone Identification
CCSM	Community Climate System Model
CLM	Community Land Model (a part of CAM3)
DJF	December, January, and February
ECMWF	European Center for Medium Range Weather Forecast
ERA40	The 40 year ECMWF Reanalysis
GCM	General Circulation Model
IPCC	Intergovernmental Panel on Climate Change
JJA	June, July, and August
NCAR	National Center for Atmospheric Research
NCEP	National Center for Environmental Prediction
RMS	Root Mean Square
SLP	Sea Level Pressure
SST	Sea Surface Temperature
T42	Fourier series in Spectral method is truncated after 42 terms
T85	Fourier series in Spectral method is truncated after 85 terms

Appendix B

The Eady model of baroclinic growth

The Eady model is a baroclinic instability model with constant stratification and no β-effect. Several models of baroclinic instability have been made through the years. Different models include different processes and complexity. The Eady model is perhaps the simplest one, but it still manages to capture many of the observed features and provides lots and lots of useful insight.

This review of the Eady model approximately follows Vallis (2005).

Assumptions

f-plane approximation This is the β-plane approximation with $\beta = 0$. Thus the Coriolis parameter is constant throughout the domain ($f = f_0$) and does not contribute to the vorticity, there is no planetary vorticity in the Eady model. This greatly simplifies things, but is considered the major drawback of the model as the real atmosphere does indeed have planetary vorticity.

Constant Brunt-Viäsälä frequency That is, the atmosphere is uniformly stratified. This reflects the stratification of the atmosphere and is a reasonable approximation when concerned with the troposphere.

Two rigid lids The upper and lower boundary are assumed to be two flat rigid horizontal surfaces. For the lower boundary this is equivalent to assuming no topography. Taking the upper boundary to be a rigid lid is perhaps slightly more suspicious. When the boundaries are represented by two horizontal lids they do not generate any vertical velocities.

Constant vertical wind shear The wind shear is given by $\bar{u} = \Lambda z \Rightarrow \frac{\partial \bar{u}}{\partial z} = \Lambda$ where

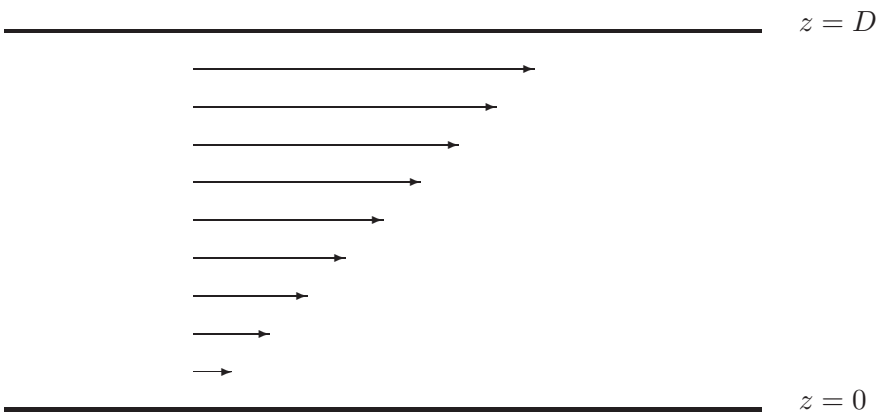

Figure B.1: *The figure illustrates some of the assumptions of the Eady model. The two thick lines are the rigid lids at $z = 0$ and $z = D$ and the linearly increasing wind shear is illustrated by the arrows.*

Λ =Constant. Due to this assumption the Eady model satisfies the fourth Charney-Stern criteria for baroclinic instability, namely that the vertical wind shear has the same sign on the upper and lower boundary.

Linearization

As is common procedure, take the quasi-geostrophic potential vorticity equation (GQPV equation) for the interior of the fluid and the quasi-geostrophic temperature equation for the boundaries. The full adiabatic QGPV equation is:

$$\frac{D_g}{dt}\left[\nabla^2\psi + \beta y + \frac{\partial}{\partial z}(\frac{f_0^2}{N^2}\frac{\partial}{\partial z}\psi)\right] = 0 \tag{B.1}$$

where material derivative following the geostrophic wind is defined as

$$\frac{D_g}{dt} = \frac{\partial}{\partial t} + u_g\frac{\partial}{\partial x} + v_g\frac{\partial}{\partial y} \tag{B.2}$$

and ψ is the streamfunction defined as

$$u_g = -\frac{\partial}{\partial y}\psi, \qquad v_g = \frac{\partial}{\partial x}\psi \tag{B.3}$$

From equation (B.3) it follows that the geostrophic relative vorticity ζ_g is:

$$\begin{aligned} \zeta_g &= \frac{\partial}{\partial x} v_g - \frac{\partial}{\partial y} u_g && \text{(B.4)} \\ &= \frac{\partial}{\partial x}(\frac{\partial}{\partial x}\psi) - \frac{\partial}{\partial y}(-\frac{\partial}{\partial y}\psi) && \text{(B.5)} \\ &= \nabla^2 \psi && \text{(B.6)} \end{aligned}$$

Equation (B.1) is a non-linear equation due to the advection terms. To make further investigations of the equation as painless as possible it's wise to linearize the equation. Linearization of such equations is done in the following way:

1. Assume that the velocities may be written as a sum of two parts:

$$u_g = \bar{u} + u', \qquad v_g = \bar{v} + v' \tag{B.7}$$

   where $\bar{u}$ and $\bar{v}$ are the mean velocities and constitute the mean flow. The primed quantities u' and v' and deviations from the mean and *small* such that $\bar{u}, \bar{v} >> u', v'$. In the atmosphere at mid-latitudes $\bar{v}$ is generally taken to be zero, and this is also the case in the Eady model. From the assumptions of the Eady model it is known that $\bar{u} = \Lambda z$. Thus $\bar{u}$ is a function of z only!

$$\begin{aligned} \bar{u} &= \bar{u}(z) \\ \bar{v} &= 0 \\ u' &= u'(x, y, z, t) \\ v' &= v'(x, y, z, t) \end{aligned}$$

2. Insert expressions from equation (B.7) into the equation about to be linearized.

3. Neglect terms that are products of primed quantities as these are very small compared to the remaining terms.

Due to equation (B.7), the streamfunction may be written in a similar way:

$$\psi = \bar{\psi} + \psi' \tag{B.8}$$

where $\bar{\psi}$ and ψ' are connected to the mean and perturbed velocities through equation

(B.3).

$$\begin{aligned} \frac{\partial}{\partial y}\bar{\psi} &= -\bar{u} \\ \frac{\partial}{\partial y}\bar{\psi} &= -\Lambda z \\ \int \frac{\partial}{\partial y}\bar{\psi} d\, y &= \int -\Lambda z d\, y \\ \bar{\psi} &= \Lambda z y + const. \end{aligned}$$

ψ' is a function of all dimensions. Consequently:

$$\psi(x, y, z, t) = \bar{\psi}(y, z) + \psi'(x, y, z, t) \tag{B.9}$$

Now, apply this to linearize equation (B.1). Insert equation (B.7) into equation (B.1) and use that N^2 =Constant and that $\beta = 0$. Keep in mind that from equation (B.9) $\nabla^2\psi = \nabla^2\bar{\psi}(y, z) + \nabla^2\psi'(x, y, z, t)$ and $\frac{\partial^2}{\partial z^2}\psi = \frac{\partial^2}{\partial z^2}\bar{\psi}(y, z) + \frac{\partial^2}{\partial z^2}\psi'(x, y, z, t)$. But since $\bar{\psi} = \Lambda z y + const.$ both $\bar{\psi}$ terms in the above equation go away! *The background flow does not have any vorticity.* This yields: $\nabla^2\bar{\psi}(y, z) = 0$, $\frac{\partial^2}{\partial z^2}\bar{\psi}(y, z) = 0$ $\nabla^2\psi = \nabla^2\psi'(x, y, z, t)$, $\frac{\partial^2}{\partial z^2}\psi = \frac{\partial^2}{\partial z^2}\psi'(x, y, z, t)$. The linearized QGPV equation is:

$$(\frac{\partial}{\partial t} + \bar{u}\frac{\partial}{\partial x}) \left[\nabla^2\psi' + \frac{f_0^2}{N^2}\frac{\partial^2}{\partial z^2}\psi'\right] = 0$$

Now, appy the quasi-geostrophic temperature equation at the boundaries. The full adiabatic version is:

$$\frac{D_g}{dt}\frac{\partial}{\partial z}\psi\Big|_{z=0,D} + \frac{N^2}{f_0}w\Big|_{z=0,D} = 0$$

Because of the rigid lid approximation, there is no vertical velocity at either boundary. Vertical velocities are generated from topography and Ekman layers at the boundaries, and the rigid lid approximation has neither. This yields:

$$\frac{D_g}{dt}\frac{\partial}{\partial z}\psi\Big|_{z=0,D} = 0$$

Linearize this equation as before and utilize that $\bar{\psi} = \Lambda z y + \text{Constant}$. Thus: $\frac{\partial}{\partial y}\frac{\partial}{\partial z}\bar{\psi} = \frac{\partial}{\partial y}\frac{\partial}{\partial z}\Lambda z y + const. = \frac{\partial}{\partial y}\Lambda y = \Lambda$

The *linearized temperature equation* written with v' in terms of the streamfunction is:

$$(\frac{\partial}{\partial t} + \bar{u}\frac{\partial}{\partial x})\frac{\partial}{\partial z}\psi'\Big|_{z=0,D} + v'\Lambda\Big|_{z=0,D} = 0$$

So, the Eady equations are:

The Eady Model 1 *linearized QGPV equation*

$$(\frac{\partial}{\partial t} + \bar{u}\frac{\partial}{\partial x})\left[\nabla^2\psi' + \frac{f_0^2}{N^2}\frac{\partial^2}{\partial z^2}\psi'\right] = 0 \tag{B.10}$$

The Eady Model 2 *linearized QG temperature equation*

$$(\frac{\partial}{\partial t} + \bar{u}\frac{\partial}{\partial x})\frac{\partial}{\partial z}\psi'\Big|_{z=0,D} + \frac{\partial}{\partial x}\psi'\Lambda\Big|_{z=0,D} = 0 \tag{B.11}$$

Wave solutions

Assume that the streamfunction is well represented by a single Fourier component which varies sinusoidally in x, y and t:

$$\psi' \sim \mathrm{Re}\{e^{ik(x-ct)+ily}\} \tag{B.12}$$

where l is the meridional wave number, k is the zonal wave number and c is the phase speed. Notice that both the amplitude and the phase speed may be complex.

Now, impose a second boundary condition on the solution. Assume that the horizontal plane is confined to a channel with two meridional walls at $y = 0$ and $y = L$. Demand that the streamfunction ψ be zero at both meridional walls:
$\psi(x, y = 0, z, t) = \psi(x, y = L, x, t) = 0$. To satisfy this boundary condition use a streamfunction of the form:

$$\psi' = \mathrm{Re}\{\hat{\psi}(z)\sin(ly)e^{ik(x-ct)}\} \tag{B.13}$$

where $\hat{\psi}(z)$ is the amplitude. This expression automatically satisfies the second boundary condition. The meridional wave number is now quantized: $l = \frac{n\pi}{L}$, $n = 1, 2, 3\ldots$. From now on it's understood that only the real part of equation (B.13) is used and the Re notation will be omitted.

The streamfunction is proportional to e^{-ikct}, so if the solution is to be unstable, that is grow exponentially in time, the imaginary part of the phase speed has to be greater than zero. A complex phase speed may be written as $c = c_r + ic_i$ where c_r is the real part and and c_i is the imaginary part. Then the wave solution is:

$$\psi = \hat{\psi}(z)\cos(ly)e^{kc_it}e^{ik(x-c_rt)}$$

When the phase speed has a positive imaginary part, the wave grows exponentially in time and is unstable.

Inserting equation (B.13) into equation (B.10) yields:

$$(\bar{u} - c)\left[(-k^2 - l^2)\hat{\psi} + \frac{f_0^2}{N^2}\frac{\partial^2}{\partial z^2}\hat{\psi}\right] = 0$$

The equation is satisfied when:

1. $\bar{u} = c$: the phase speed equals the mean flow which is real. In this case the phase speed has no imaginary part, consequently there is no exponential growth and the wave is stable.
2. $\frac{\partial^2}{\partial z^2}\hat{\psi} - \frac{N^2(k^2+l^2)}{f_0^2}\hat{\psi} = 0$: from equation (B.10) in this case *the interior QGPV is zero*. As the QGPV of the Eady model is conserved, this means that it must be zero everywhere at all times. The phase speed is allowed to be complex and there may be unstable solutions. But since the QGPV of the interior is conserved, the instabilities must arise at the boundaries.

Now, look further into the second solution:

$$\frac{\partial^2}{\partial z^2}\hat{\psi} - \alpha^2\hat{\psi} = 0, \qquad \alpha^2 \equiv \frac{N^2(k^2 + l^2)}{f_0^2} \tag{B.14}$$

This is a second order homogeneous ODE. Obviously $\alpha^2 > 0$ and the characteristic equation has real roots. Such equations have exponentials as solution. Alternatively the solution may be written in terms of hyperbolic functions. The latter is commonly preferred yielding the solution to be:

$$\hat{\psi} = A\sinh(\alpha z) + B\cosh(\alpha z) \tag{B.15}$$

where A and B are constants.

Now, insert equation (B.13) into equation (B.14) and substitute Λz for $\bar{u}$.

$$(-c + \Lambda z)\frac{\partial}{\partial z}\hat{\psi}\Big|_{z=0,D} - \hat{\psi}\Lambda\Big|_{z=0,D} = 0$$

Inserting the expression for $\hat{\psi}$ from equation (B.15) yields two solutions, one for each boundary. At $z = 0$:

$$-cA\alpha - \Lambda B = 0 \tag{B.16}$$

At $z = D$:

$$\begin{aligned}(\Lambda D - c)\left[A\alpha\cosh(\alpha D) + B\alpha\sinh(\alpha D)\right] - \\ \Lambda\left[A\sinh(\alpha D) + B\cosh(\alpha D)\right] = \quad 0\end{aligned} \tag{B.17}$$

It's known from linear algebra that for equations (B.16) and (B.17) to have a non-trivial solution, the determinant must equal zero. For this to be satisfied the phase speed must be given by:

$$c \quad = \quad \frac{\Lambda D}{2} \pm \frac{\Lambda}{\alpha}\sqrt{(\frac{\alpha D}{2} - \coth(\frac{\alpha D}{2}))(\frac{\alpha D}{2} - \tanh(\frac{\alpha D}{2}))} \tag{B.18}$$

This is the dispersion relation. It's possible to show that $\frac{\alpha D}{2} > \coth(\frac{\alpha D}{2}),\ \forall x$. Consequently it's the sign of $\frac{\alpha D}{2} - \tanh(\frac{\alpha D}{2})$ which decides whether c has an imaginary part or not. There are two possibilities:

Real roots $\frac{\alpha D}{2} > \tanh(\frac{\alpha D}{2})$ such that the roots of equation (B.18) are real. As the phase speed has no imaginary part there is no baroclinic instability.

Imaginary roots $\frac{\alpha D}{2} < \tanh(\frac{\alpha D}{2})$ such that the roots are imaginary. Thus in this case there might be unstable growth if $c_i > 0$.

Continue to pursue the imaginary roots case as it holds baroclinic instability. The phase speed is now given by: $c = c_r + ic_i$, where $c_r = \frac{\Lambda D}{2}$ and
$c_i = \frac{\Lambda}{\alpha}\left[(\coth(\frac{\alpha D}{2} - \frac{\alpha D}{2}))(\frac{\alpha D}{2} - \tanh(\frac{\alpha D}{2}))\right]^{\frac{1}{2}}$. The wave solution is as before
$\psi = \hat{\psi}(z)\cos(ly)e^{kc_i t}e^{ik(x-c_r t)}$ where kc_i is the growth rate given by:

$$kc_i = \frac{k\Lambda}{\alpha}\sqrt{(\coth(\frac{\alpha D}{2}) - \frac{\alpha D}{2}))(\frac{\alpha D}{2} - \tanh(\frac{\alpha D}{2}))} \tag{B.19}$$

Figure B.2 shows the Eady growth rate as a function of the zonal wave number using typical atmospheric values for N, f_0, Λ, D and L:

$$N = 0.01\,\mathrm{s}^{-1},\ f_0 = 10^{-4}\,\mathrm{s}^{-1},\ \Lambda = 0.005\,\mathrm{s}^{-1},\ D = 10^4\,\mathrm{m},\ L = 2\times 10^6\,\mathrm{m}$$

Notice from figure B.2 that the growth rate peaks at $k_{peak} = 1.25 \times 10^{-6}$. Abruptly after reaching peak value, the curve falls to zero at the short wave cut-off. Waves with wavenumbers larger than this value have purely real phase speeds and are too small to interact with each other and are stable. The peak value of the zonal wavenumber k_{peak} corresponds to a wavelength of $\lambda_{peak} = \frac{2\pi}{k_{peak}} \approx 5027\,\mathrm{km}$ making the trough-crest distance about 1257 km. This fits well with the spatial scales mid-latitude cyclones are known to

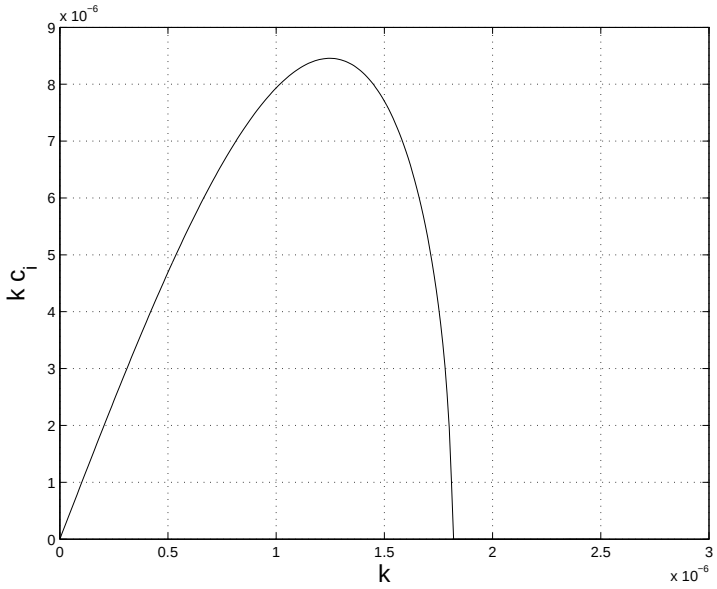

Figure B.2: *The Eady growth rate as a function of the zonal wavenumber. The following values were used:* $N = 0.01\ s^{-1}$, $f_0 = 10^{-4}\ s^{-1}$, $\Lambda = 0.005\ s^{-1}$, $D = 10^4\ m$, $L = 2 \times 10^6\ m$.

have. The growth rate in the figure peaks at about $8.456 \times 10^{-6}\,\mathrm{s}^{-1}$ corresponding to about 0.73/day, a good match to the known growth rate of mid-latitude cyclones.

Using equation (B.16) it's possible to write the expression for the streamfunction as

$$\psi = A\left[\cosh(\alpha z) - \frac{\Lambda}{c\alpha}\sinh(\alpha z)\right]\sin(ly)e^{ik(x-ct)}$$

Notice c in the denominator of the second term in the brackets. As c is complex the expression may be written as:

$$\psi = A\phi(z)\sin[ly + \gamma(z)]e^{ik(x-ct)}$$

where

$$\begin{aligned}
\phi(z) &= \sqrt{\left(\cosh(\alpha z) - \frac{c_r\Lambda}{|c|^2\alpha}\sinh(\alpha z)\right)^2 + \left(\frac{c_i\Lambda}{|c|^2\alpha}\sinh(\alpha z)\right)^2} \\
\gamma(z) &= \arctan\left(\frac{\frac{c_i\Lambda}{|c|^2\alpha}\sinh(\alpha z)}{\cosh(\alpha z) - \frac{c_r\Lambda}{|c|^2\alpha}\sinh(\alpha z)}\right)
\end{aligned}$$

Notice in particular that the complex part of the phase speed causes a phase shift in the streamfunction. The top figure in the left column of figure (B.3) shows the streamfunction

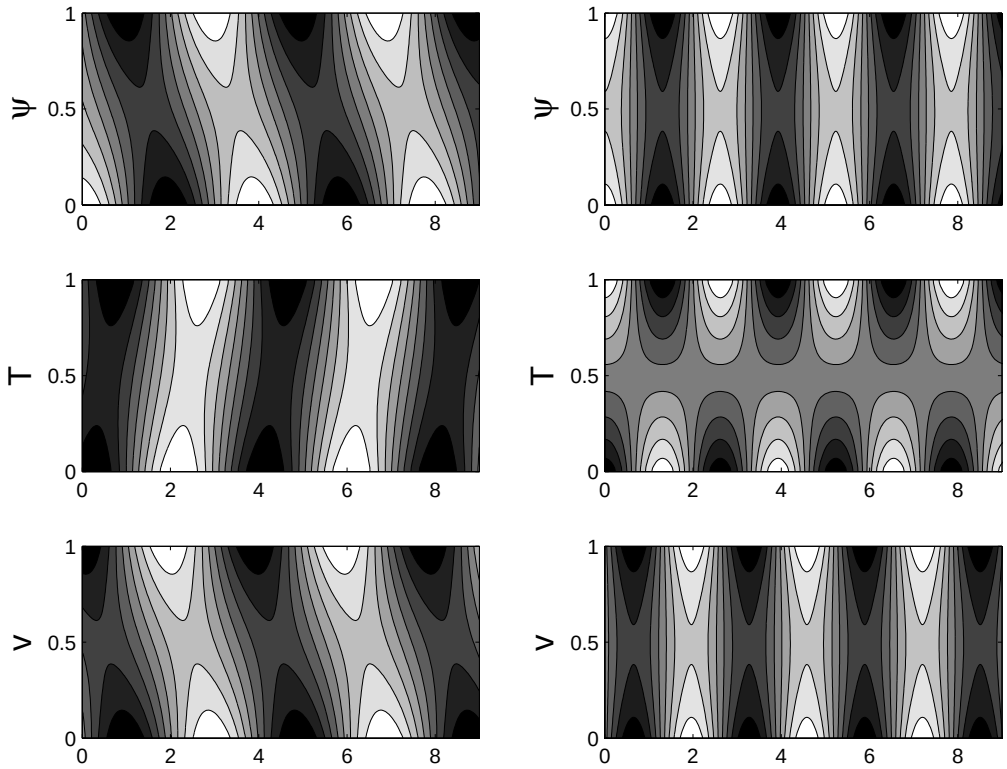

Figure B.3: *Left column: coupled Eady wave for the most unstable zonal wave number. Right coulumn: Eady wave for a zonal wave number greater than the short wave cut-off. The top figures shows the vertical structure of the streamfunction, the middle figures shows the vertical structure of the meridional velocity and the bottom figures shows the vertical structure of the temperature. Values used in the making of this plot are:* $N = f_0 = \Lambda = D = 1,\ L = 2 \times 10^6\,\mathrm{m}$. *The plot is non-dimentional. Using these values the most unstable wavenumber is* $k = 1.606$ *and this value has been used to generate the figures in the left column. The figures in the right column where generated using* $k = 2.4$. *Contour interval is 0.2 with values ranging from -1 (black contour filling) to 1 (white contour filling).*

for the zonal wavenumber of maximum growth k_{peak}. It can be seen from this figure that the amplitudes are greatest at the boundaries decaying into the interior. The amplitude of the disturbances does not go to zero anywhere in the interior in this case, allowing the disturbances on the boundaries to interact. The figure also clearly illustrates the tilt of the disturbances in the vertical, an instrumental property for the meridional heat transport. *The disturbances are tilted against the shear*.

The middle figure in the left column of figure (B.3) shows the temperature and the bottom figure shows the meridional velocity of the perturbations. The products of these quantities constitute the meridional heat transport. The figure shows that the meridional velocity is northwards where the temperature perturbations are positive. Similarly, the meridional velocity is southwards where the temperature perturbations

are negative. Thus the wave transports warm air towards the pole and cold air towards equator reducing the equator-to-pole meridional temperature gradient.

The right column of figure (B.3) shows the same three figures as the left, only with a zonal wavenumber chosen to be slightly above the short wave cut-off. Now the phase speed is purely real and the top figure shows that the perturbations does not tilt in the vertical. The middle figure shows that the temperature perturbations now decay too rapidly into the interior to interact. There is no meridional heat transport in this case.

The Eady model illustrates baroclinic growth of a single Fourier component. As the model does not have non-linear terms, the mechanisms responsible for the decay processes of baroclinic waves are not present in the model. As time increases, the waves will grow infinitely large. Still, the model illustrates important aspects of baroclinic wave growth.

Appendix C

The change_sst function

This appendix yields the source code of the R program which has been applied to change the SSTs in the CAM3 modified runs. This program was made using the R environment developed by R Development Core Team (2008) and the R-package `NCDF` (Pierce, 2006). Both the R environment and the `NCDF` package are freely available from `http://www.R-project.org`.

```
1  ######################################################################
2  # This program changes the sea surface temperatur (SST) of the
3  # climatological input file used in the data ocean model (DOM) in
4  # CAM3. The data ocean model reads and interpolates the SST data. The
5  # data set monthly samples for one year.
6  #
7  # This program changes the SST by a SCALAR!
8  #
9  # The program allows for the user to specify specific regions for
10 # which the SST is changed by a scalar for all monthly samples. The
11 # region is a square defined by lon.rng[start_lon,stop_lon] and
12 # lat.rng[start_lat,stop_lat]
13 #
14 # OPS! defining a area like the one given by the user in lon.rng and
15 # lat.rng results in a discontinuity at the boundary when changing the
16 # SST within the domain by a given scalar. This must be dealt with!
17 #
18 # Temperature is changed by a user given scalar dsst. The change in
19 # temperature (dsst) must be relaxed towards 0 as one approaches
20 # boundaries.  The relaxation interval is dlat and dlon in latitude
21 # and longitude direction.
22 #
23 # The relaxation area will typically be a area of say 3-5 degrees..?
24 #
25 # Solution may be relaxed along four "sides"
26 # 1. Along lat.rng[1]
```

```
27 # 2. Along lon.rng[2]
28 # 3. Along lat.rng[3]
29 # 4. Along lon.rng[1]
30 #
31 # Imagine a square, this means that the solution may be relaxed along:
32 # the bottom (1), the right side (2), the top (3) and the left side
33 # (4)
34 #
35 # Which boundaries there will be relaxation along is user given in the
36 # following way
37 #
38 # relax.bound <- c(b1=TRUE,b2=TRUE,b3=TRUE,b4=TRUE) The above example
39 # yields relaxation along all boundaries!
40 #
41 ######################################################################
42
43
44 # The function find.lon deals with the following problem: the start
45 # and stop latitude given by the user to define the domain of change
46 # will probably not coincide with a gripoint in the model. The
47 # function located the gridpoint which is closest to the user
48 # specified longitude.
49
50 find.lon <- function(lon,lon.rng) {
51
52   start_lon <- NULL
53   stop_lon <- NULL
54   n_start <- NULL
55   n_stop <- NULL
56
57
58   for (i in 1:length(lon)) {
59
60      if ((lon.rng[1] == lon[1])) {
61        start_lon <- lon[1]#;print('first')
62        n_start <- 1
63      }
64      if ((lon.rng[2] > lon[length(lon)])) {
65        stop_lon <- lon[length(lon)]
66        n_stop <- length(lon)
67      }
68
69      # Does any user given longitudes exactly equal the discrete ones?
70      if (lon.rng[1] == lon[i]) {start_lon <- lon[i];n_start <- i}
71      if (lon.rng[2] == lon[i]) {stop_lon <- lon[i]; n_stop <- i}
72
73      if ((lon[i] != lon[1]) & (lon[i] != lon[length(lon)])) {
74        # Start lon
75        bigger <- lon.rng[1] > lon[i-1]
```

```
76          smaller <- lon.rng[1] < lon[i]
77          if (bigger == smaller) {
78            #print('yay!')
79            # Which difference is smaller?
80            d1 <- lon.rng[1] - lon[i-1]
81            d2 <- lon[i] - lon.rng[1]
82            if (d1 < d2) {start_lon <- lon[i-1]; n_start <- i-1}
83            if (d1 > d2) {start_lon <- lon[i]; n_start <- i}
84
85          }
86          # stop lon
87          bigger <- lon.rng[2] > lon[i-1]
88          smaller <- lon.rng[2] < lon[i]
89          if (bigger == smaller) {
90            #print('yay')
91            # Which difference is smaller?
92            d1 <- lon.rng[2] - lon[i-1]
93            d2 <- lon[i] - lon.rng[2]
94            if (d1 < d2) {stop_lon <- lon[i-1]; n_stop <- i-1}
95            if (d1 > d2) {stop_lon <- lon[i]; n_stop <- i}
96          }
97        }
98    }
99    #print(lon)
100   # Does the domain include the Greenwhich Meridian?
101   if (n_start > n_stop) {
102     return(c(seq(from=n_start,to=length(lon),by=1),seq(from=1,to=n_stop,by
          =1)))
103   } else {
104     return(seq(from=n_start,to=n_stop,by=1))
105   }
106 }
107
108
109
110 # The function find.lat deals with the following problem: the start
111 # and stop latitude given by the user to define the domain of change
112 # will probably not coincide with a gripoint in the model. The function
113 # located the gridpoint which is closest to the user specified latgitude.
114
115 find.lat <- function(lat,lat.rng) {
116
117   start_lat <- NULL
118   stop_lat <- NULL
119   n_start <- NULL
120   n_stop <- NULL
121
122   for (j in 1:length(lat)) {
123
```

```
124       if ((lat.rng[1] < lat[1])) {
125         start_lat <- lat[1]
126         n_start <- 1
127         #print('first')
128       }
129
130       if (lat.rng[1] == 0) {
131         n_start <- length(lat)/2.+1
132       }
133
134       if (lat.rng[2] == 0) {
135         n_stop <- length(lat)/2.+1
136       }
137
138       if ((lat.rng[2] > lat[length(lat)])) {
139         stop_lat <- lat[length(lat)]#;print(stop_lat)
140         n_stop <- length(lat)
141       }
142
143       if ((lat[j] != lat[1]) & (lat[j] != lat[length(lat)])) {
144         bigger <- lat.rng[1] > lat[j-1]
145         smaller <- lat.rng[1] < lat[j]
146          if (bigger == smaller) {
147           # Which difference is smaller?
148           d1 <- lat.rng[1] - lat[j-1]
149           d2 <- lat[j] - lat.rng[1]
150           if (d1 < d2) {start_lat <- lat[j-1]; n_start <- j-1}
151           if (d1 > d2) {start_lat <- lat[j]; n_start <- j}
152         }
153         bigger <- lat.rng[2] > lat[j-1]
154         smaller <- lat.rng[2] < lat[j]
155         if (bigger == smaller) {
156           # Which difference is smaller?
157           d1 <- lat.rng[2] - lat[j-1]
158           d2 <- lat[j] - lat.rng[2]
159           if (d1 < d2) {stop_lat <- lat[j-1]; n_stop <- j-1}
160           if (d1 > d2) {stop_lat <- lat[j]; n_stop <- j}
161         }
162       }
163     }
164 #print(lat)
165 return(seq(from=n_start,to=n_stop,by=1))
166 }
167
168
169
170
171
172
```

```
173 # The function change_sst takes the following arguments:
174 # bc.file       : file containing boundary conditions for SST (
      climatological)
175 # field.name    : name of the SST field in bc.file
176 # lon.rng       : longitude region for which SST will be changed
177 # lat.rng       : latitude region for which SSt will be changed
178 # dsst          : change in SST (given as a scalar)
179 # dlat & dlon   : defines the relaxation area along the bondaries
180 # relax.bound   : defines which bondaries that will have relaxation
181 # keep.ice      : if changes have been made to the sea ice fraction
182 #               : (must be made separately) set keep.ice to false
183 #               : in order to change temperature where there used to
184 #               : be sea ice...
185
186 change_sst <- function(bc.file=NULL,bc.file2='cami_0000-09-01
      _64x128_L26_c030918.nc',
187 field.name='SST_cpl',field.name2='LANDFRAC',lon.rng=c(0,11),
188 lat.rng=c(-90,-77),dsst=NULL,dlat=2,dlon=2,relax.bound=c(rep(TRUE,4)),keep.
      ice=TRUE) {
189
190
191 library(ncdf)
192 #print(dsst);print(relax.bound)
193
194
195
196 if (file.exists(bc.file)) {
197   print(paste("Reading ",bc.file,"..."))
198
199   # Open netCDF file and read fields
200   nc <- open.ncdf(bc.file,write=TRUE)
201   sst <- get.var.ncdf(nc,field.name)
202   lon <- get.var.ncdf(nc,'lon')
203   lat <- get.var.ncdf(nc,'lat')
204   time <- get.var.ncdf(nc,'time')
205
206   #print(lon)
207   #print(lat)
208
209   # Get land fraction from bc.file2
210   nc2 <- open.ncdf(bc.file2,write=FALSE)
211   landfrac <- get.var.ncdf(nc2,field.name2)
212   print(dim(landfrac))
213   close.ncdf(nc2,verbose=TRUE)
214
215
216
217   # Find the gridpoints closest to the user given domain
218   longitudes <- find.lon(lon,lon.rng)
```

```
219   latitudes <- find.lat(lat,lat.rng)
220
221   # changing the SSTs!!!
222   print('Changing SSTs of region:')
223   print('Located region:')
224   print(paste('  lon=',lon[longitudes[1]],'-',lon[longitudes[length(
          longitudes)]]))
225   print(paste('  lat=',lat[latitudes[1]],'-',lat[latitudes[length(latitudes
          )]]))
226
227
228
229
230
231   old_lon=longitudes
232   old_lat=latitudes
233   relax_longitudes=NULL
234
235   # Relaxation: boundaries are defined in cyclonic order:
236   # relax.bound[1] is the southern zonal boundary
237   # relax.bound[2] is the western meridional boundary
238   # relax.bound[3] is the northern zonal boundary
239   # relax.bound[4] is the eastern meridional boundary
240   if (relax.bound[1] & !relax.bound[3]) {latitudes=latitudes[(dlat+1):
          length(latitudes)]}
241   if (relax.bound[2] & !relax.bound[4]) {longitudes=longitudes[(dlon+1):
          length(longitudes)]}
242   if (relax.bound[3] & !relax.bound[1]) {latitudes=latitudes[1:(length(
          latitudes)-dlat)]}
243   if (relax.bound[4] & !relax.bound[1]) {longitudes=longitudes[1:(length(
          longitudes)-dlon)]}
244
245   if (relax.bound[1] & relax.bound[3]) {latitudes=latitudes[(dlat+1):length
          (latitudes)-dlat]}
246   if (relax.bound[2] & relax.bound[4]) {longitudes=longitudes[(dlon+1):
          length(longitudes)-dlon]}
247
248
249  # If temperature equals -1.8, there is sea ice
250    sst_new <- round(sst,6)
251    ice.ice.baby <- sst_new == -1.8
252
253 sst_old <- sst
254  # Interior solution (without relaxation boundaries)
255
256  for (j in 1:length(lat)) {
257     if (is.element(lat[j],lat[latitudes[1]:latitudes[length(latitudes)]]))
          {
258
```

```
259           # Don't change temperature over land. Weed out elements of
                 longitudes
260           # over land. Find the keepers!
261           keepers <- longitudes[landfrac[longitudes,j]<0.2]
262
263           # Change SST where there is ocean
264           sst[keepers,j,] <- sst[keepers,j,] + dsst
265 #          print(sst[keepers,j,]-sst_old[keepers,j,])
266       }
267     }
268
269
270     a <- dsst / (dlat*(lat[2]-lat[1]))
271     print(a)
272
273     # Relaxed solution
274     for (j in 1:length(lat)) {
275
276       if ((relax.bound[1]) &
277          (is.element(lat[j],lat[(latitudes[1]-dlat-1):(latitudes[1]-1)]))) {
278           # Don't change temperature over land. Weed out elements of
                 longitudes
279           # over land. Find the keepers!
280           keepers <- old_lon[landfrac[old_lon,j]<0.2]
281
282           # Change SST where there is ocean
283           sst[keepers,j,] <- sst[keepers,j,] + dsst -
284                              a*sqrt((lat[latitudes[1]-1]-lat[j])^2)
285       }
286
287          if ((relax.bound[3]) &
288          (is.element(lat[j],lat[(latitudes[length(latitudes)]+1):
289                    (latitudes[length(latitudes)]+dlat+1)]))) {
290
291           # Don't change temperature over land. Weed out elements of
                 longitudes
292           # over land. Find the keepers!
293           keepers <- old_lon[landfrac[old_lon,j]<0.2]
294           print(lat[j])
295           print(dsst -a*sqrt((lat[latitudes[length(latitudes)]+dlat+1]-lat[j
                 ])^2))
296           # Change SST where there is ocean
297           sst[keepers,j,] <- sst[keepers,j,] + dsst -
298                              a*sqrt((lat[latitudes[length(latitudes)]+1]-lat
                                   [j])^2)
299
300       }
301
302     }
```

```
303
304   b <- dsst / (dlon*lon[2]-lon[1])
305
306   latitudes <- find.lat(lat,lat.rng)
307
308   for (i in 1:length(lon)) {
309
310     if ((relax.bound[2]) &
311        (is.element(lon[i],lon[(longitudes[1]-dlon-1):(longitudes[1]-1)])))
              {
312
313          # Don't change temperature over land. Weed out elements of
                longitudes
314          # over land. Find the keepers!
315          keepers <- latitudes[landfrac[i,latitudes]<0.2]
316
317          # Change SST where there is ocean
318          sst[i,keepers,] <- sst[i,keepers,] + dsst -
319                             b*sqrt((lon[longitudes[1]-1]-lon[i])^2)
320     }
321
322        if ((relax.bound[4]) &
323        (is.element(lon[i],lon[(longitudes[length(longitudes)]+1):
324                  (longitudes[length(longitudes)]+dlon+1)]))) {
325
326          # Don't change temperature over land. Weed out elements of
                longitudes
327          # over land. Find the keepers!
328          keepers <- latitudes[landfrac[i,latitudes]<0.2]
329
330          # Change SST where there is ocean
331          sst[i,keepers,] <- sst[i,keepers,] + dsst -
332                             b*sqrt((lon[longitudes[length(longitudes)]+1]-
                                  lon[i])^2)
333
334     }
335
336   }
337
338
339
340
341     # If there is sea ice, change back to -1.8 when keep.ice is true
342    if (keep.ice) {
343      sst[ice.ice.baby] <- -1.8
344      sst[ice.ice.baby] <- round(sst[ice.ice.baby],1)
345    }
346 #print(sst)
347
```

```
348
349
350
351     put.var.ncdf(nc,field.name,sst,verbose=TRUE)
352
353
354     close.ncdf(nc,verbose=TRUE)
355
356     }
357  }
```

Appendix D

The change_ice function

This appendix yields the source code of the R program which has been applied to change the sea ice fraction in the CAM3 modified runs. This program was made using the R environment developed by R Development Core Team (2008) and the R-package NCDF (Pierce, 2006). Both the R environment and the NCDF package are freely available from http://www.R-project.org.

```
1  ######################################################################
2  # This program removes sea ice fraction of the climatological input
3  # file used in the data ocean model (DOM) in CAM3. The data ocean model
4  # reads and interpolates the SST data. The data set monthly samples for
5  # one year.
6  #
7  # The program allows for the user to specify specific regions for
8  # which the sea is is removed for all monthly samples. The
9  # region is a square defined by lon.rng[start_lon,stop_lon] and
10 # lat.rng[start_lat,stop_lat]
11 #
12 ######################################################################
13
14
15 # The function find.lon deals with the following problem: the start
16 # and stop latitude given by the user to define the domain of change
17 # will probably not coincide with a gripoint in the model. The
18 # function located the gridpoint which is closest to the user
19 # specified longitude.
20
21 find.lon <- function(lon,lon.rng) {
22
23   start_lon <- NULL
24   stop_lon <- NULL
25
26   for (i in 1:length(lon)) {
```

```
27      if ((lon.rng[1] == lon[1])) {
28        start_lon <- lon[1]#;print('first')
29      }
30      if ((lon.rng[2] > lon[length(lon)])) {
31        stop_lon <- lon[length(lon)]
32      }
33      if ((lon[i] != lon[1]) & (lon[i] != lon[length(lon)])) {
34        # Start lon
35        bigger <- lon.rng[1] > lon[i-1]
36        smaller <- lon.rng[1] < lon[i]
37        if (bigger == smaller) {
38          # Which difference is smaller?
39          d1 <- lon.rng[1] - lon[i-1]
40          d2 <- lon[i] - lon.rng[1]
41          if (d1 < d2) start_lon <- lon[i-1]
42          if (d1 > d2) start_lon <- lon[i]
43        }
44        # stop lon
45        bigger <- lon.rng[2] > lon[i-1]
46        smaller <- lon.rng[2] < lon[i]
47        if (bigger == smaller) {
48          # Which difference is smaller?
49          d1 <- lon.rng[2] - lon[i-1]
50          d2 <- lon[i] - lon.rng[2]
51          if (d1 < d2) stop_lon <- lon[i-1]
52          if (d1 > d2) stop_lon <- lon[i]
53        }
54      }
55    }
56  return(c(start_lon,stop_lon))
57  }
58
59
60
61  # The function find.lat deals with the following problem: the start
62  # and stop latitude given by the user to define the domain of change
63  # will probably not coincide with a gripoint in the model. The function
64  # located the gridpoint which is closest to the user specified latgitude.
65
66  find.lat <- function(lat,lat.rng) {
67
68    start_lat <- NULL
69    stop_lat <- NULL
70
71    for (j in 1:length(lat)) {
72
73      if ((lat.rng[1] < lat[length(lat)/2+1])) {
74        start_lat <- lat[length(lat)/2+1]
75        #print('first')
```

```
76      }
77      if ((lat.rng[2] > lat[length(lat)])) {
78        stop_lat <- lat[length(lat)]#;print(stop_lat)
79      }
80
81      if ((lat[j] != lat[1]) & (lat[j] != lat[length(lat)])) {
82        bigger <- lat.rng[1] > lat[j-1]
83        smaller <- lat.rng[1] < lat[j]
84        if (bigger == smaller) {
85          # Which difference is smaller?
86          d1 <- lat.rng[1] - lat[j-1]
87          d2 <- lat[j] - lat.rng[1]
88          if (d1 < d2) start_lat <- lat[j-1]
89          if (d1 > d2) start_lat <- lat[j]
90        }
91        bigger <- lat.rng[2] > lat[j-1]
92        smaller <- lat.rng[2] < lat[j]
93        if (bigger == smaller) {
94          # Which difference is smaller?
95          d1 <- lat.rng[2] - lat[j-1]
96          d2 <- lat[j] - lat.rng[2]
97          if (d1 < d2) stop_lat <- lat[j-1]
98          if (d1 > d2) stop_lat <- lat[j]
99        }
100     }
101   }
102 return(c(start_lat,stop_lat))
103 }
104
105
106
107
108 # The function change_sst takes the following arguments:
109 # bc.file       : file containing boundary conditions for SST (
        climatological)
110 # field.name    : name of field in bc.file
111 # lon.rng       : longitude region for which ice cover will be changed
112 # lat.rng       : latitude region for which ice cover will be changed
113
114 change_ice <- function(bc.file=NULL,field.name='ice_cov',lon.rng=c(0,11),
115 lat.rng=c(-90,-77)) {
116
117
118 library(ncdf)
119 quit <- FALSE
120
121
122 if ((file.exists(bc.file)) & (!quit)) {
123   print(paste("Reading ",bc.file,"..."))
```

```
124   #print(paste('Looking for field ',field.name))
125   # Open netCDF file
126   nc <- open.ncdf(bc.file,write=TRUE)
127   print(nc)
128   # Find number of variables in file
129   # NOT coordinate variables
130   nv <- nc$nvars
131   # Create a list for variables
132   cdfvars <- rep("",nv)
133   for (i in 1:nv) cdfvars[i] <- nc$var[[i]]$name
134   #print(cdfvars)
135   # Find the number of the variable which equals field.name
136   pick.var <- grep(field.name,cdfvars)
137
138   # get.var.ncdf reads a the variable field.name
139   # get SST field!!
140   ice_var <- cdfvars[pick.var]
141   print(paste('Field: ',ice_var,' located'))
142   ice <- get.var.ncdf(nc,ice_var)
143   print(dim(ice))
144
145   # Number of dimensions
146   nd <- nc$ndims
147   # Create a list for variables
148   cdfdims <- rep("",nd)
149   for (i in 1:nd) cdfdims[i] <- nc$var[[pick.var]]$dim[[i]]$name
150   print('Field has dimentions:')
151   print(cdfdims)
152
153
154   # Get longitude dimension
155   itim <- grep("lon",cdfdims)
156   lon <- get.var.ncdf(nc,cdfdims[itim])
157   print(lon)
158
159   # Get latitude dimension
160   itim <- grep("lat",cdfdims)
161   lat <- get.var.ncdf(nc,cdfdims[itim])
162   print(lat)
163
164   # Get time dimension
165   itim <- grep("time",cdfdims)
166   #print(itim)
167   time <- get.var.ncdf(nc,cdfdims[itim])
168   #print(time)
169
170
171
172   # Find the gridpoints closest to the user given domain
```

```
173   lon.rng <- find.lon(lon,lon.rng)
174   lat.rng <- find.lat(lat,lat.rng)
175
176   # changing the SSTs!!!
177   print('Remove ice in region')
178   print(paste('  lon=',lon.rng[1],'-',lon.rng[2]))
179   print(paste('  lat=',lat.rng[1],'-',lat.rng[2]))
180
181 ice_old <- ice
182
183
184   for (i in 1:length(lon)) {
185     for (j in 1:length(lat)) {
186       for (t in 1:length(time)) {
187
188         if ((lon[i] >= lon.rng[1]) & (lon[i] <= lon.rng[2]) &
189             (lat[j] >= lat.rng[1]) & (lat[j] <= lat.rng[2])) {
190             #print('ice ice baby...')
191           ice[i,j,t] <- 0
192         }
193
194
195
196       }
197     }
198    }
199
200
201
202
203   put.var.ncdf(nc,ice_var,ice,verbose=TRUE)
204
205
206   close.ncdf(nc,verbose=TRUE)
207
208   }
209 }
```

References

Benestad, Rasmus E. (2008) *cyclones: Cyclone Identification*. URL `http://cran.r-project.org`, R-package version 1.2-2.

Benestad, Rasmus E. and Chen, D. (2006) *The use of a Calculus-based Cyclone Identificatin Method for Generating Storm Statistics*. Tellus, Vol. 58A(4): p. 473–486.

Bengtsson, Lennart; Hodges, Kevin I. and Roeckner, Eerich (2006) *Storm Tracks and Climate Change*. Journal of Climate, Vol. 19: p. 3518–3543.

Black, Robert X. and Dole, Randal M. (2000) *Storm Tracks and Barotropic Deformation in Climate Models*. Journal of Climate, Vol. 13: p. 2712–2728.

Blackmon, Maurice L. (1976) *An Climatological Spectral Study of the 500 mb Geopotential Height of the Northern Hemisphere*. Journal of the Atmospheric Sciences, Vol. 33: p. 1607–1623.

Blackmon, Maurice L.; Wallace, John M.; Lau, Ngar-Cheung and Mullen, Steven L. (1977) *An Observational Study of the Northern Hemisphere Wintertime Circulation*. Journal of the Atmospheric Sciences, Vol. 34: p. 1040–1053.

Branstator, Grant (1992) *The Maintenance of Low-Frequency Atmospheric Anomalies*. Journal of the Atmospheric Sciences, Vol. 49(20): p. 1924–1945.

Branstator, Grant (1995) *Organization of Storm Track Anomalies by Recurring Low-Frequency Circulation Anomalies*. Journal of the Atmospheric Sciences, Vol. 53(2): p. 207–226.

Broccoli, A. J. and Manabe, S. (1992) *The Effects of Orography on Midlatitude Northern Hemisphere Dry Climates*. Jornal of Climate, Vol. 5: p. 1181–1201.

Chang, Edmund K. M. and Orlanski, Isidoro (1993) *On the Dynamics of a Storm Track*. Journal of the Atmospheric Sciences, Vol. 50(7): p. 999–1015.

Chang, Edmund K. M. and Orlanski, Isidoro (2002) *Storm Track Dynamics*. Journal of Climate, Vol. 15: p. 2163–2183.

Collins, William D.; Rasch, Philip J; Boville, Byron A.; Hack, James J.; McCaa, James R.; Williamson, Davis L.; Briegleb, Bruce P.; Bitz, Cecilia M.; Lin, Shian-Jiann and Zhang, Minghua (2006) *The Formulation and Atmospheric Simulation of the Community Atmosphere Model Version 3 (CAM3)*. Journal of Climate, (19): p. 2144–2161.

Farlow, Stanley J. (1993) *Partial differential equations for scientists and engineers* (General Publishing Company Ltd in Canada and Constable and Company Ltd in the United Kingdom).

Gulev, S. K.; Zolina, O. and Grigoriev, S. (2001) *Extratropical Cyclone Variability in the Northern Hemisphere Winter from the NCEP/NCAR Reanalysis data*. Climate Dynamics, (17): p. 795–809.

Held, Isaac M. (1983) *Stationary and Quasi-Stationary Eddies in the Extratropical Troposphere: Theory*. In *Large-scale Dynamical Processes in the Atmosphere*, p. 127–168 (Academic Press).

Held, Isaac M. (1993) *Large-Scale Dynamics and Global Warming*. Bulletin American Meteorological Society, Vol. 74(2): p. 228–241.

Held, Isaac M.; Ting, Mingfang and Wang, Hailan (2002) *Northern Winter Stationary Waves: Theory and Modeling*. Journal of Climate, Vol. 15: p. 2125–2144.

Hinman, Russell (1888) *Eclectic Physical Geography*. The Eclectic Geographies (American Book Company), 1. edition.

Hodges, K. I. (1994) *A General Method for Tracking Analysis and its Application to Meteorological Data*. Monthly Weather Review, Vol. 122(11): p. 2573–2586.

Hodges, K. I. (1999) *Adaptive Constraints for Feature Tracking*. Monthly Weather Review, Vol. 127: p. 1362–1373.

Holton, James R. (2004) *An Introduction to Dynamic Meteorology* (Elsevier Academic Press), 4. edition.

Hoskins, Brian (1983) *Theory of transient eddies*. In Brian Hoskins and Robert Pearce (editors), *Large-Scale Dynamical Processes in the Atmosphere* (Academic Press).

Hoskins, Brian J. and Hodges, Kevin I. (2002) *New Perspectives on the Northern Hemisphere Winter Storm Tracks*. Journal of the Atmospheric Sciences, Vol. 59: p. 1041–1061.

Hoskins, Brian J. and Valdes, Paul J. (1990) *On the Existence of Storm-Tracks*. Journal of the Atmospheric Sciences, Vol. 47(15): p. 1854–1864.

Hurrell, James W.; Hack, James J.; Phillips, Adam S.; Caron, Julie and Yin, Jeffrey (2006) *The Dynamical Simulation of the Community Atmosphere Model Version 3 (CAM3)*. Journal of Climate, (19): p. 2162–2183.

ITT Visual Information Solutions (2007) *IDL Reference Guide*, idl version 6.4 edition.

Kalnay, E.; Kanamitsu, M.; Kistler, R.; Collins, W.; Deaven, D.; Gandin, L.; Iredell, M.; Saha, S.; White, G.; Woollen, J.; Zhu, Y.; Chelliah, M.; Ebisuzaki, W; Higgins, W.; Janowiak, J.; Mo, K. C.; Ropelewshi, C.; Wand, J.; Leetmaa, A; Reynolds, R; Jenne, Ros and Joseph, Dennis (1996) *The NCEP/NCAR 40-Year Reanalysis Project*. Bulletin of the American Meteorological Society, Vol. 77(3): p. 437–471.

Kalnay, Eugenia (2007) *Atmospheric Modeling, Data Assimilation and Predictability* (Cambridge University Press).

LaCasce, Joseph Henry (2008) *GEF4500: Atmosphere-Ocean Dynamics, Lecture Notes*. URL `http://www.uio.no/studier/emner/matnat/geofag/GEF4500/h08/gef4500jhl.pdf`, Department of Geosciences, University of Oslo.

Lau, Ngar-Cheung (1997) *Interactions Between Global SST Anomalies and the Midlatitude Atmospheric Circulation*. Bulletin of the American Meteorological Society, Vol. 78(1): p. 21–33.

Lindzen, R. S. and Farrell, Brian (1980) *A Simple Approximate Result for the Maximum Growth Rate of Baroclinic Instabilities*. Journal of the Atmospheric Sciences, Vol. 37: p. 1648–1656.

MaCaa, James R.; Rothstein, Mathew; Eaton, Brian E.; Rosiniski, James M; Kluzek, Eirik and Vertenstein, Mariana (2004) *User's Guide to the NCAR Community Atmosphere Model (DAM3.0)*. National Center for Atmospheric Research.

Martin, Jonathan E. (2006) *Mid-Latitude Atmospheric dynamics – A First Course* (Wiley).

McCabe, Gregory J.; Clark, Martyn P. and Serreze, Mark C. (2001) *Trends in Northern Hemisphere Surface Cyclone Frequency and Intensity*. Journal of Climate, Vol. 14: p. 2763–2768.

Nakamura, Hisashi (1992) *Midwinter Suppression of Baroclinic Wave Activity in the Pacific*. Journal of the Atmospheric Sciences, Vol. 49(17): p. 1629–1642.

Nakicenovic, Nebojsa; Alcamo, Joseph; Davis, Gerald; de Vries, Bert; Fenhann, Joergen; Gaffin, Stuart; Gregory, Kenneth; Grübler, Arnulf; Jung, Tae Yong; Kram, Tom; Rovere, Emilio Lebre La; Michaelis, Laurie; Mori, Shunsuke; Morita, Tsuneyuki; Pepper, William; Pitcher, Hugh; Price, Lynn; Riahi, Keywan; Roehrl, Alexander; Rogner, Hans-Holger; Sankovski, Alexei; Schlesinger, Michael; Shukla, Priyadarshi; Smith, Steven; Swart, Robert; van Rooijen, Sascha; Victor, Nadejda and Dadi, Zhou (2000) *Special Report on Emissions Scenarios* (Cambridge University Press).

Orlanski, Isidoro (1998) *Poleward Deflection of Storm Tracks*. Journal of the Atmospheric Sciences, Vol. 55(16): p. 2577–2602.

Orsolini, Yvan J. and Sorteberg, Asgeir (2009) *Projected Changes in Eurasian and Arctic Summer Cyclones Under Global Warming in the Bergen Climate Model*. Atmospheric and Oceanic Science Letters, Vol. 2(1): p. 62–67.

Paciorek, Christoper J.; Risbey, James S.; Venture, Valérie and Rosen, Richard D. (2002) *Multiple Indices of Northern Hemisphere Cyclone Activity, Winters 1949-99*. Journal of Climate, Vol. 15: p. 1573–1590.

Pierce, David (2006) *ncdf: Interface to Unidata netCDF data files*. URL `http://cirrus.ucsd.edu/~pierce/ncdf`, R package version 1.6.

R Development Core Team (2008) *R: A Language and Environment for Statistical Computing*. R Foundation for Statistical Computing, Vienna, Austria. URL `http://www.R-project.org`, ISBN,3-90051-07-0.

Trenberth, Kevin E.; D., Philip; Ambenje, Jones Peter; Bojariu, Roxana; Easterling, David; Tank, Albert Klein; Parker, David; Rahimzadeh, Fatemeh; Renwick, James A.; Rusticucci, Matilde; Soden, Brian and Zhai, Panmao (2007) *Climate Change 2007: The Physical Science Basis. Contribution of Working Group I to the Fourth Assessment Report of the Intergovernmental Panel on Climate Change*, chapter Observations: Surface and Atmospheric Climate Change (Cambridge University Press).

Ulbrich, U.; Leckebusch, G. C and Pinto, J. G (2009) *Extra-tropical Cyclones in the Present and Future Climate: a Review*. Theoretical and Applied Climatology, Vol. 96: p. 117–131. URL `www.springerlink.com`, Published with open access.

Vallis, Geoffrey K. (2005) *Atmospheric and Oceanic Fluid Dynamics*. URL `www.princeton.edu/gkv/aofd`.

Wallace, John M. and Hobbs, Peter V. (2006) *Atmospheric Science an Introductory Survey*, Vol. 92 of *International Geophysics Series* (Academic Press), 2. edition.

Wang, Xiaolan L.; Swail, Val R. and Zwires, Forncis W. (2006) *Climatology and Changes of Extratropical Cyclone Activity: Comparison of ERA-40 with NCEP-NCAR Reanalysis for 1958 – 2001*. Journal of Climate, Vol. 19: p. 3145–3166.

Yin, Jeffrey H. (2005) *A Consistent Poleward Shift of the Storm Tracks in Simulations of the 21st Century Climate*. Geophysical Research Letters, Vol. 32.